Designing Transfers Between Earth-Moon Halo Orbits Using Manifolds and Optimization

Gavin M. Brown

Thesis submitted to the Faculty of the
Virginia Polytechnic Institute and State University
in partial fulfillment of the requirements for the degree of

Master of Science
in
Aerospace Engineering

Jonathan T. Black, Chair
Kevin Schroeder
Cornel Sultan

June 19, 2020
Blacksburg, Virginia

Keywords: Transfers, Manifolds, Optimization, Halo Orbits, CR3BP

Designing Transfers Between Earth-Moon Halo Orbits Using Manifolds and Optimization

Gavin M. Brown

(ABSTRACT)

Being able to identify fuel efficient transfers between orbits is critical to planning and executing missions involving spacecraft. With a renewed focus on missions in cislunar space, identifying efficient transfers in the dynamical environment characterized by the Circular Restricted Three-Body Problem (CR3BP) will be especially important, both now and in the immediate future. The focus of this thesis is to develop a methodology that can be used to identify a valid low-cost transfer between a variety of orbits in the CR3BP. The approach consists of two distinct parts. First, tools related to dynamical systems theory and manifolds are used to create an initial set of possible transfers. An optimization scheme is then applied to the initial transfers to obtain an optimized set of transfers. Code was developed in MATLAB to implement and test this approach. The methodology and its implementation were evaluated by using the code to identify a low-cost transfer in three different transfer cases. For each transfer case, the best transfers from each set were compared, and important characteristics of the transfers in the first and final sets were examined. The results from those transfer cases were analyzed to determine the overall efficacy of the approach and effectiveness of the implementation code. In all three cases, in terms of cost and continuity characteristics, the best optimized transfers were noticeably different compared to the best manifold transfers. In terms of the transfer path identified, the best optimized and best manifold transfers were noticeably different for two of the three cases. Suggestions for improvements and other possible applications for the developed methodology were then identified and presented.

Designing Transfers Between Earth-Moon Halo Orbits Using Manifolds and Optimization

Gavin M. Brown

(GENERAL AUDIENCE ABSTRACT)

Being able to identify fuel efficient transfers between orbits is critical to planning and executing missions involving spacecraft. With a renewed focus on lunar missions, identifying efficient transfers between orbits in the space around the Moon will be especially important, both now and in the immediate future. The focus of this thesis is to develop a methodology that can be used to identify a valid low-cost transfer between a variety of orbits in the space around the Moon. The approach was evaluated by using the code to identify a low-cost transfer in three different transfer cases. The results from those transfer cases were analyzed to determine the overall efficacy of the approach and effectiveness of the implementation code. Suggestions for improvements and other possible applications for the developed methodology were then identified and presented.

Dedication

To our capitalist overlords, who instilled in me the irrational tenet that an individual's worth is related only to the fruits of their labor that can be exploited which, accompanied with my own pathological need to find meaning and significance in my life, led me to produce this document instead of taking a nap.

I hope y'all are happy.

And to my dad.

And my dog.

Acknowledgments

First and foremost I would like to thank the members of my advisory committee: Dr. Black, Dr. Schroeder, and Dr. Sultan. I would like to give a special thank you to Dr. Schroeder for helping me learn this material and only firing me when I deserved it.

I would also like to thank Collin Deans for listening to me whine and cry more than anyone should have, Gustavo Gargioni for being my research mentor and role model, and the students and researchers at the Hume Center and Space@VT.

Finally, thank you to my Dad for encouraging me throughout my entire life and for saying some of my results look like a mad space alien.

Contents

List of Figures

List of Tables

List of Abbreviations

$\boldsymbol{\Phi}(t, t_0)$ State Transition Matrix for the state at time t with respect to the state at time t_0.

$\boldsymbol{A}(t)$ Jacobian Matrix

$\boldsymbol{M}$ The Monodromy Matrix. The State Transition Matrix after one period.

$\delta\vec{X}(t)$ Offset in the state at time t.

ΔV Delta-V

$\dot{x}$ The time-derivative of x.

λ_i Eigenvalue of a matrix with corresponding eigenvector $\vec{v}_i$.

μ Nondimensional mass parameter

ω^{SI} Angular rotation rate of frame S with respect to inertial frame I.

ϕ_t Flow of the nonlinear system

$\vec{r}_{i,j}$ The displacement vector of m_i relative to m_j. Note: Two subscripts.

$\vec{r}_i$ The displacement vector of m_i relative to the system's center of mass. Note: One subscript.

$\vec{v}_i$ Eigenvector of a matrix with corresponding eigenvalue λ_i.

$\vec{X}(t)$ The state vector at some time t.

$\vec{X}_i^j$ The state on trajectory j at time t_i.

C Jacobi Constant

E The Energy Integral

L_i	The L_i Lagrange point.
m_1	Mass of Primary Body 1 ($m_1 > m_2$). For Earth-Moon system: the Earth.
m_2	Mass of Primary Body 2 ($m_2 < m_1$). For Earth-Moon system: the Moon.
m_s	Mass of Secondary Body. For this document: the satellite.
n	Mean Motion
$r_{i,j}$	The distance of m_i relative to m_j. Note: Two subscripts.
r_i	The distance of m_i relative to the system's center of mass. Note: One subscript.
T	Period of an Orbit
t	Some time t.
U	Pseudo-Potential
V	Magnitude of the Velocity
x_{Li}	x-coordinate of the L_i Lagrange point.
2D	Two-Dimensional
3D	Three-Dimensional
COM	Center of Mass
CR3BP	Circular Restricted Three-Body Problem
DU	Distance Units. Canonical Units for distance.
HOT	Higher Order Terms
MTN	Node Corresponding to the Manifold Transition Point
MTP	Manifold Transition Point

NLP Nonlinear Programming

OCP Optimal Control Problem

ODE Ordinary Differential Equation

PCR3BP Planar Circular Restricted Three-Body Problem

RC Restricted Coordinate

STM State Transition Matrix

TU Time Units. Canonical Units for time.

Chapter 1

Introduction

1.1 Overview

The Circular Restricted Three-Body Problem (CR3BP) is one of the most well-known examples of a system demonstrating chaotic dynamics. The CR3BP can be used to model many systems of practical interest such as the motion of a spacecraft in the vicinity of the Earth and Moon, or a spacecraft in the vicinity of the Sun and Earth. Identifying low-cost transfer paths between areas and orbits of interest in these systems is important, especially since NASA has recently produced plans to place a Lunar Gateway in orbit around the Moon [4]. In this thesis, techniques related to dynamical systems theory, such as those related manifolds and Poincaré maps, will be used in an attempt to identify low-cost transfers between orbits in the CR3BP.

1.2 Background & Motivation

The first appearance of the three-body problem, or describing the motion of three bodies when only gravitational forces are acting on those bodies, can be attributed to Isaac Newton [5]. While many famous mathematicians have produced significant work on this problem, no analytical solution completely describing motion in the system exists [6]. Several simplifying assumptions that led to the first description of the restricted three-body problem were made by Leonard Euler in 1772 [7]. Euler was also the first to describe the motion in a rotating

frame and identify three collinear points of equilibrium [3, 7]. Two more equilibrium points were identified later in 1772 by Joseph-Louis Lagrange, and all five points of equilibrium are referred to as "Lagrange points" or "libration points", even though Euler identified the first three points five years earlier in 1767 [8]. In 1836 the mathematician Carl Gustav Jacob Jacobi identified the only known constant of motion in the restricted problem that was first described by Euler. This constant of motion is an energy-like term and is referred to as the "Jacobi constant" or the "Jacobi integral" [8, 9]. Significant work building on the implications of the Jacobi constant was performed by George Hill in 1878 [7]. Other significant contributions related to dynamical systems theory have been made by a number of individuals including Henri Poincaré who published three volumes of work on the subject in 1892, 1893, and 1899, and George D. Birkhoff who produced additional work on the qualitative dynamics of this problem in 1915 [7].

One family of orbits about libration points that will be used in this analysis are "halo" orbits. These orbits were first given their name in 1968 by Farquhar [8, 10]. Farquhar produced additional work on halo orbits over the next three years, with other notable contributions being made by Breakwell and Brown in 1979 and Howell in 1984 [8, 11, 12, 13]. Some of the first analytical expressions used for approximating halo orbits about the collinear Lagrange points were derived by Richardson in 1980 [14]. In 1984, Breakwell and Howell produced fundamental work on a similar group of orbits which are now known as Near Rectilinear Halo Orbits (NRHOs) [13, 15].

Some of the first work on transfers between parking orbits about a primary body and orbits about libration points in the CR3BP was performed by L. A. D'Amario in 1973 [8, 16, 17]. In 2001, Gómez et al. [18] used "invariant manifold tubes" from orbits about libration points to design transfers between separate three body systems. A significant amount of recent research into orbits and transfers in the vicinity of the Earth and Moon has been conducted by the Multi-Body Dynamics Research Group at Purdue University under Dr. Kathleen Howell. One tool that can be used when designing transfers in the CR3BP is Adaptive

Trajectory Design, a GUI package developed in 2013 by Haapala et al. [19], building on work by Schlei [20, 21]. Howell also presented research pertaining to the development of a "transportation network in cislunar space" in 2015 [22].

Several historical spacecraft missions have used orbits around libration points, such as "NASA's Genesis Discovery Mission... the Solar and Heliospheric Observatory (SOHO), WIND, Advanced Composition Explorer (ACE), WMAP, and ISEE-3/ICE" [8]. Some possible future missions include a Lunar Gateway space station and multi-moon orbiters [8]. The Genesis Discovery Mission and ISEE-3/ICE are two important examples of past missions involving orbits around libration points. Launched in 1978, the ISEE-3/ICE mission was the first to use an orbit around an libration point [23]. ISEE-3/ICE performed a fly by of the Giacobini-Zinner comet, and was the first spacecraft to conduct detailed observations of both the tail of Earth's magnetosphere and the solar wind heading towards the Earth [17, 24]. Launched in 2001, the Genesis Discovery Mission was the first spacecraft mission to leverage techniques related to invariant manifolds with differential corrections and dynamical systems theory when designing the spacecraft's trajectory [8]. The spacecraft went to a halo orbit about the Sun-Earth L_1 Lagrange point and returned to Earth over a course of three years [8, 25]. When designing the trajectory for the Genesis Discovery Mission, the gravitational effects of the Earth, Moon, and Sun were considered [17].

Extending beyond the CR3BP to include the effects of an additional body is possible, such as including the gravitational effects of the Sun in the Earth-Moon system. Including the effects of the Sun by approximating the motion of the Earth-Moon system's barycenter around the Sun-Earth-Moon system's barycenter as a circular orbit creates a new form of the dynamics model referred to as the Bicircular Restricted Four-Body Problem [8]. For example, Pritchett et al. [26] focused on designing optimal transfers in this model. While these more advanced models can be used, the effects of the Sun and other bodies outside the CR3BP system of interest will be ignored in this analysis. A simplified form of the CR3BP in which the motion of the smallest body is restricted to be in the plane of motion of the two larger bodies is

referred to as the Planar Circular Restricted Three-Body Problem (PCR3BP).

Designing the best transfer between orbits can be viewed as one form of an optimal control problem (OCP). Many applications associated with astrodynamics and trajectory design can be viewed as OCPs. Some of these applications include designing landings on the Moon from parking orbits and designing aeroassisted orbital transfers with plane changes [27, 28]. While manifolds are often used when designing transfers in the CR3BP, in some specific applications other approaches have been used, like using Family G periodic orbits for transfers to the L_4 and L_5 points [29].

With multiple space agencies showing a renewed interest in spacecraft missions that are in cislunar space, being able to design efficient transfers between different orbits in the CR3BP is important [30, 31]. The techniques that have been developed over the last 250 years since Euler first made the assumptions associated with the CR3BP dynamics model will be used to accomplish this objective. A transfer design tool that can accept the initial conditions of an initial orbit and a desired orbit, in addition to a reasonable number of other input parameters, and return a sufficiently low-cost transfer (in terms of ΔV or propellant required) from the initial orbit to the desired orbit will be created. Several complexities that arise in process of designing a code base that is general enough to design a transfer between a wide variety of possible orbits will be identified and discussed. Possible improvements that could be made to the transfers will also be assessed.

1.3 Organization of Thesis

The remainder of this document will be divided into four chapters.

Chapter 2: Theoretical Background. An overview of the relevant theory associated with designing transfers between orbits in the CR3BP will be provided in this chapter. A description of the specific dynamics model will be given including details on the equations

of motion and Lagrange points. Dynamical systems theory will also be discussed. This discussion will cover linearizing the nonlinear equations of motion, stability analysis of the linearized system, invariant manifolds, and Poincaré sections & maps. Finally, a background on approaches used to solve OCPs and differential corrections will be provided.

Chapter 3: Methodology & Approach. Details related to the specific methodology used in this analysis will be provided in this chapter. How the theory discussed in Chapter 2 will be leveraged to construct manifold transfers between general periodic orbits in the CR3BP will be addressed. Correction and optimization schemes will then be used on the manifold transfers to create a new set of possible transfers. A justification for the use of these schemes, possible approaches to correct and optimize the original manifold transfers, and the details associated with these particular schemes will all be provided in this chapter.

Chapter 4: Results for Selected Cases. The methodology discussed in Chapter 3 will be applied to three transfer cases. In order to verify the efficacy of this methodology, a transfer in a PCR3BP test case, referred to as "Transfer 1" or "2D Case 1", between two Lyapunov orbits will be designed. How well the methodology performed in this test case will be discussed before moving on to the next transfer case. A transfer for a 3D case, referred to as "Transfer 2" or "3D Case 1", between two halo orbits will be designed. Finally, a transfer for another 3D case, referred to as "Transfer 3" or "3D Case 2", between a halo orbit and one planned orbit for the Lunar Gateway will be designed.

Chapter 5: Conclusion. A summary of the results obtained for the three selected transfer cases in Chapter 4 will be provided. Important conclusions that can be identified from the results of applying this specific methodology will be discussed as well, including conclusions related to the overall efficacy of this methodology. Possible issues with this methodology will then be identified. Improvements that could be made to address those possible issues, as well as future work that could be performed to build on the work outlined in this document, will be discussed.

Chapter 2

Theoretical Background

2.1 Dynamics Model

2.1.1 Circular Restricted 3 Body Problem

The CR3BP is an idealized model of the general three-body problem with four key assumptions:

1. The three bodies can be modeled as point masses.
2. The only forces acting on the bodies are the gravitational forces between them.
3. Related to the second assumption, the mass of the third body m_s (known as the secondary body) is significantly less than the masses of the two bodies m_1 and m_2 (known as the primary bodies), such that m_s does not affect the motion of m_1 and m_2.
4. The two primary bodies move around their center of mass in circular orbits such that their angular rotation rate about that point ω^{SI} is constant.

Instead of using an inertial frame I, the motion of the third body can be represented in a rotating frame S such that the two primaries have fixed positions with respect to this new rotating frame. As the mass of the secondary body is considered negligible compared to the masses of the two primaries, the center of mass of the system (known as the "barycenter") is in the same position as the center of mass of the two primaries. In this rotating frame the barycenter is located at the origin. As the rotation rate of this new frame is the same as the

rotation rate of the two primaries, the positions of m_1 and m_2 with respect to the system's barycenter are fixed. The directions of the axes in this rotating frame are as follows:

- The positive x-axis $\hat{i}$ is in the primaries' plane of motion and points along the line from the larger primary m_1 to the smaller primary m_2.
- The positive z-axis $\hat{k}$ points out of the primaries' plane of motion in the same direction as the angular velocity vector of the primaries.
- The positive y-axis $\hat{j}$ completes the right-handed coordinate system and is in the primaries' plane of motion.

A representation of this model is provided in Figure 2.1. Please note that the naming conventions used in this figure are also used in the rest of this document. Unless otherwise indicated, all displacements and distances are measured in the rotating frame. A distance $r_{i,j}$ represents the distance between m_i and m_j. A distance with only one subscript r_i represents the distance of m_i relative to the system's barycenter.

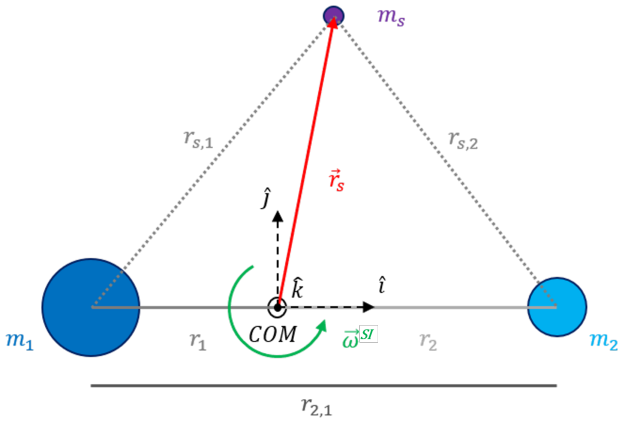

Figure 2.1: Model of the Rotating Frame for the CR3BP. Please note this figure is not to scale. The two primary bodies are m_1 (dark blue) and m_2 (light blue), and the secondary body is m_s (purple). The barycenter of the system (black circle) is in the same position as the center of mass of the two primaries. The $\hat{k}$ axis points out of the page and $\vec{\omega}^{si}$, which is the angular rotation rate vector of the rotating frame S with respect to the inertial frame I, is in the $+\hat{k}$ direction.

Canonical Units

A transformation to a set of units, referred to as Canonical Units, can be performed such that the distance between the two primaries is $r_{2,1} = 1$ DU (distance unit), and the period of the two primaries' motion about their center of mass is $T = 2\pi$ TU (time units). The mean motion is $n = 1$ rad/TU because $T = 2\pi$ TU. Achieving this desired transformation is accomplished by first setting the sum of the two primaries' masses equal to one by utilizing a non-dimensional parameter μ such that $m_1 = 1 - \mu$ and $m_2 = \mu$. The system's barycenter is at the origin and $r_{2,1}$ is always equal to 1 DU, so $r_1 = -\mu$ DU and $r_2 = 1 - \mu$ DU. This thesis focuses on the Earth-Moon system so the following values will be used: 1 DU = 384,400 km and $\mu = 0.012150584673414$ [32, 33, 34]. The three conversions used to convert to Canonical Units are:

$$1\text{ DU} = r_{2,1} \qquad 1\text{ TU} = \sqrt{\frac{r_{2,1}^3}{G(m_1 + m_2)}} \qquad \mu = \frac{m_2}{m_1 + m_2} \tag{2.1}$$

Euqations of Motion

The phase space in the CR3BP is six dimensional and, for a body in this system, the state vector at any time t is $\vec{X}(t) = [x(t)\ y(t)\ z(t)\ \dot{x}(t)\ \dot{y}(t)\ \dot{z}(t)]^T$. The elements in the state vector are given in the rotating frame with respect to the system's barycenter. The first three elements represent the position of m_s in DU and the last three elements represent the velocity of m_s in DU/TU. The equations of motion for m_s in the rotating frame are ordinary differential equations (ODEs) of the form $\dot{\vec{X}} = f(\vec{X})$, and are expressed in Canonical Units in Equation 2.2. Functions like MATLAB's *ode113*, a "variable-step, variable-order Adams-Bashforth-Moulton PECE solver," can be used to integrate these ODEs [35, 36]. A detailed discussion of how to derive the equations of motion using Newtonian, Lagrangian, and Hamiltonian approaches can be found in Section 2.3 of Koon et al. [8]. Note that all derivatives are with respect to time in TU, e.g. $\dot{x}$ is in DU/TU and $\ddot{x}$ is in DU/TU^2.

$$\dot{\vec{X}} = f(\vec{X}) = \begin{bmatrix} \dot{x} \\ \dot{y} \\ \dot{z} \\ \ddot{x} \\ \ddot{y} \\ \ddot{z} \end{bmatrix} = \begin{bmatrix} \dot{x} \\ \dot{y} \\ \dot{z} \\ 2\dot{y} + x - \frac{(1-\mu)(x-r_1)}{r_{s,1}^3} - \frac{\mu(x-r_2)}{r_{s,2}^3} \\ -2\dot{x} + y - \frac{(1-\mu)y}{r_{s,1}^3} - \frac{\mu y}{r_{s,2}^3} \\ -\frac{(1-\mu)z}{r_{s,1}^3} - \frac{\mu z}{r_{s,2}^3} \end{bmatrix} \qquad r_{s,i} = \sqrt{(x-r_i)^2 + y^2 + z^2} \quad (2.2)$$

While these equations of motion do depend on terms that are time-varying, like the positions and velocities (e.g. x, y, z, $\dot{x}$, $\dot{y}$, and $\dot{z}$), there is no explicit dependence on the variable for time t. Therefore, the equations of motion in the CR3BP can be classified as time-independent. As described in Koon et al. [8], the equations of motion for the CR3BP can be represented in a Hamiltonian form and they do not explicitly depend on time. So, representative of the fact that the energy of a body in the CR3BP will be conserved, there is a scalar constant of motion. This conserved quantity is the Jacobi constant C, also known as the Jacobi integral, and it can be calculated using the following equation,

$$C = 2U - V \qquad \text{where} \qquad U = \frac{1-\mu}{r_{s,1}} + \frac{\mu}{r_{s,2}} + \frac{1}{2}(x^2 + y^2) \quad \text{and} \quad V = \dot{x}^2 + \dot{y}^2 + \dot{z}^2 \quad (2.3)$$

where U is the pseudo-potential and V is the magnitude of the velocity in the rotating frame [37]. Please note that all the terms in Equation 2.3 are to be taken with respect to the rotating frame. Looking at the terms in Equation 2.3, it is apparent that the Jacobi constant is a slightly modified form of the energy integral $E = T + V$ expressed in the rotating frame [8, 9].

2.1.2 Lagrange Points

While it may not be obvious looking at the equations of motion in Equation 2.2, there is a set of initial conditions that if a body were to start in a certain position at rest, that body would remain fixed in that position for all time with respect to the rotating frame. In other words, $\vec{X}(t) = \vec{X}(t_0)$ for initial conditions $\vec{X}(t_0) = [x_0\ y_0\ z_0\ 0\ 0\ 0]$ at time t_0 that result in no velocity or acceleration, i.e. $\ddot{x}(t) = \ddot{y}(t) = \ddot{z}(t) = \dot{x}(t) = \dot{y}(t) = \dot{z}(t) = 0$ for any and all time t. As the locations of the two primaries with respect to the system's barycenter are fixed, a body at any of these points would not appear to move from the perspectives of the system's barycenter, mass m_1, or mass m_2. These points are called Lagrange points and there are five of them in the CR3BP. A diagram of the general locations of the Lagrange points in the CR3BP is provided in Figure 2.2.

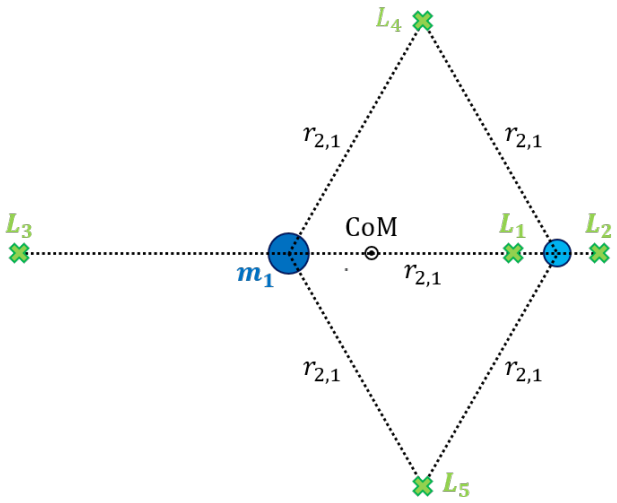

Figure 2.2: Lagrange Points in the CR3BP. Please note this figure is not to scale. The two primaries are m_1 (dark blue) and m_2 (light blue). The locations of the five Lagrange points (L_1, L_2, L_3, L_4, and L_5) are indicated by light green "x"s. L_4 and L_5 are vertices on equilateral triangles with sides of length $r_{2,1}$ with m_1 and m_2 at the other vertices.

The locations of these points can be obtained by solving for x, y, and z, such that the last three terms in Equation 2.2 are zero (remember for these points $\dot{x} = \dot{y} = \dot{z} = 0$). The Lagrange points will all have $z = 0$, as that is the only way to ensure the last term in Equation 2.2 is always zero. The five Lagrange points in the CR3BP can be divided into

two distinct types.

The first three Lagrange points (L_1, L_2, L_3) are unstable and collinear. These three points lie on the x-axis ($y = 0$) which ensures that the second to last term in the equations of motion is zero because $\dot{x} = 0$. The x-values of these three points can be obtained by substituting in $y = z = \dot{y} = 0$ into the fourth term in the equations of motion, then setting that term equal to zero, and solving for x. A numerical solver can be used to solve the resulting equations for the values of x at L_1, L_2, and L_3, respectively:

$$x_{L1} + \frac{1-\mu}{(x_{L1}-r_1)^2} + \frac{\mu}{(x_{L1}-r_2)^2} = 0 \tag{2.4}$$

$$x_{L2} - \frac{1-\mu}{(x_{L2}-r_1)^2} + \frac{\mu}{(x_{L2}-r_2)^2} = 0 \tag{2.5}$$

$$x_{L3} - \frac{1-\mu}{(x_{L3}-r_1)^2} - \frac{\mu}{(x_{L3}-r_2)^2} = 0 \tag{2.6}$$

The other two Lagrange points (L_4, L_5) are neutrally stable provided $m_1 \geq 24.96\ m_2$, and their locations can be calculated by using geometry [9, 38]. Both of these Lagrange points are located at a vertex of their own invariant equilateral triangle. The two primary bodies are located at the other two vertices in both of these triangles. So L_4 is in the x-y plane and is a distance of $r_{2,1}$ away from m_1 60° above the x-axis. Similarly, L_5 is in the x-y plane and is a distance of $r_{2,1}$ away from m_1, but is 60° below the x-axis. By using trigonometry,

$$x_{L4} = \frac{1}{2} + r_1 = \frac{1}{2} - \mu \qquad y_{L4} = \frac{\sqrt{3}}{2} \tag{2.7}$$

$$x_{L5} = \frac{1}{2} + r_1 = \frac{1}{2} - \mu \qquad y_{L5} = -\frac{\sqrt{3}}{2} \tag{2.8}$$

The locations of the Lagrange points in several common CR3BP systems can be found in Section 2.5 of Schlei [21]. The locations of the points were calculated in the Earth-Moon system, and the results are provided in Table 2.1.

Lagrange Point	Location (DU)		
	x	y	z
L_1	0.8369	0	0
L_2	1.1557	0	0
L_3	-1.0051	0	0
L_4	0.4878	0.8660	0
L_5	0.4878	-0.8660	0

Table 2.1: Locations of Lagrange Points in the Earth-Moon System. All units are in DU.

Orbits of Interest

Many periodic orbit families in the CR3BP are based around the five Lagrange points. Some of these families include 2D Lyapunov orbits, as well as 3D halo orbits, axial orbits, and vertical orbits. Methods to obtain initial conditions for these orbits are discussed in more detail in Section 2.3.2. A comprehensive discussion of orbit families in the CR3BP, as well as tabulated results of initial conditions for a variety of these orbits, can be found in Grebow [1]. Differential correction coupled with numerical continuation can be used to identify the initial conditions for orbits in these families [8]. Several diagrams of some of these orbit families which are directly from Grebow [1] are in Figure 2.3.

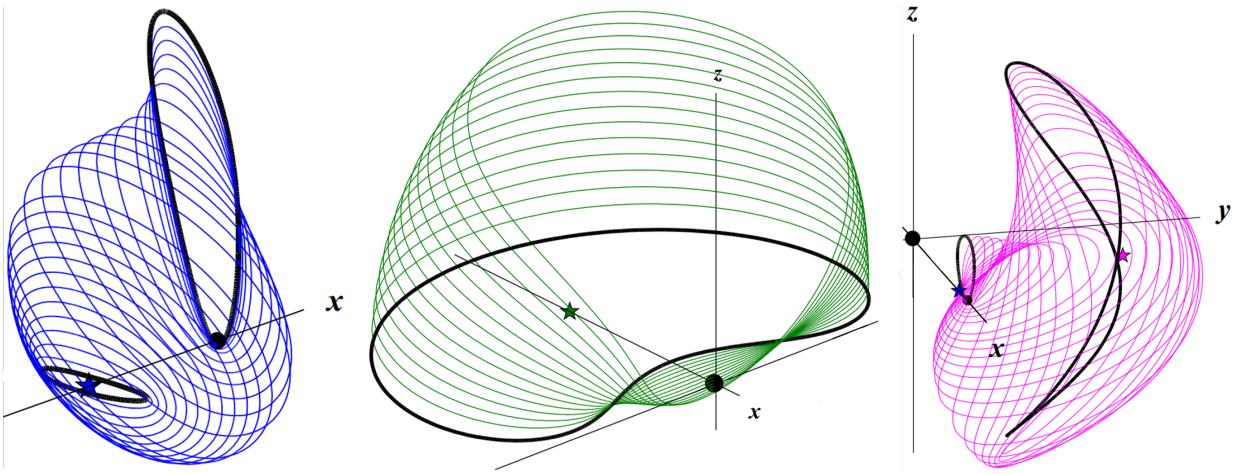

Figure 2.3: Orbit Families in the CR3BP directly from Grebow [1]. Note that these figures are directly from Grebow [1] and are the diagrams in (from left to right) Table 3.4, Table 3.6, and Table 3.15 in that document. Left: L_1 Northern halo orbit family. Middle: L_3 Northern halo orbit family. Right: L_4 Northern axial orbit family.

Much work has recently been done in identifying and determining initial conditions for periodic orbits in the CR3BP. Analytical expressions describing some orbits in the CR3BP have been derived, and analytical expressions for halo orbits can be found in Richardson [14]. Some methods used to identify orbits in the CR3BP that are asymmetrical also exist [39, 40]. Some orbits cover large amounts of space, moving in regions that are not only in the immediate space around one Lagrange point. One example of these orbits are "horseshoe orbits" that around L_4 and L_5 [1, 41].

As stated in Chapter 1, NASA has announced plans for a crewed station in cislunar space known as the "Lunar Gateway" [4]. The Lunar Gateway will be in a Near Rectilinear Halo Orbit (NRHO) about L_2. Detailed information about the planned orbit for the Lunar Gateway can be found in Williams et al. [2]. An image and state vector for one specific possible orbit directly from Williams et al. [2] has been included below,

Epoch	Nov 8, 2025 23:22:07.10353 TDB
r_x (km)	-1.259522004870315e+2
r_y (km)	1.209609406690672e+2
r_z (km)	4.357680596646485e+3
v_x (km/s)	-4.229621580376978e-2
v_y (km/s)	1.468560523456590e+0
v_z (km/s)	-3.538768970252955e-3

Figure 2.4: Orbit and State Vector for the Lunar Gateway directly from Williams et al. [2]. Left: Image of 20 revolutions of one possible orbit for the planned Lunar Gateway that is stable for 110 days in the ephemeris model. L_2 southern NRHO family with a periapsis of 4500 km. Right: Table of the state vector that produces the orbit on the left. Please note that the values in this table are in the rotating frame, but are with respect to the Moon, not the system's barycenter (so not with respect to the origin of the rotating frame).

2.1.3 State Transition Matrix & Monodromy Matrix

The state on a trajectory at some time depends on the trajectory's state at some initial time t_0 and the time since t_0. So, the expression for a state on a trajectory at time t after t_0 is:

$$\vec{X}_1 = \vec{X}(\vec{X}_0, t) \tag{2.9}$$

Let there be two different trajectories that start at time t_0, and at time t_0 Trajectory A has the state $\vec{X}_0^a$ and Trajectory B has the state $\vec{X}_0^b$. The states along these trajectories at some time t after t_0 are given by:

$$\vec{X}_1^a = \vec{X}(\vec{X}_0^a, t) \quad \text{and} \quad \vec{X}_1^b = \vec{X}(\vec{X}_0^b, t) \tag{2.10}$$

If a spacecraft is initially on Trajectory A, but at t_0 the state of the spacecraft is instantaneously changed from $\vec{X}_0^a$ which is on Trajectory A to $\vec{X}_0^b$ which is on Trajectory B, the offset in the state at t_0 is $\delta\vec{X}(t_0)$. For time t after t_0, the difference between the states on the two trajectories at time t can be represented as $\delta\vec{X}(t)$. The offset in the state is represented by:

$$\delta\vec{X}(t_0) = \vec{X}_0^b - \vec{X}_0^a \tag{2.11}$$

$$\vec{X}_1^b = \vec{X}_1^a + \delta\vec{X}(t) \tag{2.12}$$

The offset in the state is also represented in Figure 2.5, which is modified from Gordon [42].

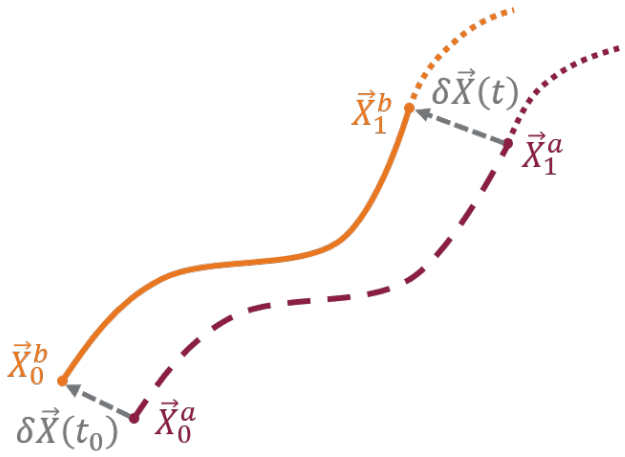

Figure 2.5: Offset in the State Vector. The solid line indicates the trajectory that is followed. The long dashed line represents the trajectory that would have been followed. The small dashed lines represent the future path of the trajectories. The points indicate the states on the trajectories at initial time t_0 and some other time t. Maroon indicates the initial trajectory, orange indicates the final trajectory, and gray indicates the offset between the trajectories. This figure is not geometrically accurate, and is modified from Gordon [42].

It would be useful to know how the offset from the initial trajectory $\delta\vec{X}(t)$ changes in time, based on the initial offset $\delta\vec{X}(t_0)$. With that idea in mind, the procedure outlined in Section 3.1.1 of Pritchett [3] will be followed. The procedure begins by recognizing the second expression in Equation 2.10 is equal to Equation 2.12.

$$\vec{X}(\vec{X}_0^b, t) = \vec{X}_1^a + \delta\vec{X}(t)$$

$$\vec{X}(\vec{X}_0^a + \delta\vec{X}(t_0), t) = \vec{X}_1^a + \delta\vec{X}(t) \tag{2.13}$$

By using a Taylor Series expansion on Equation 2.13, a linear approximation of $\delta\vec{X}(t)$ as a function of $\delta\vec{X}(t_0)$ can be obtained,

$$\vec{X}(\vec{X}_0^a, t) + \left.\frac{\partial\vec{X}_1}{\partial\vec{X}_0}\right|_{\vec{X}^a} \delta\vec{X}(t_0) + \text{HOT} = \vec{X}_1^a + \delta\vec{X}(t)$$

$$\vec{X}_1^a + \left.\frac{\partial\vec{X}_1}{\partial\vec{X}_0}\right|_{\vec{X}^a} \delta\vec{X}(t_0) + \text{HOT} = \vec{X}_1^a + \delta\vec{X}(t) \tag{2.14}$$

By canceling out terms that appear on both sides of the equation, ignoring the higher order terms (HOT), and rearranging, the following linear approximation is obtained:

$$\delta\vec{X}(t) = \mathbf{\Phi}(t, t_0)\,\delta\vec{X}(t_0) \quad \text{where} \quad \mathbf{\Phi}(t, t_0) = \left.\frac{\partial\vec{X}_1}{\partial\vec{X}_0}\right|_{\vec{X}^a} \tag{2.15}$$

The term $\mathbf{\Phi}(t, t_0)$ in Equation 2.15 is known as the state transition matrix (STM). The significance of the previous equation is that the STM can be used to relate how an initial offset in the state at some time t_0 affects the offset in the state at some other time t. Note that the STM is evaluated along the initial trajectory. The STM in the CR3BP is a 6 x 6 matrix with the elements given in Equation 2.16.

$$\mathbf{\Phi}(t,t_0) = \begin{bmatrix} \frac{\partial x(t)}{\partial x(t_0)} & \frac{\partial x(t)}{\partial y(t_0)} & \frac{\partial x(t)}{\partial z(t_0)} & \frac{\partial x(t)}{\partial \dot{x}(t_0)} & \frac{\partial x(t)}{\partial \dot{y}(t_0)} & \frac{\partial x(t)}{\partial \dot{z}(t_0)} \\ \frac{\partial y(t)}{\partial x(t_0)} & \frac{\partial y(t)}{\partial y(t_0)} & \frac{\partial y(t)}{\partial z(t_0)} & \frac{\partial y(t)}{\partial \dot{x}(t_0)} & \frac{\partial y(t)}{\partial \dot{y}(t_0)} & \frac{\partial y(t)}{\partial \dot{z}(t_0)} \\ \frac{\partial z(t)}{\partial x(t_0)} & \frac{\partial z(t)}{\partial y(t_0)} & \frac{\partial z(t)}{\partial z(t_0)} & \frac{\partial z(t)}{\partial \dot{x}(t_0)} & \frac{\partial z(t)}{\partial \dot{y}(t_0)} & \frac{\partial z(t)}{\partial \dot{z}(t_0)} \\ \frac{\partial \dot{x}(t)}{\partial x(t_0)} & \frac{\partial \dot{x}(t)}{\partial y(t_0)} & \frac{\partial \dot{x}(t)}{\partial z(t_0)} & \frac{\partial \dot{x}(t)}{\partial \dot{x}(t_0)} & \frac{\partial \dot{x}(t)}{\partial \dot{y}(t_0)} & \frac{\partial \dot{x}(t)}{\partial \dot{z}(t_0)} \\ \frac{\partial \dot{y}(t)}{\partial x(t_0)} & \frac{\partial \dot{y}(t)}{\partial y(t_0)} & \frac{\partial \dot{y}(t)}{\partial z(t_0)} & \frac{\partial \dot{y}(t)}{\partial \dot{x}(t_0)} & \frac{\partial \dot{y}(t)}{\partial \dot{y}(t_0)} & \frac{\partial \dot{y}(t)}{\partial \dot{z}(t_0)} \\ \frac{\partial \dot{z}(t)}{\partial x(t_0)} & \frac{\partial \dot{z}(t)}{\partial y(t_0)} & \frac{\partial \dot{z}(t)}{\partial z(t_0)} & \frac{\partial \dot{z}(t)}{\partial \dot{x}(t_0)} & \frac{\partial \dot{z}(t)}{\partial \dot{y}(t_0)} & \frac{\partial \dot{z}(t)}{\partial \dot{z}(t_0)} \end{bmatrix} \tag{2.16}$$

The initial goal was to obtain an expression for $\delta\vec{X}(t)$ as a function of $\delta\vec{X}(t_0)$. As shown in Equation 2.15, they are related by the STM. So to achieve that initial goal, the STM must be known at every time t. The STM is clearly time-varying as the the elements of the state along the trajectory change with time. An expression for the time rate of change of the STM can be obtained by performing the following manipulation:

$$\dot{\mathbf{\Phi}}(t,t_0) = \frac{d}{dt}\frac{\partial \vec{X}_1}{\partial \vec{X}_0} = \frac{\partial}{\partial \vec{X}_0}\frac{d\,\vec{X}_1}{dt} = \frac{\partial}{\partial \vec{X}_0}\,\vec{f}(\vec{X}_1) = \frac{\partial \vec{f}(\vec{X}_1)}{\partial \vec{X}_1}\frac{\partial \vec{X}_1}{\partial \vec{X}_0} \tag{2.17}$$

The last term in Equation 2.17 is just the STM, so Equation 2.17 can be put in the form,

$$\dot{\mathbf{\Phi}}(t,t_0) = \boldsymbol{A}(t)\,\mathbf{\Phi}(t,t_0) \quad \text{where} \quad \boldsymbol{A}(t) = \frac{\partial \vec{f}(\vec{X}_1)}{\partial \vec{X}_1} \tag{2.18}$$

The term $\boldsymbol{A}(t)$, which is known as the Jacobian matrix, has the elements given in Equation 2.19.

$$\boldsymbol{A}(t) = \begin{bmatrix} \frac{\partial \dot{x}(t)}{\partial x} & \frac{\partial \dot{x}(t)}{\partial y} & \frac{\partial \dot{x}(t)}{\partial z} & \frac{\partial \dot{x}(t)}{\partial \dot{x}} & \frac{\partial \dot{x}(t)}{\partial \dot{y}} & \frac{\partial \dot{x}(t)}{\partial \dot{z}} \\ \frac{\partial \dot{y}(t)}{\partial x} & \frac{\partial \dot{y}(t)}{\partial y} & \frac{\partial \dot{y}(t)}{\partial z} & \frac{\partial \dot{y}(t)}{\partial \dot{x}} & \frac{\partial \dot{y}(t)}{\partial \dot{y}} & \frac{\partial \dot{y}(t)}{\partial \dot{z}} \\ \frac{\partial \dot{z}(t)}{\partial x} & \frac{\partial \dot{z}(t)}{\partial y} & \frac{\partial \dot{z}(t)}{\partial z} & \frac{\partial \dot{z}(t)}{\partial \dot{x}} & \frac{\partial \dot{z}(t)}{\partial \dot{y}} & \frac{\partial \dot{z}(t)}{\partial \dot{z}} \\ \frac{\partial \ddot{x}(t)}{\partial x} & \frac{\partial \ddot{x}(t)}{\partial y} & \frac{\partial \ddot{x}(t)}{\partial z} & \frac{\partial \ddot{x}(t)}{\partial \dot{x}} & \frac{\partial \ddot{x}(t)}{\partial \dot{y}} & \frac{\partial \ddot{x}(t)}{\partial \dot{z}} \\ \frac{\partial \ddot{y}(t)}{\partial x} & \frac{\partial \ddot{y}(t)}{\partial y} & \frac{\partial \ddot{y}(t)}{\partial z} & \frac{\partial \ddot{y}(t)}{\partial \dot{x}} & \frac{\partial \ddot{y}(t)}{\partial \dot{y}} & \frac{\partial \ddot{y}(t)}{\partial \dot{z}} \\ \frac{\partial \ddot{z}(t)}{\partial x} & \frac{\partial \ddot{z}(t)}{\partial y} & \frac{\partial \ddot{z}(t)}{\partial z} & \frac{\partial \ddot{z}(t)}{\partial \dot{x}} & \frac{\partial \ddot{z}(t)}{\partial \dot{y}} & \frac{\partial \ddot{z}(t)}{\partial \dot{z}} \end{bmatrix} \tag{2.19}$$

Expressions for $\dot{x}(t)$, $\dot{y}(t)$, $\dot{z}(t)$, $\ddot{x}(t)$, $\ddot{y}(t)$, and $\ddot{z}(t)$ are obtained from the equations of motion in Equation 2.2. Once the partial derivatives are taken, the elements of $\boldsymbol{A}(t)$ are evaluated using the state vector along the trajectory at time t, i.e. $\vec{X}_1^a$. Note that while the elements of $\boldsymbol{A}(t)$ are time-varying, they depend only on the elements of $\vec{X}_1^a$; they do not explicitly depend on the time variable t. Using the equations of motion for the CR3BP with Equation 2.19, the elements of Jacobian matrix in the CR3BP are:

$$\boldsymbol{A}(t) = \begin{bmatrix} 0 & 0 & 0 & 1 & 0 & 0 \\ 0 & 0 & 0 & 0 & 1 & 0 \\ 0 & 0 & 0 & 0 & 0 & 1 \\ \frac{\partial^2 U}{\partial x^2} & \frac{\partial^2 U}{\partial x \partial y} & \frac{\partial^2 U}{\partial x \partial z} & 0 & 2 & 0 \\ \frac{\partial^2 U}{\partial y \partial x} & \frac{\partial^2 U}{\partial y^2} & \frac{\partial^2 U}{\partial y \partial z} & -2 & 0 & 0 \\ \frac{\partial^2 U}{\partial z \partial x} & \frac{\partial^2 U}{\partial z \partial y} & \frac{\partial^2 U}{\partial z^2} & 0 & 0 & 0 \end{bmatrix} \tag{2.20}$$

Note that the expression for U can be found in Equation 2.3. Expressions for the partial derivatives of U that are in Equation 2.18 are provided in the equations below.

$$\frac{\partial^2 U}{\partial x^2} = 1 - \frac{1-\mu}{r_{s,1}^3} - \frac{\mu}{r_{s,2}^3} + \frac{3(1-\mu)(x-r_1)^2}{r_{s,1}^5} - \frac{3\mu(x-r_2)^2}{r_{s,2}^5} \tag{2.21}$$

$$\frac{\partial^2 U}{\partial x \partial y} = \frac{\partial^2 U}{\partial y \partial x} = \frac{3(1-\mu)(x-r_1)y}{r_{s,1}^5} - \frac{3\mu(x-r_2)y}{r_{s,2}^5} \tag{2.22}$$

$$\frac{\partial^2 U}{\partial x \partial z} = \frac{\partial^2 U}{\partial z \partial x} = \frac{3(1-\mu)(x-r_1)z}{r_{s,1}^5} - \frac{3\mu(x-r_2)z}{r_{s,2}^5} \tag{2.23}$$

$$\frac{\partial^2 U}{\partial y^2} = 1 - \frac{1-\mu}{r_{s,1}^3} - \frac{\mu}{r_{s,2}^3} + \frac{3(1-\mu)y^2}{r_{s,1}^5} - \frac{3\mu y^2}{r_{s,2}^5} \tag{2.24}$$

$$\frac{\partial^2 U}{\partial y \partial z} = \frac{\partial^2 U}{\partial z \partial y} = \frac{3(1-\mu)yz}{r_{s,1}^5} - \frac{3\mu yz}{r_{s,2}^5} \tag{2.25}$$

$$\frac{\partial^2 U}{\partial z^2} = -\frac{1-\mu}{r_{s,1}^3} - \frac{\mu}{r_{s,2}^3} + \frac{3(1-\mu)z^2}{r_{s,1}^5} - \frac{3\mu z^2}{r_{s,2}^5} \tag{2.26}$$

Equation 2.18 is in the form of a matrix differential equation. Because the STM is 6 x 6, Equation 2.18 results in 36 scalar differential equations for each of the 36 scalar elements of the STM. Just like the six equations of motion, those 36 differential equations can be solved by using an ODE integrator like MATLAB's *ode113*. To integrate those 36 differential equations for each element of the STM, 36 initial conditions are needed. The initial conditions for the STM at time t_0 can be obtained by evaluating Equation 2.15 at time $t = t_0$,

$$\delta\vec{X}(t_0) = \boldsymbol{\Phi}(t_0, t_0)\, \delta\vec{X}(t_0)$$

$$\boldsymbol{\Phi}(t_0, t_0) = \boldsymbol{I}_{6\text{x}6} \tag{2.27}$$

So, 42 differential equations need to be integrated from time t_0 to time t in order to obtain the STM at time t. In summary, if $\delta\vec{X}(t_0)$ is known, an approximation for $\delta\vec{X}(t)$ can be obtained by using the STM (Equation 2.15). In addition, by using Equation 2.18 and Equation 2.27, the STM at any time t can also be obtained.

As stated previously in this section, $\boldsymbol{A}(t)$ is not explicitly dependent on time. This statement is confirmed by the fact that the variable t does not explicitly appear anywhere in Equation 2.20. So, the values of the elements in $\boldsymbol{A}(t)$ are only dependent on the state vector at the time that $\boldsymbol{A}(t)$ is being evaluated at. If the state vector at one time is the same as the state vector at another time, then the Jacobian matrix is the same for both of those states. For a periodic orbit, the state vector along the orbit is the same at different times, i.e. the state on the orbit at time t_0 is the same as the state on the orbit at time t if $t = t_0 + kT$ where k is an integer and T is the orbit period [43]. Therefore, if the initial trajectory is a periodic orbit, then the Jacobian matrix is periodic [8, 17]. The fact that the Jacobian matrix is periodic when the initial trajectory is a periodic orbit is an important characteristic that will be relevant in Section 2.2.1. Still assuming that the initial trajectory is a periodic orbit, the offset in the state after one period of that initial orbit is of particular interest.

The monodromy matrix $\boldsymbol{M}$ is a special term for the STM at $t = T$ where T is the period of the orbit, i.e. $\boldsymbol{M} = \boldsymbol{\Phi}(T, t_0)$. The monodromy matrix contains important information about the stability of the orbit [44]. What that information is and how to obtain that information are both discussed in the next section.

2.2 Dynamics Systems Theory

2.2.1 Stability Analysis

As stated in the previous section, the monodromy matrix can be useful when assessing the stability of a periodic orbit. The eigenvalues of the monodromy matrix, also known as Floquet exponents, and their corresponding eigenvectors, will be represented by λ_i and $\vec{v}_i$, respectively. λ_i and $\vec{v}_i$ can be used to identify directions $\delta\vec{X}(t)$, from a given point in the state space $\vec{X}(t)$, that shifting the state of the given point in those directions will result in distinct types of motion [44]. As the monodromy matrix is 6 x 6 for the CR3BP, there are six eigenvalue/eigenvector pairs.

Floquet Theory

Also, as stated in the previous section, the Jacobian matrix is periodic when the trajectory that the Jacobian matrix is being evaluated at is a periodic orbit. The fact that the Jacobian is periodic can be used to prove that Floquet Theory can be applied to this problem using the process outlined in Section 4.3 of Koon et al. [8]. The Floquet Theorem is:

$$\boldsymbol{\Phi}(t, t_0) = \boldsymbol{P}(t)e^{\boldsymbol{R}t} \tag{2.28}$$

"where $\boldsymbol{P}(t)$ is a T-periodic matrix and $\boldsymbol{R}$ is a constant matrix" [8]. Both $\boldsymbol{P}(t)$ and $\boldsymbol{R}$ are

6 x 6 matrices. Evaluating Equation 2.28 at $t = t_0$,

$$\boldsymbol{\Phi}(t_0, t_0) = \boldsymbol{P}(t_0)e^{\boldsymbol{R}t_0}$$

From Equation 2.27 $\boldsymbol{\Phi}(t_0, t_0)$ is the 6 x 6 identity matrix,

$$\boldsymbol{I}_{6\text{x}6} = \boldsymbol{P}(t_0)e^{\boldsymbol{R}t_0}$$

Let $\mathbf{0}_{6\text{x}6}$ represent the 6 x 6 zeroes matrix. By letting $t_0 = 0$,

$$\boldsymbol{I}_{6\text{x}6} = \boldsymbol{P}(0)e^{\mathbf{0}_{6\text{x}6}}$$

By using the fact that a matrix exponential of an n x n zeroes matrix is the n x n identity matrix, the expression for $\boldsymbol{P}(0)$ is

$$\boldsymbol{P}(0) = \boldsymbol{I}_{6\text{x}6}$$

Because $\boldsymbol{P}(t)$ is a T-periodic matrix,

$$\boldsymbol{P}(0 + kT) = \boldsymbol{I}_{6\text{x}6}$$

where k is an integer. Evaluating Equation 2.28 at $t = T$, the following expression for the monodromy matrix can be obtained,

$$\boldsymbol{\Phi}(T, 0) = \boldsymbol{P}(T)e^{\boldsymbol{R}T}$$

$$\boldsymbol{M} = \boldsymbol{I}_{6\text{x}6}e^{\boldsymbol{R}T}$$

$$\boldsymbol{M} = e^{\boldsymbol{R}T} \tag{2.29}$$

Evaluating Equation 2.28 at integer multiples of the period T,

$$\begin{aligned}
\boldsymbol{\Phi}(0 + kT, 0) &= \boldsymbol{P}(0 + kT)e^{\boldsymbol{R}(0+kT)} \\
\boldsymbol{\Phi}(kT, 0) &= \boldsymbol{I}_{6\text{x}6}e^{\boldsymbol{R}kT} \\
\boldsymbol{\Phi}(kT, 0) &= (e^{\boldsymbol{R}T})^k \\
\boldsymbol{\Phi}(kT, 0) &= \boldsymbol{M}^k
\end{aligned} \tag{2.30}$$

As stated in Section 4.3 of Koon et al. [8], by ignoring higher order terms, and as a result of Equation 2.30,

$$\delta\vec{X}(t_0 + kT) = \boldsymbol{M}^k\delta\vec{X}(t_0) \tag{2.31}$$

Stability & Eigenspaces

The monodromy matrix is a real symplectic matrix. By Lyapnuov's Theorem, because $\boldsymbol{M}$ is a symplectic matrix, for every eigenvalue λ_i of $\boldsymbol{M}$, there must be another eigenvalue λ_j of $\boldsymbol{M}$ that is a reciprocal of λ_i, i.e. $\lambda_j = \lambda_i^{-1}$ [3, 17]. Because $\boldsymbol{M}$ is a real matrix, if one eigenvalue λ_i of $\boldsymbol{M}$ is complex, then another eigenvalue λ_j of $\boldsymbol{M}$ must be the complex conjugate of λ_i, i.e. $\lambda_j = \bar{\lambda}_i$. Also, the complex eigenvalues of $\boldsymbol{M}$ have a magnitude of one to ensure that they are also reciprocal [3].

Another important property of the monodromy matrix is that its eigenvectors are linearly independent [43, 45]. So, the eigenvectors of $\boldsymbol{M}$ span the six-dimensional space $\mathbb{R}^6$. If the reader chooses to review Section 3.1 in Wiggins [43], it would be useful to note that the constant matrix $\boldsymbol{R}$ in Equation 2.29 is the Jacobian matrix evaluated on the initial orbit at

time T, and that the eigenvectors of some constant matrix $\boldsymbol{B}$ are the same as the eigenvectors of the matrix $e^{\boldsymbol{B}T}$ (note in this case $\boldsymbol{B} = \boldsymbol{A}$). Recalling the convention used at the end of Section 2.1.3, the initial offset in a state $\delta\vec{X}(t_0)$ is a vector in the six-dimensional state space. So, $\delta\vec{X}(t_0)$ can be represented as a linear combination of the eigenvectors of the monodromy matrix:

$$\delta\vec{X}(t_0) = \sum_{i=1}^{6} c_i\vec{v}_i \tag{2.32}$$

where the term c_i is a scalar for $i = 1, 2, ..., 6$. Substituting the expression in Equation 2.32 into Equation 2.31

$$\delta\vec{X}(t_0 + kT) = \boldsymbol{M}^k \left(\sum_{i=1}^{6} c_i\vec{v}_i \right)$$

$$\delta\vec{X}(t_0 + kT) = \sum_{i=1}^{6} c_i\boldsymbol{M}^k\vec{v}_i \tag{2.33}$$

A new expression for $\boldsymbol{M}^k\vec{v}_i$ can be obtained by recognizing that $\vec{v}_i$ (for $i = 1, 2, ..., 6$) are the eigenvectors of the matrix $\boldsymbol{M}^k$. From the fundamentals of linear algebra,

$$\boldsymbol{M}\vec{v}_i = \lambda_i\vec{v}_i \tag{2.34}$$

$$\boldsymbol{M}\boldsymbol{M}\vec{v}_i = \boldsymbol{M}\lambda_i\vec{v}_i$$

$$\boldsymbol{M}^2\vec{v}_i = \lambda_i\boldsymbol{M}\vec{v}_i$$

$$\boldsymbol{M}^2\vec{v}_i = \lambda_i^2\vec{v}_i \tag{2.35}$$

By continuing to left multiply by both sides of the equation by $\boldsymbol{M}$, the expression on the top of the next page can be obtained,

$$\boldsymbol{M}^k \vec{v}_i = \lambda_i^k \vec{v}_i \tag{2.36}$$

Substituting this expression into Equation 2.33,

$$\delta\vec{X}(t_0 + kT) = \sum_{i=1}^{6} c_i \lambda_i^k \vec{v}_i \tag{2.37}$$

If $\delta\vec{X}(t_0)$ is only in the direction of just one of the eigenvectors, (i.e. Equation 2.32 can be simplified to $\delta\vec{X}(t_0) = c_\alpha \vec{v}_\alpha$, where α is just a number from one to six), then Equation 2.37 can be simplified to:

$$\delta\vec{X}(t_0 + kT) = c_\alpha \lambda_\alpha^k \vec{v}_\alpha \tag{2.38}$$

$$\delta\vec{X}(t_0 + kT) = \lambda_\alpha^k \delta\vec{X}(t_0) \tag{2.39}$$

Remember that Equation 2.39 represents the linearized approximation of the offset in the state from the initial periodic orbit at a time that is k periods after time t_0. The behavior of $\delta\vec{X}(t_0 + kT)$ is completely dependent on the value of $|\lambda_\alpha|$. Perturbing a state that is initially on a periodic orbit in the direction of $\vec{v}_\alpha$ (in the state space) corresponding to:

- $|\lambda_\alpha| < 1$ results in motion that is asymptotically stable.
- $|\lambda_\alpha| = 1$ results in motion that is neutrally stable.
- $|\lambda_\alpha| > 1$ results in motion that is unstable.

These relationships can be justified by looking at Equation 2.39. If $|\lambda_\alpha| < 1$, after one period $|\delta\vec{X}(t_0 + T)| < |\delta\vec{X}(t_0)|$. As k approaches infinity (i.e. the time after t_0 approaches infinity), the magnitude in the offset from the original state on the initial orbit will approach zero. In other words, the new trajectory resulting from the initial offset in the state will

asymptotically approach the original trajectory as $t \to \infty$. So, at time $t = t_0 + kT$, the state on the new trajectory will get closer to the state on the original trajectory as k increases. If $|\lambda_\alpha| > 1$, after one period $|\delta\vec{X}(t_0 + T)| > |\delta\vec{X}(t_0)|$. So, at time $t = t_0 + kT$, the state on the new trajectory will get further away from the state on the original trajectory as k increases. The new trajectory resulting from the initial offset in the state will asymptotically approach the original trajectory as $t \to -\infty$. If $|\lambda_\alpha| = 1$, then the magnitude in the offset between the state on the new trajectory relative to the state on the old trajectory will neither exponentially grow nor decay. There are actually two possible cases where $|\lambda_\alpha| = 1$. If λ_α has an imaginary component then, at time $t = t_0 + kT$, the perturbated state will oscillate around the state on the original trajectory as k increases [46]. If $|\lambda_\alpha|$ is purely real then $\lambda_\alpha = \pm 1$. If $\lambda_\alpha = 1$ then, at time $t = t_0 + kT$, the offset $\delta\vec{X}(t)$ will be the exact same as the offset at time t_0, $\delta\vec{X}(t_0)$. But, if $\lambda_\alpha = -1$, then at time $t = t_0 + kT$, the perturbation $\delta\vec{X}(t)$ will be the same as $-\delta\vec{X}(t_0)$ for odd k and $\delta\vec{X}(t_0)$ for even k.

By grouping the eigenvalues of $\boldsymbol{M}$ together based on what type of motion an initial offset in the direction of each eigenvector will cause, the state space can be viewed as consisting of three structures that result in the three distinct types of motion listed on the previous page. Let the number of eigenvalues that have a magnitude equal to one be n_C. If the number of eigenvalues that have a magnitude less than one is n_S, then the number of eigenvalues that have a magnitude greater than one is $n_U = n_S$ because Lyapunov's Theorem states that the eigenvalues must occur in reciprocal pairs. Since there are six eigenvectors $n_S + n_U + n_C = 6$. $n_U + n_S = 2n_S$ must always be even because n_S must always be an integer. Since $2n_S + n_C = 6$, and six is an even number, then n_C must be even. Let the span of the eigenvectors corresponding to eigenvalues with magnitudes less than one, equal to one, and greater than one be represented by E^S (the stable subspace), E^C (the center subspace), and E^U (the unstable subspace), respectively. It is important to note that a state that is in one of these three subspaces at some initial time will stay in that subspace for all time [43].

For this discussion, the initial state at time t_0 was on a periodic orbit $\vec{X}_0^a$. If the offset in this

initial state vector is in the same direction as the equations of motion when evaluated at the initial point (i.e. $\delta\vec{X}(t_0)$ is in the same direction as $f(\vec{X}_0^a)$), then the new state would still be a state on the original periodic orbit. In other words, the offset in the state vector from the initial time is the same offset in the state vector that would occur if that initial state was propagated along its orbit. As the new state is on the same periodic orbit, after one orbit period, the offset between the states will be the exact same as it was at the initial time. This means that one of eigenvalues of $\boldsymbol{M}$ has to be equal to exactly one. Because of Lyapunov's Theorem, if one eigenvalue of $\boldsymbol{M}$ has a value exactly equal to one, then another eigenvalue of $\boldsymbol{M}$ has to be equal to one. The first eigenvalue of one indicated that the initial orbit was periodic. The second eigenvalue of one indicates that the initial orbit is one member of a family of orbits [37]. So, two eigenvalues of $\boldsymbol{M}$ are equal to exactly one.

For all points on a periodic orbit, the eigenvalues of $\boldsymbol{M}$ are the same regardless of what point on that orbit is used to calculate $\boldsymbol{M}$. If there is even one eigenvalue of $\boldsymbol{M}$ that has a magnitude greater than one ($n_U > 1$), the periodic orbit is unstable. For most of the orbits of interest mentioned in Section 2.1.2, $n_S = n_U = 1$ and $n_C = 4$ [1, 42]. Detailed figures depicting the eigenvalue structure for a number of CR3BP orbit families can be found in Howell [22]. When $n_S = n_U = 1$, E^S is in the direction of the 6D space indicated by the one eigenvector $\vec{v}_S = \vec{v}_i$ that corresponds to $|\lambda_i| < 1$. Also in this case, E^U is in the direction of the 6D space indicated by the one eigenvector $\vec{v}_U = \vec{v}_i$ that corresponds to $|\lambda_i| > 1$.

It is important to remember that the dynamics of the CR3BP are nonlinear. The relationships between the three types of motion and $\delta\vec{X}(t_0)$ that have been discussed in this section were based on the eigenvalues and eigenvectors of the monodromy matrix. Recall that the monodromy matrix came from a linearized approximation of the dynamics. With that idea in mind, two questions arise: 1. are there dynamical structures in the nonlinear dynamics that will yield motion of the three distinct types and, 2. if they do exist, is there a relationship between those nonlinear structures and the stable, center, and unstable subspaces identified in the stability analysis of the linearized dynamics?

2.2.2 Invariant Manifolds

The answers to both of the previous questions are yes. Regarding the first question, the structures in the nonlinear dynamics that are in essence equivalent to the three subspaces are referred to as invariant manifolds. Just like there were stable, center, and unstable subspaces in the analysis of the linearized dynamics (E^S, E^C, and E^U), there are stable, center, and unstable manifolds in the nonlinear dynamics (W^S, W^C, and W^U). There are several possible methods that can be used to calculate these manifolds [21, 47]. Each periodic orbit has its own set of manifolds, so often times manifolds will be represented by $W(\Gamma)$ to indicate that the manifold W is a manifold for the orbit Γ. The stable and unstable manifolds are of particular interest to transfers between orbits. Perturbing a state vector that is on a periodic orbit in the direction of a(n):

- Stable manifold results in motion that will return to the original periodic orbit.
- Unstable manifold results in motion that will depart from the original periodic orbit.

Local & Global Manifolds

The manifolds of a periodic orbit in their entirety are referred to as "global manifolds". The local stable, center, and unstable manifolds are the parts of the global stable, center, and unstable manifolds that are close to the periodic orbit. The local stable, center, and unstable manifolds are represented as W^S_{loc}, W^C_{loc}, and W^U_{loc}, respectively. As a definition, propagating some state $\vec{X}_i$ in time using the nonlinear equations of motion to some state after propagation $\vec{X}_f$ can be represented as

$$\vec{X}_f = \phi_t(\vec{X}_i) \tag{2.40}$$

where ϕ_t is referred to as the "flow of the nonlinear system" [48]. The stable manifold

theorem for periodic orbits, from Section 3.5 of Perko [48], gives definitions for the local stable and local unstable manifolds.

$$W^S_{loc}(\Gamma) = \{\vec{X}_i \in N \mid d(\phi_t(\vec{X}_i), \Gamma) \to 0 \text{ as } t \to \infty \text{ and } \phi_t(\vec{X}_i) \in N \text{ for } t \geq 0\} \tag{2.41}$$

$$W^U_{loc}(\Gamma) = \{\vec{X}_i \in N \mid d(\phi_t(\vec{X}_i), \Gamma) \to 0 \text{ as } t \to -\infty \text{ and } \phi_t(\vec{X}_i) \in N \text{ for } t \leq 0\} \tag{2.42}$$

where Γ is a periodic orbit, N is the region around Γ, $d(\_,\_)$ represents the difference between the two items in the parentheses, and ϕ_t is the nonlinear flow of the system [48]. The local stable manifold of a periodic orbit consists of all the states $\vec{X}_i$ that 1) are in the region around the periodic orbit, and 2) when $\vec{X}_i$ is propagated forward in time by t to the state $\vec{X}_f$: 2. a) $\vec{X}_f$ approaches a state on the initial orbit as $t \to \infty$, and 2. b) $\vec{X}_f$ remains in the region around the orbit. The local unstable manifold of a periodic orbit consists of all the states $\vec{X}_i$ that 1) are in the region around the periodic orbit, and 2) when $\vec{X}_i$ is propagated backward in time by $-t$ to the state $\vec{X}_f$: 2. a) $\vec{X}_f$ approaches a state on the initial orbit as $|t| \to \infty$, and 2. b) $\vec{X}_f$ remains in the region around the orbit [48].

When a state on a local manifold is propagated in time, a trajectory that represents the global manifold is obtained [42, 48]. A trajectory on the global stable manifold is obtained by propagating a state on the local stable manifold backward in time. A trajectory on the global unstable manifold is obtained by propagating a state on the local unstable manifold forward in time. This relationship is represented mathematically as shown in Perko [48]:

$$W^S(\Gamma) = \bigcup_{t \leq 0} \phi_t(W^S_{loc}(\Gamma)) \tag{2.43}$$

$$W^U(\Gamma) = \bigcup_{t \geq 0} \phi_t(W^U_{loc}(\Gamma)) \tag{2.44}$$

Stepping Onto Manifolds

The relationship between the manifolds and the subspaces is given by the stable and center manifold theorems for periodic orbits [3, 48]. Close to the orbit, W^S_{loc}, W^C_{loc}, and W^U_{loc} are tangent to E^S_{loc}, E^C_{loc}, and E^U_{loc}, respectively. Let the magnitude of the change in the position components of $\vec{X}^a_0$ in the phase space be represented by the scalar value d. By the stable and center manifold theorems for periodic orbits, for a value of d that is "small enough", the direction of the stable manifold is in the same direction as the eigenvector of the monodromy matrix $\vec{v}_i$ corresponding to $|\lambda_i| < 1$. Similarly, for a value of d that is "small enough", the direction of the unstable manifold is in the same direction as the eigenvector of the monodromy matrix $\vec{v}_i$ corresponding to $|\lambda_i| > 1$. Remember that for most orbits (and all the orbits used in this analysis), there is only one eigenvector with a corresponding $|\lambda_i| < 1$ ($\vec{v}_S$), and only one eigenvector with a corresponding $|\lambda_i| > 1$ ($\vec{v}_U$). The change in $\vec{X}^a_0$ to a new state that approximates a state on the manifolds ($\vec{X}^a_{S,0}$ or $\vec{X}^a_{U,0}$ for new states on the stable or unstable manifolds, respectively) is given by the following two equations, where $\vec{v}_i = [x_{v_i}\ y_{v_i}\ z_{v_i}\ \dot{x}_{v_i}\ \dot{y}_{v_i}\ \dot{z}_{v_i}]$.

$$\vec{X}^a_{S,0} = \vec{X}^a_0 \pm \frac{d}{\sqrt{x^2_{v_S} + y^2_{v_S} + z^2_{v_S}}}\,\vec{v}_S \tag{2.45}$$

$$\vec{X}^a_{U,0} = \vec{X}^a_0 \pm \frac{d}{\sqrt{x^2_{v_U} + y^2_{v_U} + z^2_{v_U}}}\,\vec{v}_U \tag{2.46}$$

Moving the state in the direction of the local manifold in this way is also referred to as "stepping" onto the manifold. A visual representation of this relationship, directly from Pritchett [3], is provided in Figure 2.6. Note that the "±" symbol appears in the previous equations because eigenvectors are "bidirectional", and an initial condition in both the positive and negative direction of the eigenvector is needed to generate an entire manifold [3, 21, 49]. The value of d should be small enough to yield a valid approximation of the manifold's direction, but not too small as the manifolds asymptotically approach or

depart (depending on the manifold type) the orbit. For analysis in the Earth-Moon system, d values typically range from 0.4 to 100 km [3, 8]. For this analysis, a value of $d = 25$ km was selected. Note, if the state and eigenvector are in Canonical Units, d should be in DU.

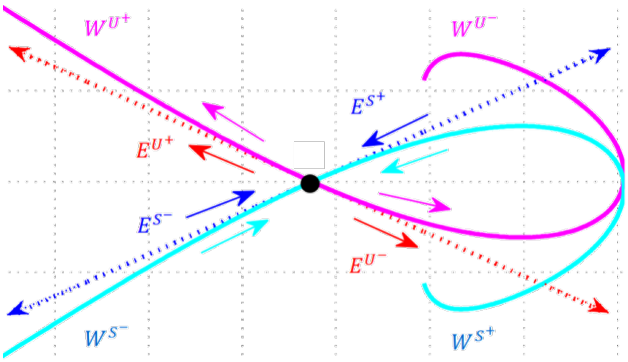

Figure 2.6: Stepping onto Manifolds directly from Pritchett [3]. W^S is the stable manifold and W^U is the unstable manifold. The superscripts $^+$ and $^-$ indicate positive and negative steps onto the manifolds, respectively. Linear approximations of the manifolds' directions are given by E^S and E^U, which are in the directions of $\vec{v}_S$ and $\vec{v}_U$, respectively. The black dot in the middle is the original state $\vec{X}_0^a$ for which the manifolds are determined.

The states $\vec{X}_{S,0}^a$ and $\vec{X}_{U,0}^a$ in Equation 2.45 and Equation 2.46 are states on the local stable and unstable manifolds of the orbit. Remembering Equation 2.43 and Equation 2.44, propagating these states in time will produce trajectories on the global manifolds. For an L_1 halo orbit, a visual representation of the procedure outlined in this section is shown in Figure 2.7.

Manifolds for an Entire Orbit

Remember, the two $\vec{X}_{S,0}^a$ states ($\vec{X}_{S^+,0}^a$ and $\vec{X}_{S^-,0}^a$) and the two $\vec{X}_{U,0}^a$ states ($\vec{X}_{U^+,0}^a$ and $\vec{X}_{U^-,0}^a$) were obtained by using the previous process for one point on the periodic orbit: $\vec{X}_0^a$ (the state on the orbit at t_0). So, this procedure will yield the manifolds for only one point on the periodic orbit. However, Equation 2.41 and Equation 2.42 referred to not just states that go to specifically one point on the orbit, the states could go to any point on the orbit. So, all the other points on the orbit need to be considered. A representation for the manifolds of the entire orbit, not just the manifolds of one point on the orbit, can be obtained by repeating the above process for many other points on the orbit.

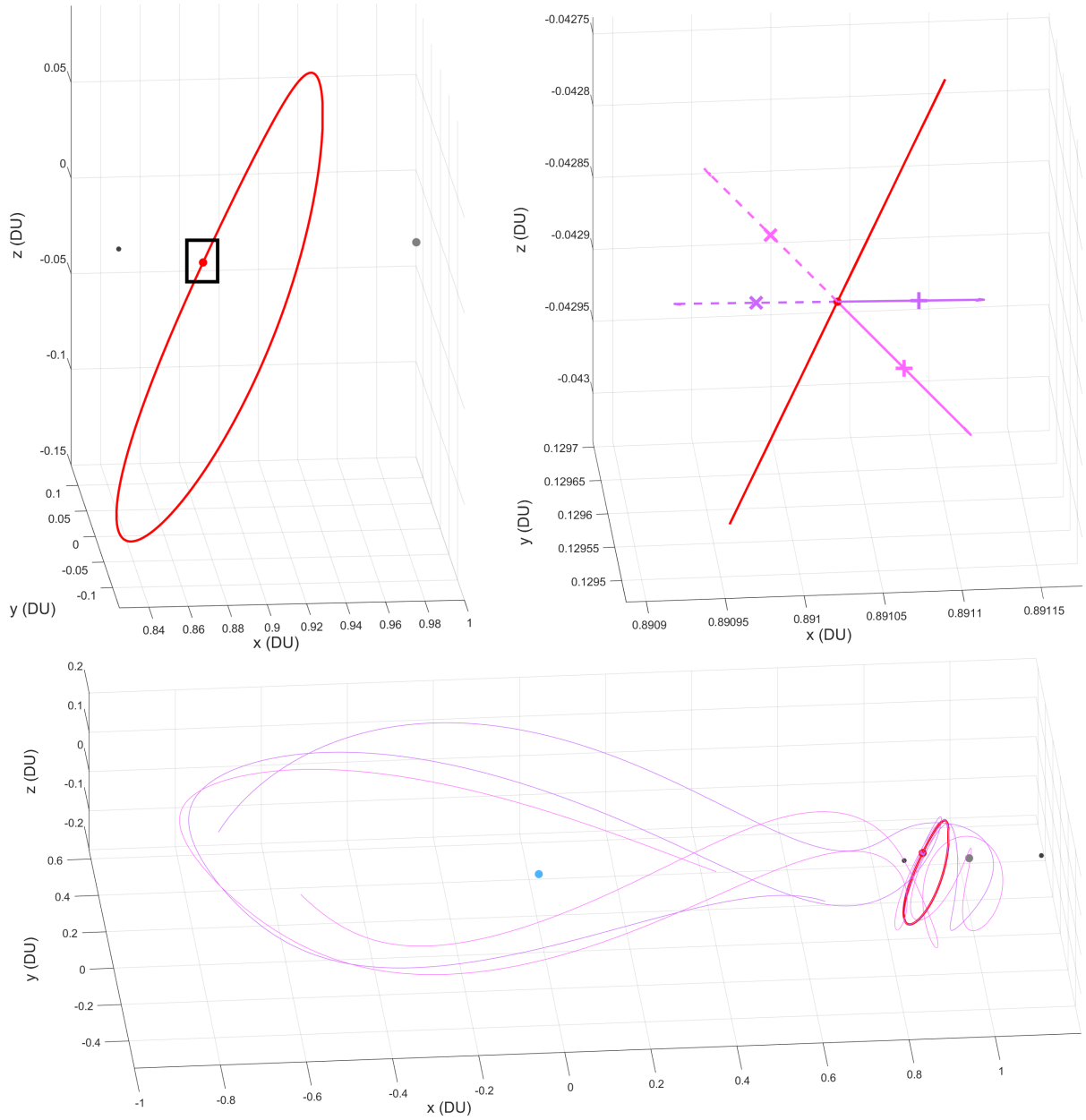

Figure 2.7: First Part of Procedure for Calculating Manifolds of an Orbit. Top left: L_1 (black dot) halo orbit (red line) used. Point P_1 (red dot) which $\boldsymbol{M}$ was calculated for is highlighted in the black box. Top right: Zoomed in view of P_1. The direction of the monodromy matrix's stable and unstable eigenvectors are shown with magenta and purple lines, respectively. For these eigenvectors, solid and dashed lines indicate the direction of the $\vec{v}_i$ and $-\vec{v}_i$, respectively. "+" and "x" represent the states on the manifolds for the positive and negative steps, respectively, with a step size of $d = 25$ km. Bottom: Manifold trajectories that represent the global manifolds for this point on the orbit, obtained from propagating the four states on the manifolds in time. Stable and unstable manifold trajectories are shown with magenta and purple lines, respectively. Each trajectory was propagated for ± 10 TU.

This method is referred to as the discrete geodesic evolution (GDE) technique [21]. Multiple points (n_p points) are selected around the initial orbit. At each of these points the monodromy matrix and its eigenvalues and eigenvectors are calculated. Two states on the stable manifold and two states on the unstable manifold are determined for each of the points on the orbit using Equation 2.45 and Equation 2.46. So, there are $2n_p$ states on the orbit's local stable manifold and $2n_p$ states on the orbit's local unstable manifold. Each of those $4n_p$ states on the manifolds are then propagated, and the collection of the resulting trajectories are used to represent the invariant stable manifold and unstable manifold of the orbit.

When determining the eigenvectors of the monodromy matrix at each point on the orbit, one of two methods could be employed. The first is to take the other states on the orbit and determine the eigenvectors of the monodromy matrix by propagating the 42 differential equations for each of those points as discussed in Section 2.1.3. The second method, which is more efficient, involves performing the process discussed in Section 2.1.3 for one point on the orbit, then using the equation below to determine the eigenvectors of the monodromy matrix for other points on the same orbit [8].

$$\vec{v}_i(\vec{X}_1^a) = \mathbf{\Phi}(t, t_0)\ \vec{v}_i(\vec{X}_0^a) \tag{2.47}$$

where $\vec{v}_i(\vec{X}_0^a)$ is the eigenvector at the original point and the $\vec{v}_i(\vec{X}_1^a)$ is the eigenvector at the new point on the orbit. So, the eigenvectors of the monodromy matrix are different for each point on the orbit. However, as stated previously, the eigenvalues of the monodromy matrix are the same regardless of what point on the orbit is used to calculate the monodromy matrix. The same process that was used in Figure 2.7 was repeated for 49 other points on the same L_1 halo orbit. The results are shown in Figure 2.8.

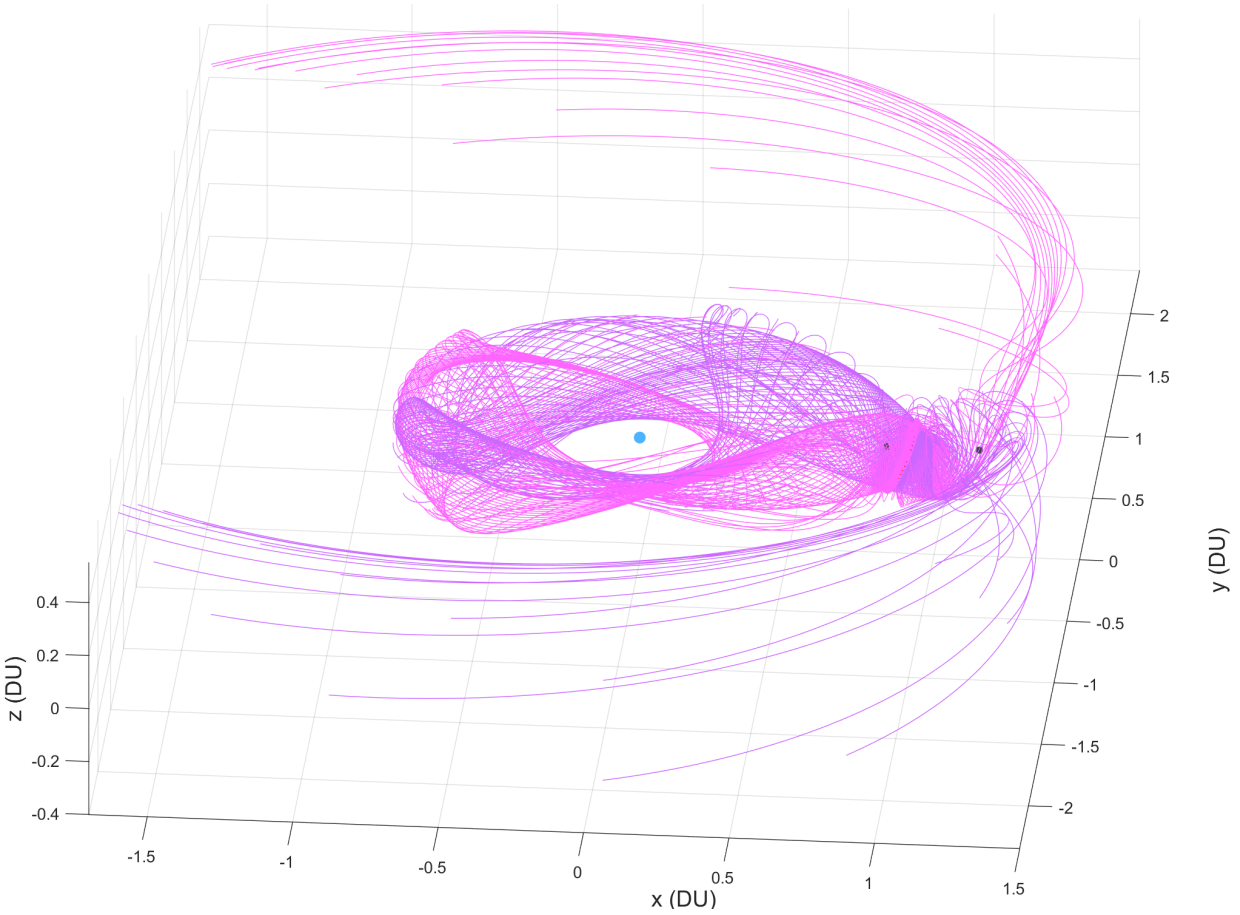

Figure 2.8: Calculating the Stable and Unstable Manifolds for an Orbit. Manifold trajectories that represent the global manifolds for this orbit were obtained by propagating states on the local manifolds in time. The states on the local manifolds were obtained for 50 points on the orbit, so there are 100 stable manifold trajectories and 100 unstable manifold trajectories shown in this figure. Stable and unstable manifold trajectories are represented by magenta and purple lines, respectively. Each trajectory was propagated for ± 10 TU. The process used for each of the 50 points on the orbit is demonstrated in Figure 2.7.

2.2.3 Poincaré Sections & Maps

A Poincaré section, represented by Σ, is one useful tool for analyzing dynamical systems that can be chaotic. A Poincaré section is a representation of the motion of a continuous time dynamical system at discrete times [43, 50]. Representing the system at discrete times reduces the dimensionality of the motion compared to the motion in the continuous time system, i.e. for a n degree of freedom system, a Poincaré section is of dimension $D \leq n$ [43]. The discrete times for which a Poincaré section represents the system could be based on many

different types of conditions, like certain specified times, or based on when a condition for the state is met, e.g. when states on trajectories have a certain value of x [50]. Representing a system with this second type of Poincaré sections can be thought of as observing the system while one of the n variables of the state space is fixed [51].

In this analysis, Poincaré sections of this second type will be used. Instead of representing a group of trajectories by their states at all times, that group of trajectories will be represented by only the states on those trajectories that have meet a certain condition. For example, only the states where $x = x_{val}$ will be selected. In the discrete time representation of a trajectory with this Poincaré section, to fully describe a state on the trajectory, only five state elements are needed instead of six (for the previous example: y, z, $\dot{x}$, $\dot{y}$, and $\dot{z}$). So, using Poincaré sections to represent trajectories at discrete times decreases the dimensionality of trajectories' motion, which also decreases the complexity of visualizing and processing the motion of the trajectories. Also, because the Jacobi constant is a conserved quantity in the CR3BP, if the value of C for a trajectory is known, just four of the five remaining elements need to be specified to completely define a state on the trajectory.

Poincaré sections are directional, and the direction of a given Σ will be represented by $\hat{\Sigma}$. In other words, the direction a trajectory crosses Σ matters. For the previous example, states on trajectories where $x = x_{val}$ are what are represented by the Poincaré section. But, there are Σ crossings where the states on trajectories have $\dot{x} > 0$ and others that have $\dot{x} < 0$. Because Poincaré sections are directional, only states with either $\dot{x} > 0$ or $\dot{x} < 0$, but not both, can be represented by a single Poincaré section. States should be represented by Poincaré sections that are "transverse to the vector field" at those states [43]. In other words, for a state s on Σ, motion of that state in time does not just remain in Σ, or $\vec{f}(s) \cdot \hat{\Sigma} \neq 0$. For the previous example, states on Σ (states with $x = x_{val}$) with $\dot{x} = 0$ should be avoided.

If an initial condition with the state s on Σ is propagated forward in time, the path might cross Σ again with the state $P(s)$. It is possible that propagating s in time could result in a

path that crosses Σ multiple times. If multiple sets of initial conditions on Σ are generated, propagated in time, and those crossings are recorded, useful information about the dynamics of the system can be obtained. This process will generate what is known as a Poincaré map, because the initial conditions s on Σ map to $P(s)$ [51]. A demonstration of this process is shown in Figure 2.9 which is based off of diagrams from Ross [51] and Vaquero [52].

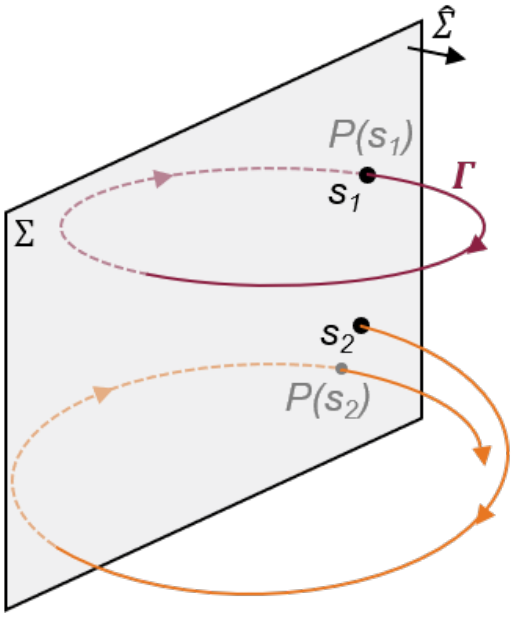

Figure 2.9: General Poincaré Map. This figure is based off of diagrams from Ross [51] and Vaquero [52]. Black dots are initial conditions (ICs). Gray dots are crossings of the Poincaré section Σ. Notice how only crossings that are in the direction of $\hat{\Sigma}$ are recorded. The orange trajectory has an IC s_2, and the trajectory crosses Σ again at the state $P(s_2)$. The maroon trajectory is a periodic orbit Γ with an IC of s_1. Notice how $P(s_1)$ is at s_1 for Γ. While both ICs shown here are on Σ because this figure represents a mapping, for a Poincaré section, there is no reason why ICs used to determine crossings of a Σ have to be a state on Σ.

2.3 Optimal Control & Differential Corrections

Designing the most efficient (in terms of propellant expenditure or ΔV) continuous-time transfer between two orbits can be viewed as an optimal control problem (OCP). As discussed in Section 1.2, there are many examples of OCPs in astrodynamics, as well as in dynamics and engineering in general, besides transfers between two orbits in the CR3BP. The general

formulation of an OCP can be represented as:

$$\begin{aligned} \min_{u(t)} J \quad & \text{where} \quad J = \phi(t_f, x(t_f)) + \int_{t_0}^{t_f} L(x(t), u(t), t)dt \\ \text{such that} \quad & x(t_0) = x_0 \\ & \dot{x}(t) = f(t, x(t), u(t)) \qquad t_0 \leq t \leq t_f \\ & h(t, x(t), u(t)) \leq 0 \qquad t_0 \leq t \leq t_f \\ & h_{t_f}(t_f, x(t_f), u(t_f)) \leq 0 \end{aligned} \tag{2.48}$$

where $x(t)$ is the state, $u(t)$ is the control, $\dot{x} = f$ captures the dynamics model, t_i and t_f represent the initial and final times of the transfer, x_0 is the initial state, J is the total cost function which consists of a terminal cost (ϕ) and a cost that accumulates based on the path chosen (the integral term), h are the path constraints, and h_{t_f} are the terminal constraints [53, 54]. The form of the OCP for a transfer between two orbits can be represented as a two-point boundary-value problem (TPBVP) [3, 55]. The OCP can be formulated as a nonlinear programming (NLP) problem, and the formulation of a NLP problem can be represented as:

$$\begin{aligned} \min_{Y} \; & J(Y) \\ \text{such that} \quad & Y_{LB} \leq Y \leq Y_{UB} \\ & h(Y) \leq 0 \\ & g(Y) = 0 \end{aligned} \tag{2.49}$$

where Y are the variables whose values can be directly changed, $J(Y)$ is the cost function to be minimized, $h(Y)$ are inequality constraints, and $g(Y)$ are equality constraints [53, 54].

The variables Y often contain states of the transfer, $J(Y)$ is some scalar indicative of the propellant expenditure required for the transfer (e.g. mass of propellant needed, ΔV, etc.), and $g(Y)$ are the constraints that enforce the continuity of the transfer and that the transfer starts and ends at the appropriate points. The OCP can be formulated as a NLP problem by discretizing the transfer into a set of points along the trajectory using what is known as a "direct method", like with multiple shooting or collocation. A variety of existing NLP problem solvers that are capable of solving NLP problems of this scale can then be used [54].

2.3.1 Shooting Methods

A shooting method is one tool that can be used to solve TPBVPs. In its simplest form, a shooting method attempts to change variables to meet conditions. The variables that can be changed are known as free variables, and will be represented by $\vec{Y}_{FV}$. There are certain metrics that should be zero. These metrics are known as constraints, and will be represented by $\vec{G}_C$. The values of the free variables affect the values of the constraints. The values of the constraints cannot be directly changed, but the values of the free variables can be directly changed in an attempt to make the values of the constraints zero.

A good example of this problem is outlined in Section 3.2 of Schlei [21]. Consider someone throwing a dart at a target. The goal is to throw the dart in such a way, so that when the dart hits the target, it is in the center of the bullseye. The constraint, which should be zero, is the distance between the dart when it hits the target and the center of the bullseye. But the thrower cannot walk up to the target and directly put the dart in the bullseye (that would be cheating). So, the thrower cannot directly change the value of the constraint. The thrower can only change parameters associated with how they throw the dart, like what is the final speed of the dart when it is released, what angle is it thrown at, etc. So how the dart is thrown (the changeable parameters) are the free variables for this case. So, the thrower starts with an "initial guess" of how to throw the dart with an initial set of values

for the free variables. The dart is thrown with the initial values of the free variables, and the path of the dart follows the dynamics of the system (with gravity, air drag, etc.). The dart hits the target a certain distance away from the center of the bullseye. Then based on how far the dart was off from the bullseye (the value of the constraint), the thrower updates how they throw the dart (the free variables). They throw the dart again, the dart follows the dynamics, and hits the target a new distance away from the bullseye. The thrower repeats this process until the dart is within the ring of the bullseye, even if the dart is not in the exact center of the bullseye (the constraint is zero within some tolerance). While the dart example could be slightly modified to include an objective function, this example is a good representation of the general process used in a corrective scheme.

Types of Shooting Methods

Often times in orbital mechanics applications, shooting methods are used to correct trajectories. For example, the operator of a spacecraft starting at an initial state wants the spacecraft to end at some final state after some amount of time. For these kinds of examples, four types of shooting methods are frequently used: fixed-time single shooting, variable-time single shooting, fixed-time multiple shooting, and variable-time multiple shooting. A detailed discussion of these four types of shooting methods can be found in Section 2.4 of Pavlak [56]. Single shooting methods consist of a single segment that represents a single trajectory, while multiple shooting methods have multiple segments along a single trajectory. Fixed-time shooting methods have a set time for each of the segments, while variable time shooting methods allow for the time of each segment to be a free variable. Please note that a common convention is to represent free variables by the vector $\vec{X}$. In this document, instead of $\vec{X}$, $\vec{Y}_{FV}$ will be used to represent the free variables to avoid confusion between the representation of the free variables for a shooting method and a state vector in the dynamical system.

2.3.2 Applications of Shooting Methods

Constructing Periodic Orbits

Shooting methods can be used to obtain initial conditions for periodic orbits. A simplified overview of this process will be provided in this section. A detailed discussion of how to obtain initial conditions for a variety of periodic orbits in the CR3BP can be found in Grebow [1].

When an accurate guess of a periodic orbit's initial conditions and period are known, even if the orbit does not possess symmetry, shooting methods can be used. For a state on a periodic orbit, after one period of that orbit, the state should be the same. Again, assuming a sufficiently accurate guess of the initial conditions and period are known, a fixed-time single shooting method can be used. Technically any of the four types of shooting methods could be used, but the use of a fixed-time single shooting method will be discussed here. In this case the free variables are the six elements of the initial state on the orbit. That initial condition is propagated using the equations of motion from the initial time t_i to a final time which is fixed at $t_f = t_i + T$. At this final time, the final state should be the same as the initial state, so there are six constraints for this problem (one for each element of the state vector). The formulation of this problem is represented by the following equation:

$$\vec{Y}_{FV} = \vec{X}_i = \begin{bmatrix} x_i \\ y_i \\ z_i \\ \dot{x}_i \\ \dot{y}_i \\ \dot{z}_i \end{bmatrix} \qquad \vec{G}_C = \vec{X}_i - \vec{X}_f = \begin{bmatrix} x_i - x_f \\ y_i - y_f \\ z_i - z_f \\ \dot{x}_i - \dot{x}_f \\ \dot{y}_i - \dot{y}_f \\ \dot{z}_i - \dot{z}_f \end{bmatrix} \quad \text{where} \quad \vec{X}_f = \phi_{t:t_i \to t_f}(\vec{X}_i) \tag{2.50}$$

For orbits demonstrating symmetry, the formulation of the problem can be modified. If a periodic orbit has symmetry, the equations of motion do not have to be integrated to a specified time, like the orbit's period. Instead, the equations of motion can be integrated from the initial condition until a certain state condition is met where the symmetry of the orbit is identifiable, and constraints related to the symmetry can be evaluated.

Constructing Lyapunov Orbits

Lyapunov orbits are 2D ($z = \dot{z} = 0$ for all time) and are symmetrical about the x-axis. When crossing the x-axis ($y = 0$ at these points), the velocity is purely in the $\pm$ y direction ($\dot{x} = 0$ at these points). So an initial guess for a state on a Lyapunov orbit that is crossing the x-axis can be represented as: $\vec{X}_i = [x_i \; 0 \; 0 \; 0 \; \dot{y}_i \; 0]^T$. Notice there are only two free variables (x_i and $\dot{y}_i$) instead of six. But, if the initial condition for a Lyapunov orbit with a specific Jacobi constant value is desired, then there is only free variable as for each value of x_i, there is only one value of $\dot{y}_i$ that satisfies Equation 2.3 (assuming the direction of the crossing is known, i.e. if $\dot{y}_i$ is positive or negative). From this initial condition, the state can be propagated, until the trajectory crosses the x-axis again (i.e. when the state meets a certain condition). When crossing the x-axis again, the state should only have a velocity component in the $\pm$ y direction. Relevant expressions for the problem of obtaining an initial condition for a Lyapunov orbit with a specific C value are:

$$\vec{X}_i = \begin{bmatrix} x_i \\ 0 \\ 0 \\ 0 \\ \dot{y}_i \\ 0 \end{bmatrix} \qquad \vec{X}_f = \begin{bmatrix} x_f \\ 0 \\ 0 \\ \dot{x}_f \\ \dot{y}_f \\ 0 \end{bmatrix} \qquad \text{where} \qquad \begin{gathered} \vec{X}_f = \phi_{t:t_i \to t_{y=0}}(\vec{X}_i) \\ \text{and} \\ \dot{y}_i = \sqrt{\frac{2(1-\mu)}{|x_i - r_1|} + \frac{2\mu}{|x_i - r_2|} + x_i^2 - C} \end{gathered} \tag{2.51}$$

One formulation of the problem that can be used in the shooting method is:

$$\vec{Y}_{FV} = \begin{bmatrix} x_i \end{bmatrix} \qquad \vec{G}_C = \begin{bmatrix} 0 - \dot{x}_f \end{bmatrix} \tag{2.52}$$

As there are Lyapunov orbits about each of the three collinear Lagrange points, the final value of x_i found by the shooting method may depend on the value of x_i in the initial guess. So, if the initial condition for an L_1 Lyapunov orbit with a certain C value is desired, the initial guess for the value of x_i should be closer to the actual x_i for the L_1 Lyapunov orbit, not the actual x_i for the L_2 or L_3 Lyapunov orbits. In other words, in a shooting scheme, how close the initial guess is to the desired final value(s) can be a significant determiner of the likelihood of finding an appropriate solution.

Constructing Halo Orbits

Another example of orbits that demonstrate symmetry are halo orbits. Halo orbits are 3D and are symmetrical about the x-z plane. When crossing the x-z plane ($y = 0$ at these points), the velocity is purely in the $\pm$ y direction ($\dot{x} = \dot{z} = 0$ at these points). An initial guess for a state on a halo orbit that is in the x-z plane can be represented as: $\vec{X}_i = [x_i \; 0 \; z_i \; 0 \; \dot{y}_i \; 0]^T$. So there are only three free variables instead of six. But, if the initial condition for a halo orbit with a specific Jacobi constant value is desired, then there are only two free variables as the three variables x_i, z_i, and $\dot{y}_i$ are related by one equation, Equation 2.3 (assuming the direction of the crossing is known, i.e. if $\dot{y}_i$ is positive or negative). When propagating this initial condition, instead of stopping the propagation after a set time, the propagation will be stopped when the trajectory crosses the x-z plane again. When crossing the x-z plane again, the trajectory's state should only have a velocity component in the $\pm$ y direction. Relevant expressions for the problem of obtaining an initial condition for a halo orbit with a specific C value are in Equation 2.53.

$$\vec{X}_i = \begin{bmatrix} x_i \\ 0 \\ z_i \\ 0 \\ \dot{y}_i \\ 0 \end{bmatrix} \quad \vec{X}_f = \begin{bmatrix} x_f \\ 0 \\ z_f \\ \dot{x}_f \\ \dot{y}_f \\ \dot{z}_f \end{bmatrix} \quad \text{where} \quad \begin{array}{c} \vec{X}_f = \phi_{t:t_i \to t_{y=0}}(\vec{X}_i) \\ \text{and} \\ \dot{y}_i = \sqrt{\frac{2(1-\mu)}{\sqrt{(x_i-r_1)^2+z_i^2}} + \frac{2\mu}{\sqrt{(x_i-r_2)^2+z_i^2}} + x_i^2 - C} \end{array} \tag{2.53}$$

One formulation of the problem that can be used in the shooting method is:

$$\vec{Y}_{FV} = \begin{bmatrix} x_i \\ z_i \end{bmatrix} \qquad \vec{G}_C = \begin{bmatrix} 0 - \dot{x}_f \\ 0 - \dot{z}_f \end{bmatrix} \tag{2.54}$$

The accuracy of the initial guess used to find the initial condition of a halo orbit can be significant, just as was the case for finding the initial condition of a Lyapunov orbit. As halo orbits are 3D, it can be more difficult for a numerical correction scheme to converge compared to the 2D case with Lyapunov orbits. As a result, the accuracy of the initial guess is even more significant when obtaining initial conditions for halo orbits. As was the case for the Lyapunov orbits, there are halo orbit families about L_1, L_2, and L_3.

Constructing Orbital Transfers

For a numerical optimizer there are three types of parameters:

- Free Variables: Variables whose values the optimizer can directly modify.
- Constraints: Conditions, represented by an equality or inequality, that must met.
- The Cost Function: A result whose value should be minimized.

Shooting methods applied with a numerical optimizer can also be used to construct transfers between orbits. For any valid transfer between two orbits, the transfer must be continuous in position. A transfer between two orbits must minimize the ΔV required in order to be considered an optimal transfer (in terms of propellant expenditure). At discrete points, a change in the velocity (ΔV) can be accomplished by using maneuvers like burns, that are assumed to be instantaneous. Under this assumption, by minimizing the ΔV of a certain transfer, the amount of propellant required to perform that transfer is also minimized. The variables that can directly be changed by the optimizer are the states at points along the transfer path and the times between the points. In this sense, the process of constructing an optimized transfer between two orbits using a numerical optimizer is similar to the process used in a variable-time multiple shooting method. Details about how transfers between orbits are optimized in this analysis are discussed in Section 3.2.

Chapter 3

Methodology & Approach

3.1 Transfers Using Manifolds

As shown previously in Section 2.2.2, states on the stable and unstable manifolds for a point on a periodic orbit are obtained by slightly changing the state vector at that point. Part of this change (specifically the change in velocity) can be thought of as a maneuver, or burn, with a small ΔV cost. A trajectory obtained by propagating a state on an orbit's unstable manifold forward in time will move away from that orbit and a trajectory obtained by propagating a state on an orbit's stable manifold forward in time will move towards that orbit. Suppose that a spacecraft in one orbit is trying to get to another orbit. If a trajectory on the initial orbit's unstable manifold intersects (in terms of position) a trajectory on the desired orbit's stable manifold, then the path that is formed by connecting those manifold trajectories could be viewed as continuous in terms of position. If the two trajectories also have similar velocities at the intersection point (i.e. a small burn is needed at that point), then the path formed by connecting those manifold trajectories could also be viewed as a good representation of a low-cost transfer path between the two orbits. So, if an operator of a satellite m_s wants it to transfer from an initial orbit (Orbit 1) to a desired orbit (Orbit 2), a good guess of a low ΔV transfer path can be approximated by using the manifold trajectories of Orbit 1 and Orbit 2 that intersect each other with similar velocities. A transfer that uses manifolds in this way will be referred to as a "manifold transfer".

A conceptual diagram depicting a manifold transfer is shown in Figure 3.1, and an outline

of such a transfer is described (in chronological order) in the list below.

1. Start at Point A.
2. Follow the path of Segment 1 from Point A to Point MT_1.
3. Perform an instantaneous burn to change the the state of m_s from the state at Point MT_1 to the state at Point MT_2.
4. Follow the path of Segment 2 from Point MT_2 to Point B.
5. End at Point B.

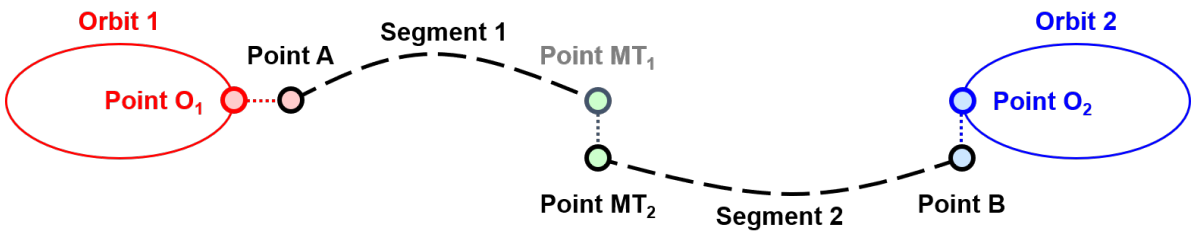

Figure 3.1: High-Level Diagram of an Orbit Transfer Using Manifolds. The transfer starts at Point A and ends at Point B. Small dotted lines indicate instantaneous changes in the state. Orbit 1 (red) is the initial orbit and Orbit 2 (blue) is the final desired orbit. The transfer goes from left to right with the transfer consisting of all points & segments in black. Note that Point O_1, Point MT_1, and Point O_2 are not on the actual transfer because the states are instantaneously changed from the states at those points to the states at Point A, Point MT_2, and Point B, respectively.

The important points of a manifold transfer are:

- Point A: The state obtained by stepping onto the unstable manifold from a point that is on Orbit 1 (Point O_1) using Equation 2.46.
- Point B: The state obtained by stepping onto the stable manifold from a point that is on Orbit 2 (Point O_2) using Equation 2.45.
- Point MT: The transition point between the manifolds. The point where the unstable manifold trajectory obtained from propagating Point A forward in time, and the stable

manifold trajectory obtained from propagating Point B backward in time, intersect (in terms of position), and have similar velocities.

  - Point MT_1: The state along the unstable manifold trajectory obtained from propagating Point A forward in time that corresponds to Point MT.
  - Point MT_2: The state along the stable manifold trajectory obtained from propagating Point B backward in time that corresponds to Point MT.

The important segments of a manifold transfer are:

- Segment 1: m_s follows this path from Point A to Point MT_1. Segment 1 is the trajectory obtained from propagating the state vector of Point A forward in time until Point MT_1 is reached.
- Segment 2: m_s follows this path from Point MT_2 to Point B. Segment 2 is the trajectory obtained from propagating the state vector of Point B backward in time until Point MT_2 is reached.

3.1.1 Identifying Intersections of Manifold Trajectories

For this analysis, transfers where the transition point between the two manifold trajectories is near the Moon were of interest as a significant number of intersections between the manifold trajectories are expected to occur in that space. For two halo orbits, the unstable manifold of Orbit 1 and the stable manifold of Orbit 2 were calculated for 50 points on each orbit and are shown in Figure 3.2. Knowledge of the exact initial conditions of these two orbits are not necessary to identify the pattern in the figure, but are given in Section 4.2.1. As can be seen by looking at the figure, identifying all points where the manifold trajectories intersect is not easy. This analysis will specifically focus on identifying intersections in the region around the Moon.

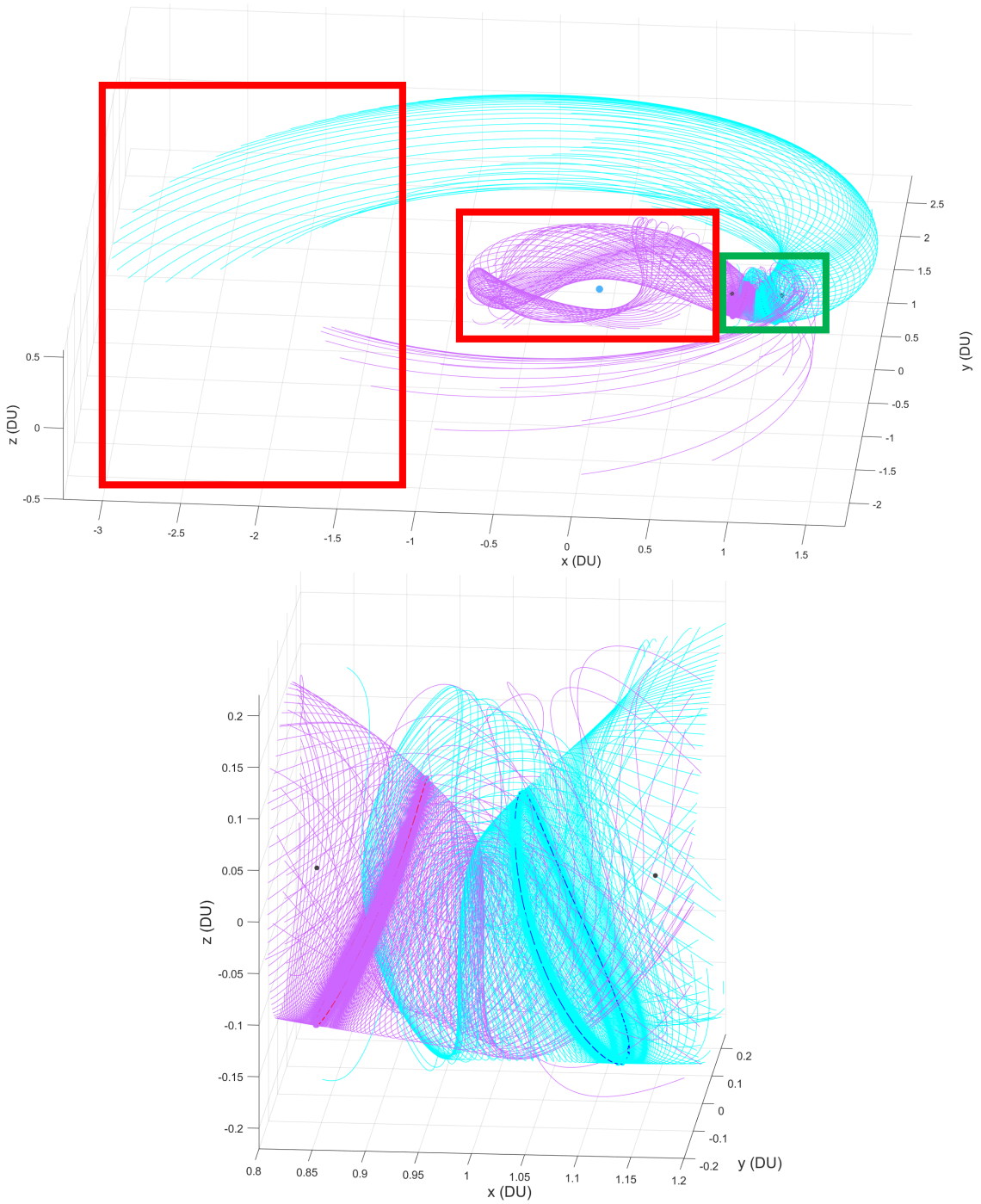

Figure 3.2: Manifolds of Two Halo Orbits. Purple and cyan lines are Orbit 1 unstable and Orbit 2 stable manifold trajectories, respectively. The light blue dot is the Earth, the light gray dot is the Moon, and the dark gray dots are L_1 and L_2. 50 points on each orbit were used with a step of $d = 25$ km. Each manifold trajectory was propagated for 10 TU. Top: Full view of the manifold trajectories. Regions outlined in red could contain possible manifold intersections (depending on the step size and propagation time) that will not be considered in this analysis. The region outlined in green contains possible manifold intersections that will be considered, and a zoomed-in view of this approximate region is displayed on the bottom. Bottom: View of the manifold trajectories focused on the space around the Moon.

There are many points where the trajectories could intersect in terms of position, which is one reason for the complexity in identifying all of the intersections. For this analysis, all manifold trajectories were propagated from 0 TU to ± 10 TU while storing the state vector of each manifold trajectory every 0.001 TU. As a result, each manifold trajectory in Figure 3.2 consists of 10,001 points. While Figure 3.2 shows the manifolds for only 50 points on each orbit, in the actual analysis, 1,000 points along each orbit were used (1,000 points with positive and negative steps, so 2,000 manifold trajectories for each orbit) to make sure the behaviors of the manifold trajectories for all points on both orbits were captured. To directly compare all the points on the manifold trajectories, each of the 20,002,000 Orbit 1 manifold trajectory points would need to be compared with each of the 20,002,000 Orbit 2 manifold trajectory points. This direct comparison would be computationally intensive as calculations for just over 4×10^{14} pairs of points would be required.

If the x-value, y-value, or z-value of the manifold transition point was fixed, the complexity in identifying all intersections of the manifold trajectories would be greatly reduced as only a fraction of the points on each manifold trajectory would need to be considered. The x-value of the manifold transition point x_{MT} can be fixed by creating a Poincaré section Σ at $x = x_{MT}$, for a selected value of x_{MT}. A manifold trajectory is then propagated and every time the trajectory crosses Σ, the trajectory's state vector is recorded. Repeating the previous step for all of the other manifold trajectories will result in a set of state vectors corresponding to all points on the manifold trajectories where the x-value is the same as x_{MT}. The y- and z-values of each state vector in that set can then compared with the y- and z-values of the other state vectors in that set to determine if there are any pairs of trajectory points on Σ that are "close enough" (within a tolerance limit). Of the pairs of trajectory points on Σ with positions that are "close enough", a low-cost transfer path can be determined by identifying the point on Σ from an Orbit 1 unstable manifold trajectory and the point on Σ from an Orbit 2 stable manifold trajectory that have the smallest magnitude velocity difference. This procedure is shown for one value of x_{MT} in Figure 3.3 and Figure 3.4.

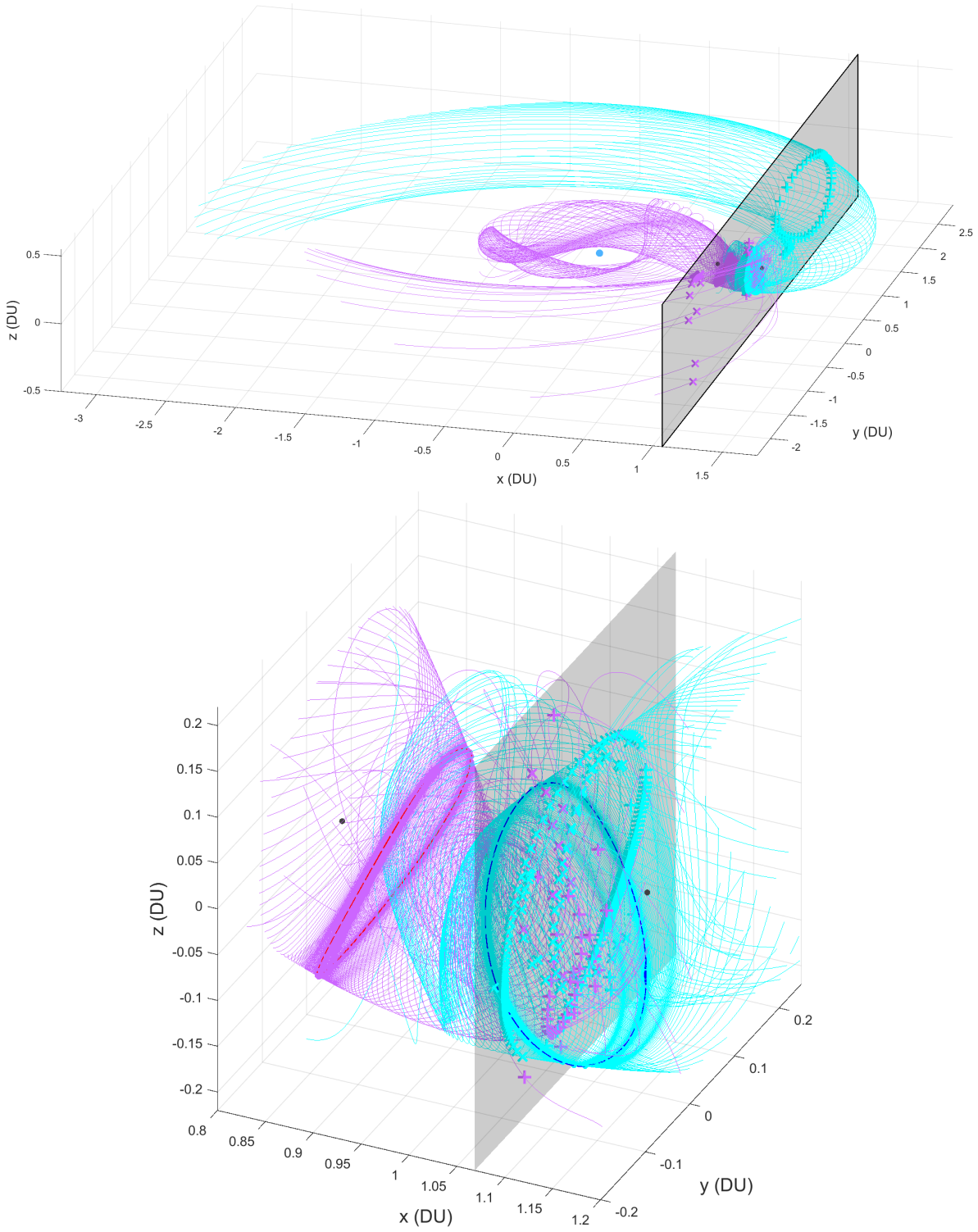

Figure 3.3: Restricting Transfers to Have Discrete Values of x_{MT} using Poincaré Sections. The images above represent crossings of a Poincaré section by manifold trajectories for two halo orbits. The Poincaré section Σ (the gray plane) is located at $x = 1.0687$ DU. To generate these images, 1,000 points on each orbit were used, but as to not crowd the images, trajectories from only 50 of those points are shown here. Top: View of all crossings of Σ. Bottom: View of the crossings of Σ that are in the region around the Moon.

Focusing on the region close to the Moon, the states at each crossing (bottom of Figure 3.3) are represented on a position plot and a velocity plot in Figure 3.4. To identify the best valid transfer, the states with positions that are "close enough" (Figure 3.4 - left), and have the smallest magnitude difference in velocity (Figure 3.4 - right), need to be identified.

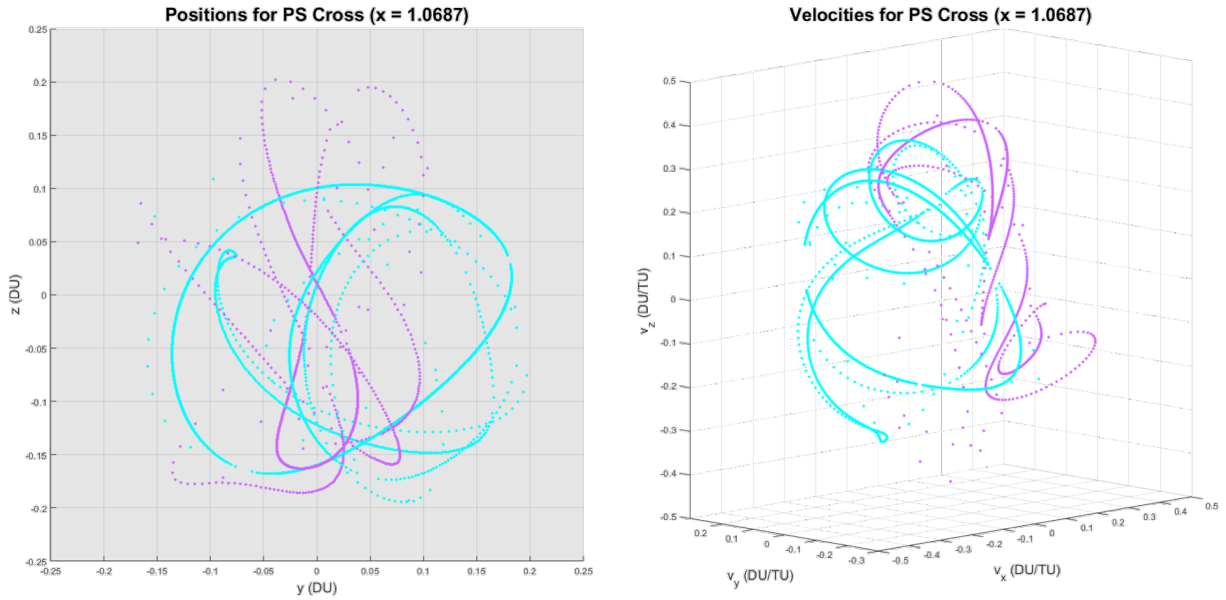

Figure 3.4: Finding the Best Manifold Transfer for a Set Value of x_{MT}. The images above represent crossings of a Poincaré section Σ by manifold trajectories for the same two halo orbits and Σ as in Figure 3.3. These images show the crossings of all 2,000 Orbit 1 manifold trajectories and all 2,000 Orbit 2 manifold trajectories (using 1,000 points on each orbit, with positive and negative steps, results in 2,000 manifold trajectories for each orbit). Position components (left) and velocity components (right) of the state at every crossing of Σ.

3.1.2 Determining the Best Manifold Transfers

However, that procedure restricted the transition between the manifold trajectories to occur at one specific x-value. If that procedure is repeated for multiple x-values, a set of low-cost transfers can be generated. This process will hopefully be sufficient to identify a transfer that is reasonably similar to the best transfer that would be obtained by directly comparing all the manifold points with each other individually, while being significantly more computationally efficient. A diagram of this process is provided in Figure 3.5.

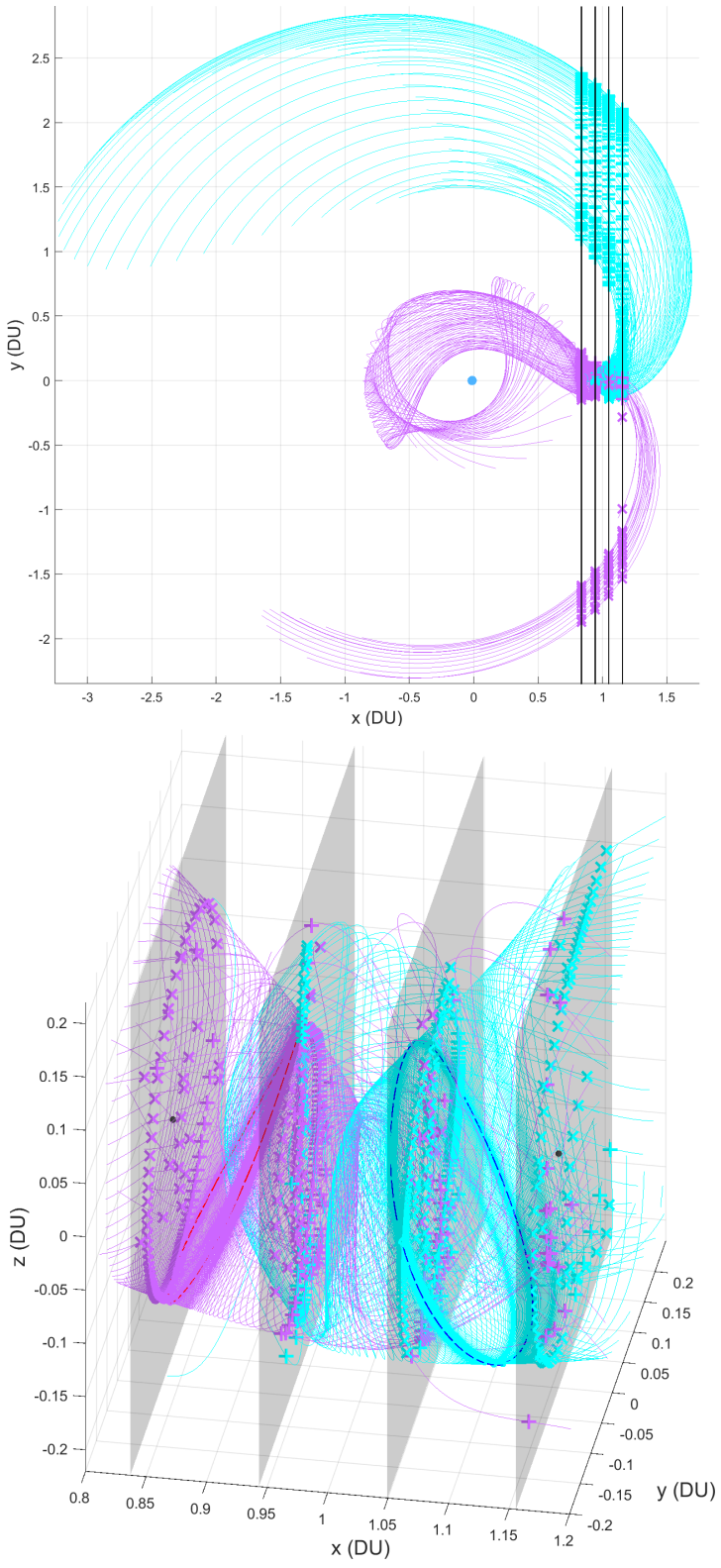

Figure 3.5: Determining the Best Manifold Transfers for a Set of x_{MT} Values using Poincaré Sections. The two images above represent crossings of four Poincaré sections by the manifold trajectories from Figure 3.3. The four values of x_{MT} were equally spaced between the x-values of L_1 and L_2. Top: View of all crossings of the Poincaré sections. Bottom: View of the crossings of the Poincaré sections that are in the region around the Moon.

By constructing the best manifold transfer at each value of x_{MT}, the best manifold transfer overall can be selected based on which of the best manifold transfers has the lowest ΔV. For the remainder of this document, the phrase "best manifold transfer" refers to the best valid manifold transfer at each selected value of x_{MT}, while "best manifold transfer overall" refers to the best manifold transfer with the lowest ΔV at the manifold transition point, compared to all the other best manifold transfers. After the best manifold transfer at each value of x_{MT} is determined, each transfer is analyzed to determine if the transfer path crashes into the Moon at any point. For the best transfer with the manifold transition point at the first selected value of x_{MT}, the distance between each point along that transfer path and the center of the Moon is calculated. If at any point along that transfer path, the distance between the path point and the center of the Moon is less than the radius of the Moon, that transfer is classified as invalid. This process is then repeated for the remaining selected values of x_{MT}.

If enough values of x_{MT} are selected, hopefully this process will be sufficient to identify a transfer that is similar to the best transfer overall that would be obtained by directly comparing each and every individual state along Orbit 1's unstable manifold trajectories with each and every individual state along Orbit 2's stable manifold trajectories.

3.2 Correcting Transfers from Manifolds

Manifold transfers can be used as approximations of low ΔV transfers between orbits. However, there are still some aspects of the transfer that could be improved. For instance, the first and last points on the manifold transfer are not actually on the initial and final orbits; those points are on the manifolds of the orbits. While technically once on an orbit's manifold the trajectory should eventually reach the orbit, it will only do so as the magnitude of time approaches infinity (as $t \to -\infty$ for an unstable manifold, and as $t \to \infty$ for a

stable manifold). One correction that could be made to each manifold transfer is to force the transfer path to start and end on the actual orbits, instead of on their manifolds, while maintaining a similar transfer time of flight (TOF) as the original manifold transfer.

One other issue associated with the manifold transfer is the allowed discontinuity when transitioning between Orbit 1's unstable manifold and Orbit 2's stable manifold. At the manifold transition point, there had to be a "close enough" tolerance between the two manifold trajectories that were being compared. Another correction that could be made to each of the manifold transfers is to make the discontinuity at the manifold transition point closer to zero than the specified "close enough" tolerance, while still maintaining a transfer path that is similar to the original manifold transfer path.

3.2.1 Approach to Transfer Correction & Optimization

An optimization scheme can be used with a manifold transfer as an initial guess to obtain a better transfer. A manifold transfer consists of two parts: one part along Orbit 1's unstable manifold and one part along Orbit 2's stable manifold. To use a numerical optimization scheme, the manifold transfer must first be discretized into points which will be referred to as nodes. If n nodes are selected to represent the transfer, and if a scheme similar to a variable-time multiple shooting method is used, then there are $7n - 1$ variables that can be directly changed by the optimizer. These $7n - 1$ free variables will be the elements of the states at each node ($6n$ variables) and the durations of the segments between each sequential pair of nodes ($n - 1$ variables). Nodes that are not the first or last node will be referred to as interior nodes.

The scalar cost function in the optimization scheme is the sum of the individual ΔVs for each of the three instantaneous maneuvers, or burns. Instantaneous burns can occur: 1. when going from a state on Orbit 1 (the state at Point O_1) to the state at the beginning of the first segment of the transfer (the state of the first node), 2. when transitioning between the

manifolds, and 3. when going from the state at the end of the last segment of the transfer (the state of the last node) to a state on Orbit 2 (the state at Point O_2). The total cost of the transfer is the sum of the individual costs of each of the burns. Point O_1 is the point on Orbit 1 that produced the specific unstable manifold trajectory used in the manifold transfer. Point O_2 is the point on Orbit 2 that produced the specific stable manifold trajectory used in the manifold transfer. The ΔV of the first burn is the magnitude of the difference between the velocity of the first node and the velocity at Point O_1. The ΔV of the second burn is the magnitude of the difference between the velocity of the node that represents the manifold transition point and the velocity of the state obtained by propagating the previous node's state in time by the TOF of that segment. The ΔV of the third burn is the magnitude of the difference between the velocity of the last node and the velocity at Point O_2. So nine of the $7n - 1$ free variables are directly used to calculate the cost of the transfer.

Regarding constraints, one constraint will be used to ensure that the x-value of the interior node where the burn occurs is the same as the original x_{MT} value for the manifold transfer. Other than this first constraint, two types of constraints must be used: constraints that ensure the transfer begins and ends in the correct places, and constraints that ensure the transfer is continuous. For the first type of constraints: the first node will be constrained to have the same position, but not necessarily the same velocity, as Point O_1 (3 constraints), and the last node will be constrained to have the same position, but not necessarily the same velocity, as Point O_2 (3 constraints). There are also some conditions that must be met for the transfer consisting of the nodes to be continuous. The state (position and velocity) of the last node must be the same as the state obtained by integrating the state of the second to last node in time by the TOF between those two nodes (6 constraints). If a burn is allowed to occur at a given interior node, then the position of that node must be the same as the position that is obtained by integrating the state of the previous node in time by the TOF between the two nodes. In this analysis, only one interior node is allowed to have a burn: the node corresponding to the manifold transition point (3 constraints). If a burn is not

allowed to occur at a given interior node, then that node must have the same position and velocity as the position and velocity obtained by integrating the state of the previous node in time by the TOF between the two nodes ($6(n-3)$ constraints).

For the case of representing the transfer using three nodes, there is: one node at the initial time (Point 0), one node at the manifold transition point (Point 1), and one node at the final time (Point 2). For this case, position continuity must be enforced at the middle node, but full state continuity must be enforced at the final node. A high-level concept diagram of the variables, individual costs, and constraints of the optimization scheme that are used in the case when a transfer is represented by three nodes is shown in Figure 3.6.

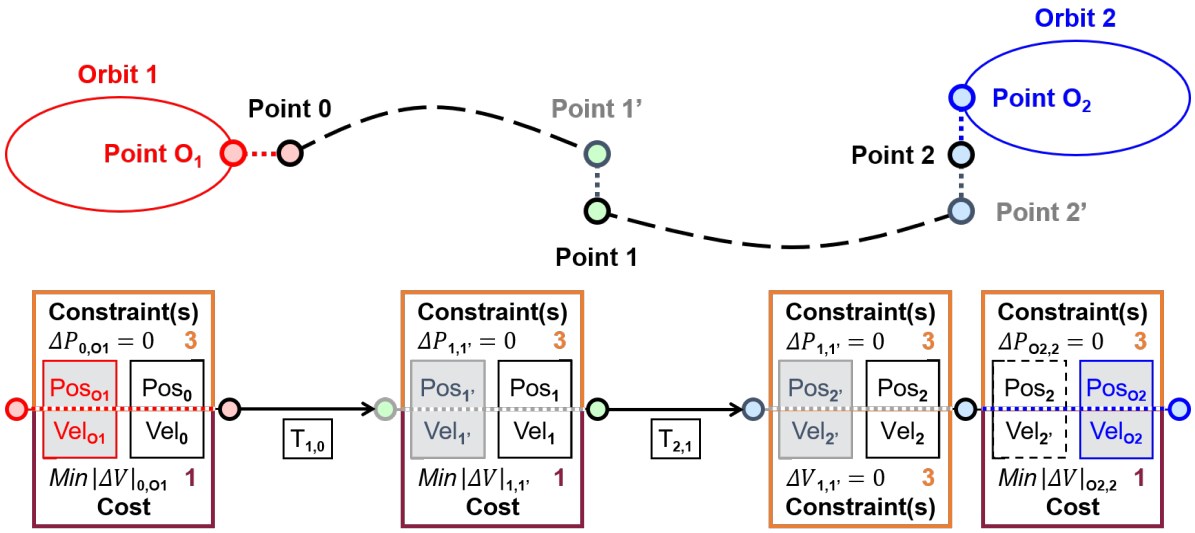

Figure 3.6: General Diagram of a Manifold Transfer Represented by Three Nodes Used in the Optimization Scheme. This diagram represents the numerical optimization scheme used, which can be viewed as a variable-time multiple shooting method implemented with a numerical optimizer. A NLP problem solver will be used. States at points with black outlines can be directly changed. States at points with any other color outline cannot be directly changed. Gray outlines correspond to points generated from propagating the black points forward in time and are used primarily in continuity constraints. Red and blue filled points are related to the initial and final points. $\Delta P_{i,j}$ is a vector with three elements, and represents the difference in position between Point i and Point j. $\Delta V_{i,j}$ is a vector with three elements, and represents the difference in velocity between Point i and Point j. $|\Delta V|_{i,j}$ represents the magnitude of $\Delta V_{i,j}$. Top: Diagram of transfer represented by three nodes (not to scale). Bottom: Breakdown of the constraints and objective for minimizing the ΔV for this type of transfer. Not depicted here is the constraint requiring that x-value of the interior node where the burn occurs is the same as the original x_{MT} value for the manifold transfer.

For the case of representing the transfer using more than three nodes, there is/are: n_1 nodes along the first part of the transfer before the manifold transition point (including one at the initial time), one node at the manifold transition point, and n_2 nodes along the second part of the transfer after the manifold transition point (including one at the final time). In this case, the total number of nodes is: $n = n_1 + n_2 + 1$. There is one total cost of the transfer, with nine of the $7n - 1$ free variables being used directly to calculate this cost. There are a total of $6n - 2$ constraints with: one constraint ensuring that the x-value of the interior node where the burn occurs is the same as the original value of x_{MT} for the manifold transfer (like before), six constraints fixing the start and end positions of the transfer (like before), three constraints ensuring position continuity at the manifold transition point (like before), and $6(n - 2)$ constraints ensuring continuity at all other nodes that are not the first node.

The states at Point O_1 and Point O_2 must be provided as 12 fixed values, as six values for each state are required. Initial guess values for each of the free variables must be provided as well. The number of these variables is directly related to how many nodes are used to discretize the manifold transfer. How these nodes are selected will be discussed in the next section.

3.2.2 Discretizing Trajectories

The manifold transfers are discretized into nodes (or discretization points) in two different ways. The first type of discretization will be referred to as "Type 1". The state on the unstable manifold trajectory that corresponds to the manifold transition point (Point MT_1 in Figure 3.1) is used as the state of the node at the manifold transition point. This selection results in no position or velocity discontinuity at the manifold transition point, but there is a discontinuity at the next point after the manifold transition point. The second type of discretization will be referred to as "Type 2" and, when integrating between the nodes, produces a transfer that is exactly the same as the manifold transfer. For Type 2, the

state on the stable manifold trajectory that corresponds to the manifold transition point (Point MT_2 in Figure 3.1) is used as the state of the node at the manifold transition point. This results in a position and velocity discontinuity at the manifold transition point, but there is no significant discontinuity at the next point. A diagram outlining how a manifold transfer is discretized with three nodes using both types is shown in Figure 3.7.

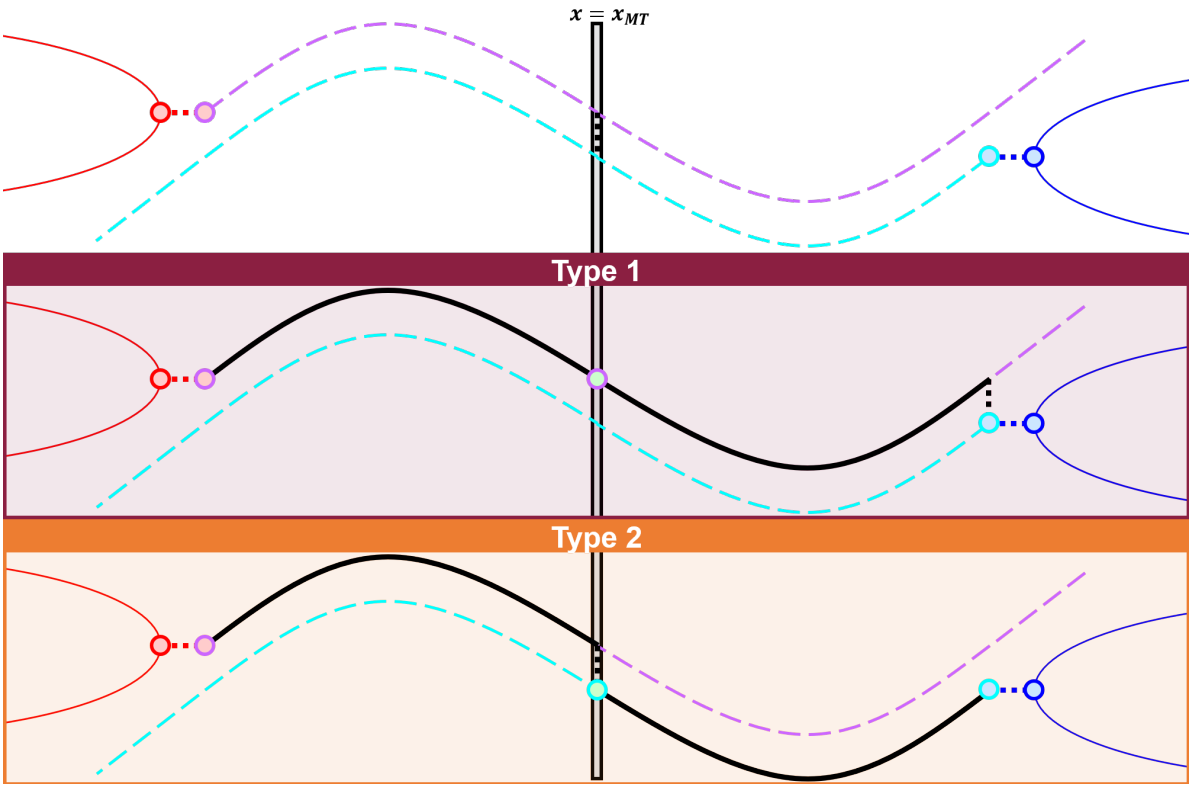

Figure 3.7: Discretization Type 1 and Type 2 of the Manifold Transfers ($n = 3$). Note these are high-level concept diagrams and are not to scale. The black line indicates the path that would be obtained by integrating each node (discretization point) in time to the next node. The black dashed line indicates the difference between the state obtained by integrating a node to what would be the next node, and the actual state of the next node. The manifold transition point is indicated by a light green dot. A purple or cyan outline indicates that the initial guess of the state at the node used in the correction scheme is the same as the state on the Orbit 1 unstable or Orbit 2 stable manifold trajectory, respectively. Top: Orbit 1 unstable manifold trajectory (purple) and Orbit 2 stable manifold trajectory (cyan) that are "close enough" at the manifold transition point, which is defined by x_{MT} (light gray), such that those trajectories can be used to construct a valid transfer from Orbit 1 (red) to Orbit 2 (blue). The red and blue dashed lines indicate the step from a point on an orbit (dots with light red/blue fills and red/blue outlines) to a point on that orbit's manifold (dots with light red/blue fills and purple/cyan outlines). Middle: Transfer from discretization "Type 1". Bottom: Transfer from discretization "Type 2".

A diagram outlining how a manifold transfer is discretized with more than three nodes using both types is shown in Figure 3.8.

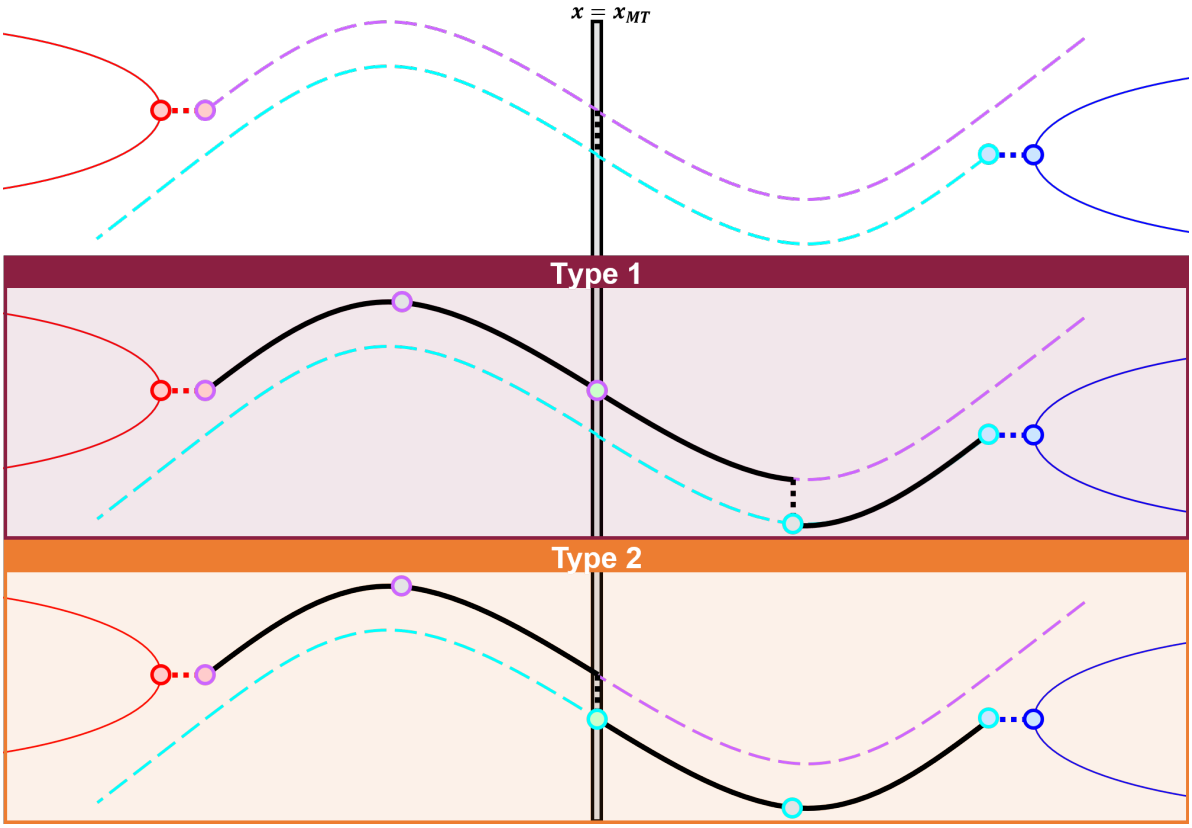

Figure 3.8: Discretization Type 1 and Type 2 of the Manifold Transfers ($n = 5$). Note these are high-level concept diagrams and are not to scale. The black line indicates the path that would be obtained by integrating each node (discretization point) in time to the next node. For more detail on what each shape and color represent, see Figure 3.7. Top: Orbit 1 unstable manifold trajectory (purple) and Orbit 2 stable manifold trajectory (cyan) that are "close enough" at the manifold transition point, which is defined by x_{MT} (light gray), such that those trajectories can be used to construct a valid transfer from Orbit 1 (red) to Orbit 2 (blue). The red and blue dashed lines indicate the step from a point on an orbit (dots with light red/blue fills and red/blue outlines) to a point on that orbit's manifold (dots with light red/blue fills and purple/cyan outlines). Middle: Transfer from discretization "Type 1". Bottom: Transfer from discretization "Type 2".

While Figure 3.8 only includes two nodes before and two nodes after the manifold transition point, the process shown in that figure could be extended to include significantly more nodes. The specific number of nodes used in this analysis will be discussed in the next section.

3.2.3 Determining the Best Corrected Transfers

For this analysis, each manifold transfer will be discretized using both discretization Type 1 and Type 2, and with three sets of nodes. Each discretization set will have a different number of nodes with: three nodes ($n_1 = n_2 = 1$) referred to as "Correction Set 1", five nodes ($n_1 = n_2 = 2$) referred to as "Correction Set 2", and seven nodes ($n_1 = n_2 = 3$) referred to as "Correction Set 3". As a result, the discrete-time representations of a single manifold transfer used in the optimization scheme can be obtained in six different ways. Each of the six representations are different, because even though they are based on the same manifold transfer, the values of the states at the nodes, and the transfer times between the nodes, depend on how the manifold transfer is discretized. These six unique ways of discretizing the manifold transfers will be referred to as "correction models". The six correction models used in this analysis are:

- Set 1 Type 1: $n = 3$ ($n_1 = n_2 = 1$), the state on Orbit 1's unstable manifold trajectory (Point MT_1) is used as the initial guess for the state at the manifold transition node.
- Set 1 Type 2: $n = 3$ ($n_1 = n_2 = 1$), the state on Orbit 2's stable manifold trajectory (Point MT_2) is used as the initial guess for the state at the manifold transition node.
- Set 2 Type 1: $n = 5$ ($n_1 = n_2 = 2$), the state on Orbit 1's unstable manifold trajectory (Point MT_1) is used as the initial guess for the state at the manifold transition node.
- Set 2 Type 2: $n = 5$ ($n_1 = n_2 = 2$), the state on Orbit 2's stable manifold trajectory (Point MT_2) is used as the initial guess for the state at the manifold transition node.
- Set 3 Type 1: $n = 7$ ($n_1 = n_2 = 3$), the state on Orbit 1's unstable manifold trajectory (Point MT_1) is used as the initial guess for the state at the manifold transition node.
- Set 3 Type 2: $n = 7$ ($n_1 = n_2 = 3$), the state on Orbit 2's stable manifold trajectory (Point MT_2) is used as the initial guess for the state at the manifold transition node.

Visual representations of these six correction models are provided in Figure 3.9.

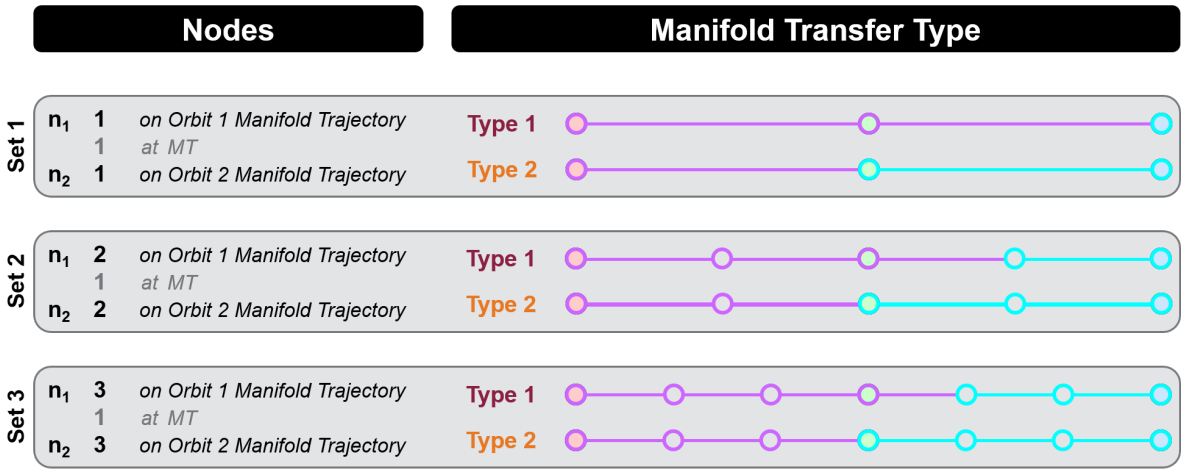

Figure 3.9: The Six Correction Models Used to Discretize Each Manifold Transfer. Note these are high-level concept diagrams and are not to scale. For more detail on what each color represents, see Figure 3.7. The path obtained when integrating a state from one node to the next is represented by either a magenta line (if the path is the same as a portion of a trajectory that is on Orbit 1's unstable manifold), or by a cyan line (if the path is the same as a portion of a trajectory that is on Orbit 2's stable manifold).

Each correction model's representation of the transfer will serve as a separate initial guess used in the optimization scheme. The six results obtained by using those six initial guesses are all corrected transfers that correspond to the one manifold transfer that was discretized into those six different initial guesses. Similar to the analysis performed on each manifold transfer, for each of the six corrected transfers, the distance between each point along those paths and the center of the Moon will be calculated. If at any point along those paths, the distance between the path point and the center of the Moon is less than the radius of the Moon, that transfer will be classified as invalid. If the magnitude of any of the constraints is greater than some specified tolerance, the corrected transfer will also be considered invalid.

Each of the other best manifold transfers will be discretized using the six correction models. If there are N_{BMT} best manifold transfers, then there will be $6N_{BMT}$ corrected transfers. Each of the corrected transfers will also be analyzed to determine if they are "valid" as described in the previous paragraph. The phrase "converged" will be used if a valid corrected transfer is obtained from a given correction model. Of the valid corrected transfers, the phrase "best

corrected transfer from Set 1" will refer to the valid corrected transfer that is from Set 1 Type 1 or Set 1 Type 2 with the lowest cost (the least total ΔV required). The phrases "best corrected transfer from Set 2" and "best corrected transfer from Set 3" can be defined similarly. Of the three transfers that are the best transfers from each set, the transfer with the lowest cost (the least total ΔV required) will be classified as the "best corrected transfer overall".

3.3 Methodology Summary

In summary, the best manifold transfer between two orbits will be identified at a number of specified x_{MT} values that are selected to be near the Moon. Each of these N_{BMT} best manifold transfers will then be discretized using six different corrections models. The $6N_{BMT}$ representations of the N_{BMT} manifold transfers will then be used as initial guesses in an optimization scheme. The best manifold transfers and the corrected transfers will be analyzed to make sure they do not crash into the Moon at any point. The corrected transfers will also be evaluated to determine if the nodes representing the transfer have a maximum constraint violation that is lower than a certain tolerance.

Before determining the best manifold transfers, the μ of the primary bodies, the units used in calculations, and the two orbits for the transfer must be defined. In the process used to determine the best manifold transfer, the number of points on each orbit, the magnitude of the step size d, and the maximum time of propagation must be specified when calculating the manifold trajectories. The type of coordinate (e.g. x, y, or z) used to restrict the manifold transition point, the range of x_{MT} (or y_{MT} or z_{MT}) values, and the number of transfers to determine (the number of x_{MT}, y_{MT}, or z_{MT} values) must also be specified. What position tolerance is "close enough" must also be specified.

When correcting the best manifold transfers, what NLP problem solver or optimizer to

use, and what characteristics it will have (e.g. the algorithm used, etc.), must be selected. The stopping criteria (e.g. the maximum number of allowed iterations and the maximum number of allowed function evaluations) and validity criteria (e.g. the maximum allowable constraint violation) must also be defined. The number of interior burn points allowed should be determined which, for this analysis, was fixed at one. Whether to use only a subset of the best manifold transfers should be considered as well. For this analysis, all of the best manifold transfers were used in the optimization scheme.

The key parameters that need to be defined to apply the methodology outlined in this chapter are listed in Table 3.1.

Environment	**Specific Transfer**
Dynamics	Orbits
μ	Orbit 1
Units	Orbit 2
Manifold Transfers	**Corrected Transfers**
Manifold Trajectories	Optimizer
Points on Orbit	Specific Optimizer Used
Magnitude of Step Size (d)	Stopping Criteria
Max Propagation Time	Bounds on variables Y
Restricting the MTP	Validity Criteria
RC Type	Max Continuity Constraints Violation
Range of RC Values	Max Change in Value of x_{MTN}
Number of RC Values	
Validity Criteria	
"Close Enough" Position Tolerance	

Table 3.1: Methodology Key Parameters. The items listed in this table are the key parameters associated with the methodology outlined in this section. "RC" stands for "Restricted Coordinate" and "MTP" stands for "Manifold Transition Point". x_{MTN} represents the x-value of the node that corresponded to the manifold transition point.

Chapter 4

Results for Selected Cases

4.1 Transfer 1: 2D Case 1

To verify the efficacy of using the methodology discussed in Chapter 3 to 3D orbits in the CR3BP, a test case in the PCR3BP was analyzed. This test case will be referred to as "Transfer 1" or "2D Case 1". The transfer was between two Lyapunov orbits about L_1 and L_2, from the L_1 Lyapunov orbit to the L_2 Lyapunov orbit.

4.1.1 Selected Parameters & Orbits

The two orbits that were selected for this transfer case are highlighted in Figure 4.1.

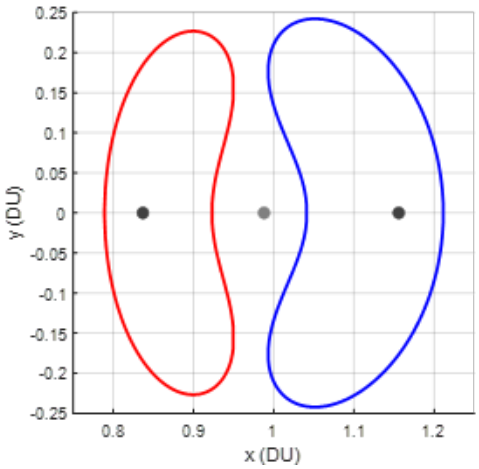

	Orbit 1	Orbit 2
Lagrange Point	L_1	L_2
Jacobi Constant	3.03851	3.03603
Initial Condition	$\begin{bmatrix} 0.789079999999996 \\ 0 \\ 0 \\ 0 \\ 0.414999104697071 \\ 0 \end{bmatrix}$	$\begin{bmatrix} 1.211192000000000 \\ 0 \\ 0 \\ 0 \\ -0.393402650654405 \\ 0 \end{bmatrix}$

Figure 4.1: Orbits Selected for Transfer 1. Left: The initial orbit (red) is a L_1 Lyapunov orbit and the final orbit (blue) is a L_2 Lyapunov orbit. The gray dot is the Moon and the black dots are L_1 (left black dot) and L_2 (right black dot). Right: Table providing characteristics of the two selected orbits.

Two initial conditions for the Lyapunov orbits were determined using the process outlined in Section 2.3.2. 100 L_1 and 100 L_2 Lyapunov orbits were generated. Of those orbits, the L_1 and L_2 Lyapunov orbits with Jacobi constant values closest to 3.03812 were selected as the initial and desired orbits, respectively. This value of C was selected because several other orbits of interest in the CR3BP had C values close to 3.03812.

A total of 100 values were selected as the possible x-values of the transition point between the manifolds. For this analysis, transfers with a x_{MT} near the Moon were of interest, so the values of x_{MT} were linearly spaced between L_1 and L_2. To generate the trajectories on each orbit's manifolds, 1,000 equally spaced points along each orbit were used. Using this number of points on each orbit resulted in 2,000 trajectories on each manifold, because there are two steps onto each manifold (from Equation 2.45 and Equation 2.46). A step size of 6.5×10^{-5} DU ($d = 25$ km) was used to determine the states on the manifold trajectories. As an orbit's unstable manifold trajectories move away from that orbit, the states on the unstable manifold of Orbit 1 were propagated forward in time from 0 TU to 10 TU. As an orbit's stable manifold trajectories move towards that orbit, the states on the stable manifold of Orbit 2 were propagated backward in time from 0 TU to -10 TU.

MATLAB's *ode113* and event functions were used to store the state vectors when each Poincaré section was crossed by the trajectories on the manifolds. Both positive and negative crossings of each Poincaré section with the same x-value were considered together. Canonical Units were used for all calculations and a tolerance of 10^{-13} was used when integrating the equations of motion. Once the manifold trajectories for all points on each orbit had been calculated, the analysis for each transfer began. For the first set value of x_{MT}, all of the manifold trajectories' state vectors at that x-value were identified from the output of the event functions. The magnitude of the difference in position (ΔP) and velocity (ΔV) were calculated between each of those state vectors that were on an Orbit 1 manifold trajectory and all of the state vectors that were on an Orbit 2 manifold trajectory. The pairs of state vectors with a ΔP less than 1.3×10^{-4} DU (50 km) were considered states on valid possible

transfers. Of those pairs of state vectors on valid possible transfers, the pair that had the lowest ΔV was then identified. The path resulting from the pair of manifold trajectories that corresponded to that identified pair of state vectors was considered to be the best transfer for that specific x_{MT} value. This process was repeated for the other 99 selected x_{MT} values.

4.1.2 Results for Manifold Transfers

This first transfer is between two 2D orbits with very similar Jacobi constant values. A preliminary analysis using conventional methods to identify a manifold transfer between these types of orbits will be conducted.

Preliminary Analysis

One of the Poincaré sections was set to be at $x = r_2$. Two Poincaré maps using the Jacobi constant values for Orbit 1 and Orbit 2 were constructed with positive Σ crossings that were generated from a 40x40 equally spaced grid of initial conditions over the ranges shown in Figure 4.2. The points on the orbits' manifold trajectories that crossed those Poincaré sections were isolated and plotted over top of the background Poincaré maps. While a Poincaré section is directional, the negative crossings of the manifold trajectories were also plotted on the same maps (although in a different color). The similar characteristics of the two maps was expected as the C values were similar. The results of this mapping are in Figure 4.2. The Σ crossings of Orbit 1's unstable manifold trajectories and Orbit 2's stable manifold trajectories were isolated, and are plotted together in Figure 4.3.

If the two orbits had the same values of the Jacobi constant, then any intersection in Figure 4.3 between the points corresponding to Orbit 1's unstable manifold and the points corresponding to Orbit 2's stable manifold would represent a transfer with $\Delta V = 0$ DU/TU. However, since the orbits have very similar values of the Jacobi constant (but not the same

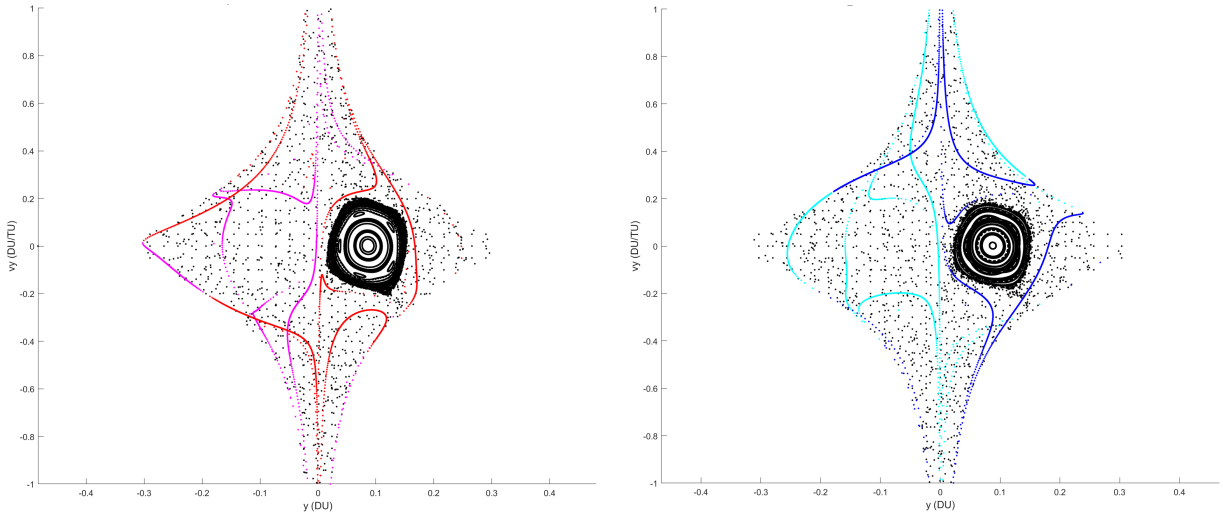

Figure 4.2: Poincaré Maps with Orbit Manifolds for Σ at $x = r_2$. Black dots represent the positive crossings resulting from a 40x40 equally spaced grid of initial conditions over the range shown by the axes limits in the plots. Red/blue dots are positive Σ crossings and magenta/cyan dots are negative Σ crossings of the manifolds. Left: Poincaré map with Orbit 1's C value and Σ crossings of Orbit 1's unstable manifold. Right: Poincaré map with Orbit 2's C value and Σ crossings of Orbit 2's stable manifold.

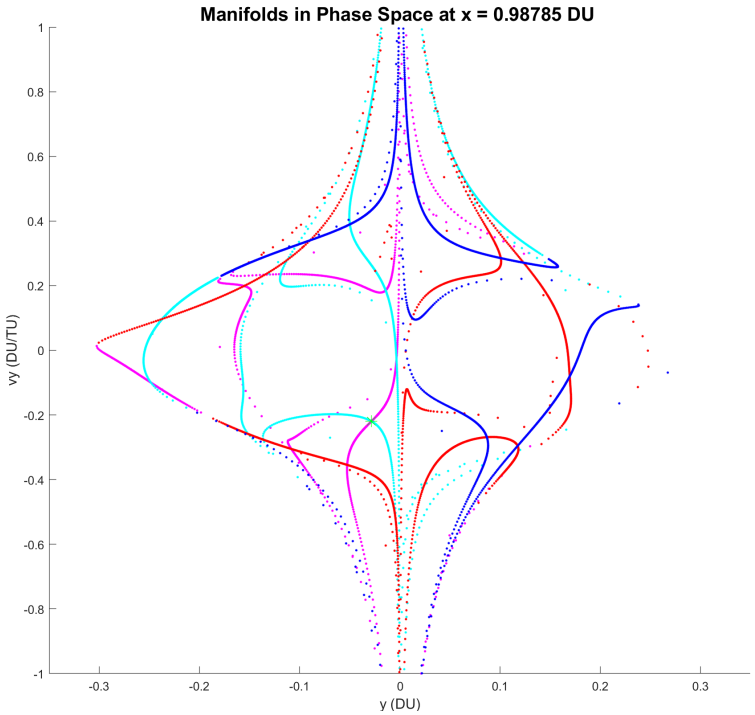

Figure 4.3: States of Orbit 1 Unstable & Orbit 2 Stable Manifolds at $x = r_2$. Σ is at $x = r_2$. Red/magenta dots are positive/negative Σ crossings of Orbit 1's unstable manifold. Blue/cyan dots are positive/negative Σ crossings of Orbit 2's stable manifold.

values of C), if the result from applying the methodology discussed in Section 3.1 yields a transfer with points very close to the intersections in Figure 4.3, that would be a good indication that the methodology discussed in Section 3.1 can be used.

Identified Transfers

The ΔVs and ΔPs at the manifold transition point for each of the best transfers identified by using the methodology discussed in Section 3.1 are provided in Figure 4.4.

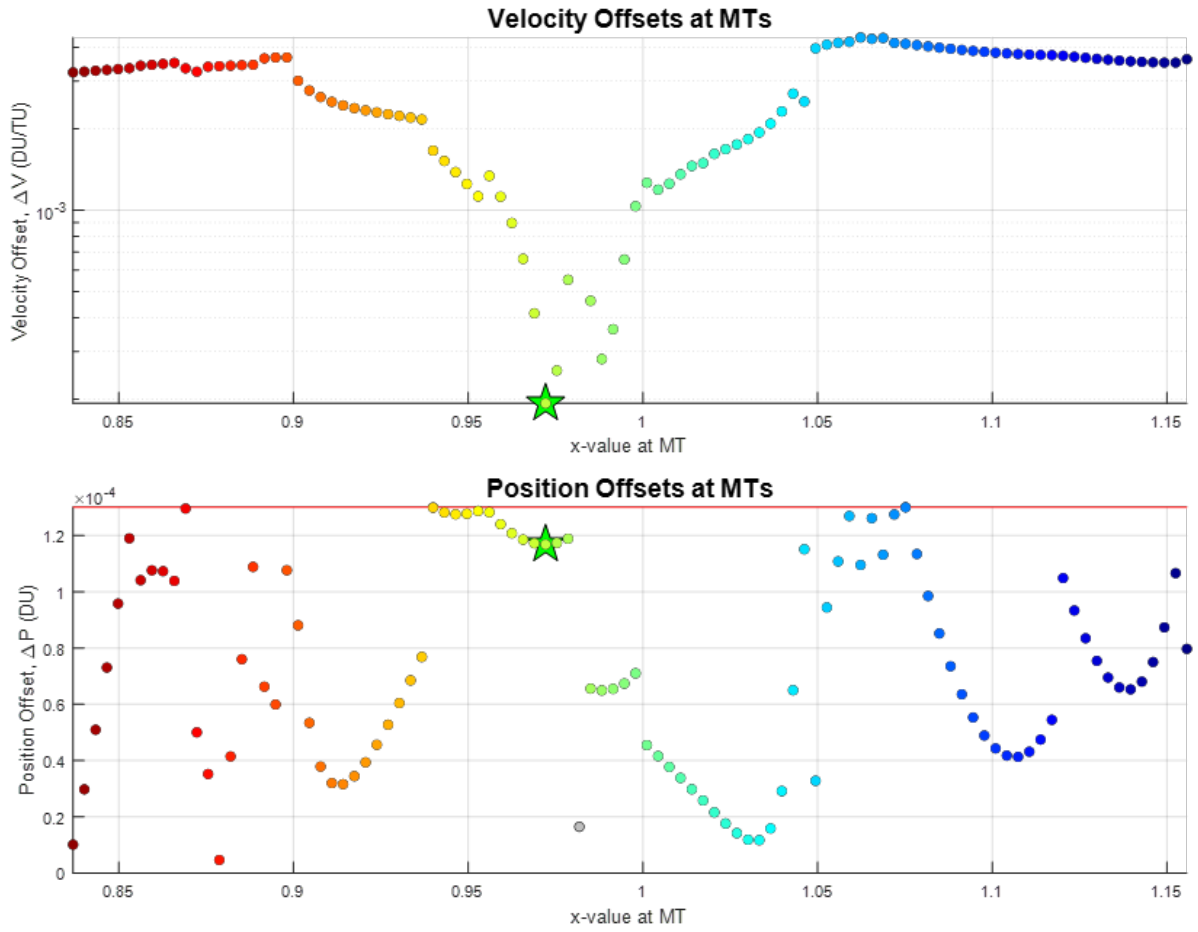

Figure 4.4: Position and Velocity Offsets at the Manifold Transition Point of the Best Manifold Transfers for Transfer 1. The velocity offsets are shown in the top plot and the position offsets are shown in the bottom plot. The maximum allowable position offset is indicated by the red line. Gray dots indicate the transfer crashed into the Moon. The light green star indicates the best manifold transfer overall. The color scale indicates the value of x_{MT} for each transfer, with maroon being at L_1 and navy being at L_2, and is the same as the color scale in Figure 4.5.

The ΔVs of the best transfers were lowest for x_{MT} values between 0.95 and 1 DU. A transfer that met the position continuity requirement was identified for all 100 of the set values of x_{MT}. One of those 100 transfers had a path that crashed into the Moon, so that transfer was ignored when determining the best transfer overall. An image of the best manifold transfers is provided on the left side of Figure 4.5. An image of the best manifold transfer overall is on the right side of Figure 4.5. At the x_{MT} of the best manifold transfer overall, $x_{MT} = 0.9721$ DU, $\Delta P = 1.1683 \times 10^{-4}$ DU, and a ΔV of 1.931×10^{-4} DU/TU was required.

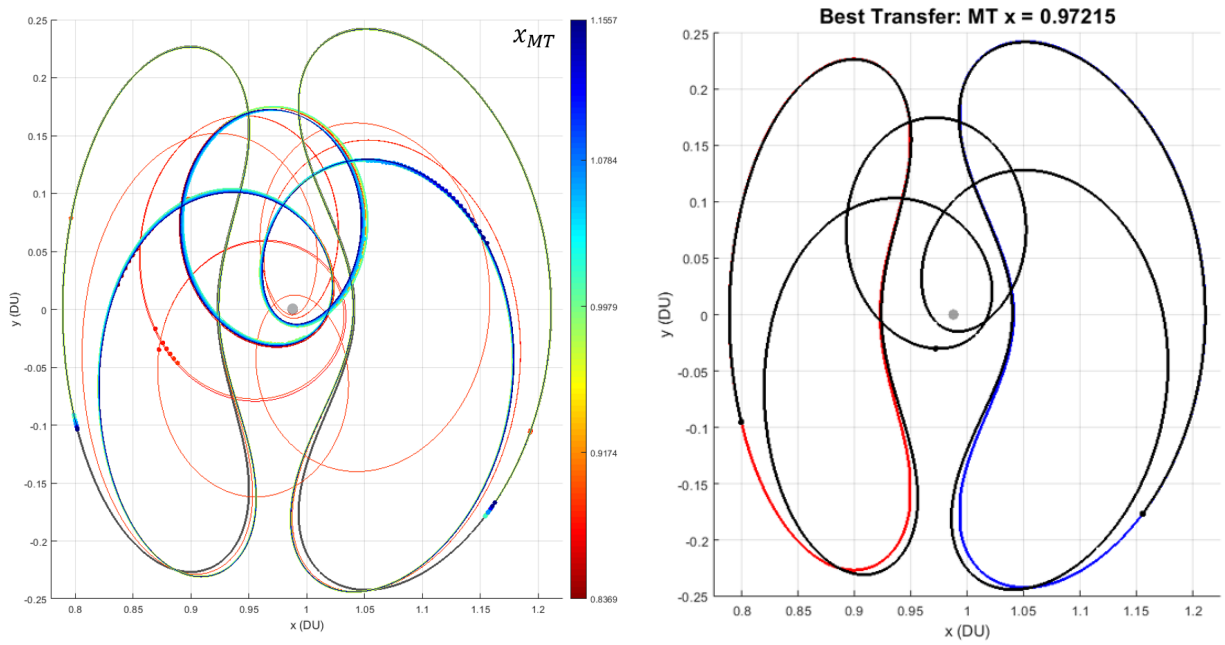

Figure 4.5: Best Identified Manifold Transfers for Transfer 1. Left: Best manifold transfers at each specified value of x_{MT}. The color scale indicates the value of x_{MT} for each manifold transfer with maroon being at L_1 and navy being at L_2 (see Figure 4.4). Right: Best manifold transfer overall for Transfer 1. The black line represents the best transfer identified amongst all the best manifold transfers for Transfer 1, which are shown on the left.

Applying the methodology discussed in Section 3.1 resulted in a transfer with states at the manifold transition point that were close to one of the intersections in Figure 4.3. This transfer is shown on the right side of Figure 4.5. This result is a good indication that this methodology can be used for transfers between more complex orbits in the CR3BP.

4.1.3 Results from Optimization

The total ΔV and the magnitude of the maximum constraint violation for the Correction Set 1 transfers and the best manifold transfers for Transfer 1 are provided in Figure 4.6.

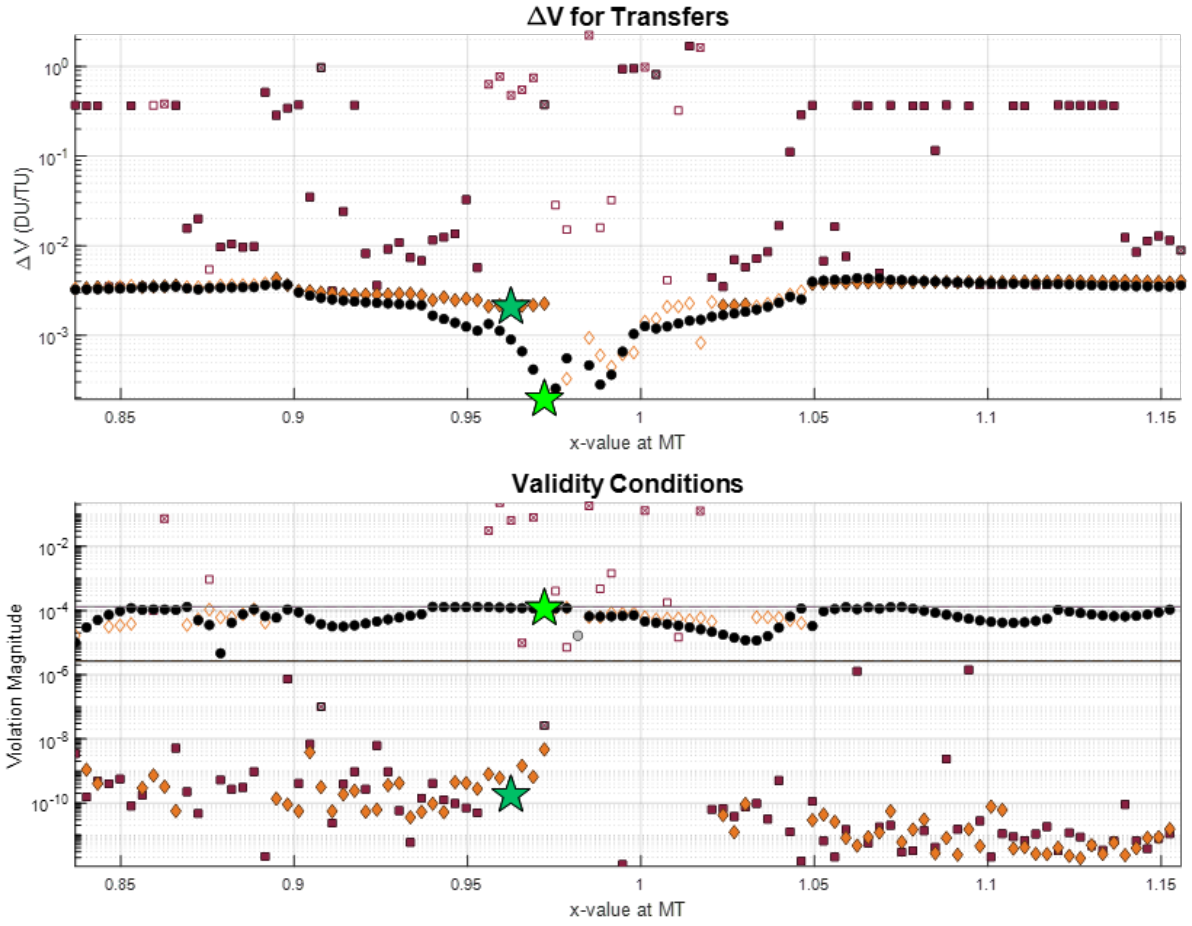

Figure 4.6: Total ΔV and Constraint Violation of the Correction Set 1 Transfers for Transfer 1. The total ΔVs are shown in the top plot and the maximum constraint violations are shown in the bottom plot. The maximum allowable constraint violation is indicated by the black line, and the maximum allowable position offset for the manifold transfers is shown by the gray line. Black dots indicate the best manifold transfers (same data as shown in Figure 4.4). Gray dots indicate the manifold transfer crashed into the Moon. Solid shapes indicate a valid corrected transfer. Maroon and orange indicate a corrected transfer of Type 1 and Type 2, respectively. Hollow shapes indicate the corrected transfer violated the max allowable constraint limit. Hollow shapes with "+"s or "x"s in the middle indicate the corrected transfer crashed into the Moon. The light green star indicates the best manifold transfer overall. The dark green star indicates the best corrected transfer from Set 1.

As can be seen in Figure 4.6, manifold transfers with values of x_{MT} between 0.9 and 0.95 DU

or between 1.05 and 1.15 DU resulted in the highest rate of convergence, while those with values of x_{MT} between 0.975 and 1.02 DU resulted in the worst convergence rate for Set 1. For the most part, Set 1 Type 1 and Set 1 Type 2 appeared to find different corrected transfers based on the same manifold transfer (the ΔVs for the Type 1 corrected transfers are not similar to the ΔVs for the Type 2 corrected transfers). The best corrected transfer from Set 1 had significantly better continuity characteristics, but required significantly more ΔV, compared to the best manifold transfer overall. The value of x_{MT} corresponding to the best corrected transfer from Set 1 did shift compared to the value of x_{MT} corresponding to the best manifold transfer overall. The spatial representations of each of the corrected transfers from Set 1, along with the best corrected transfer from Set 1, are provided in Figure 4.7. As can be seen on the left side of Figure 4.7, the spatial shapes of the some of the corrected transfers were noticeably different than the manifold transfers on which they were based.

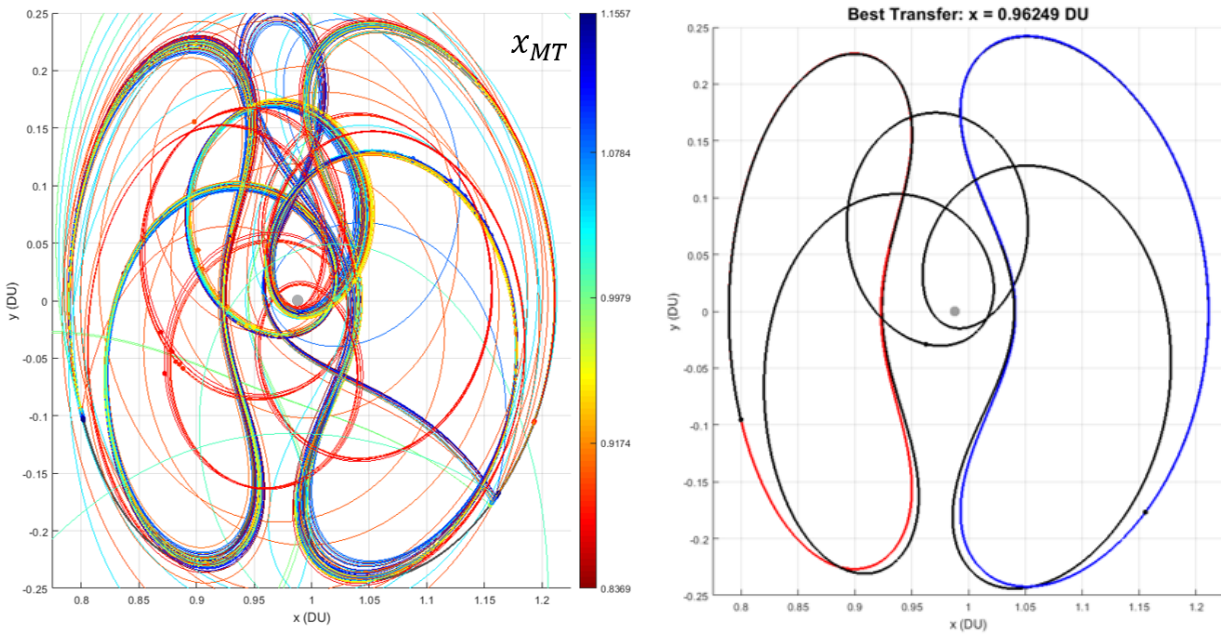

Figure 4.7: Transfers from Correction Set 1 for Transfer 1. Left: Corrected transfers from Set 1 at each specified value of x_{MT}. The color scale indicates the x_{MT} value of the manifold transfer used in the optimization scheme to generate each corrected transfer with maroon being at L_1 and navy being at L_2 (see Figure 4.4). Right: Best corrected transfer from Set 1 for Transfer 1. The black line represents the best transfer identified amongst all the possible corrected transfers from Set 1 for Transfer 1, which are shown on the left.

The total ΔV and the magnitude of the maximum constraint violation for the Correction Set 2 transfers and the best manifold transfers for Transfer 1 are provided in Figure 4.8.

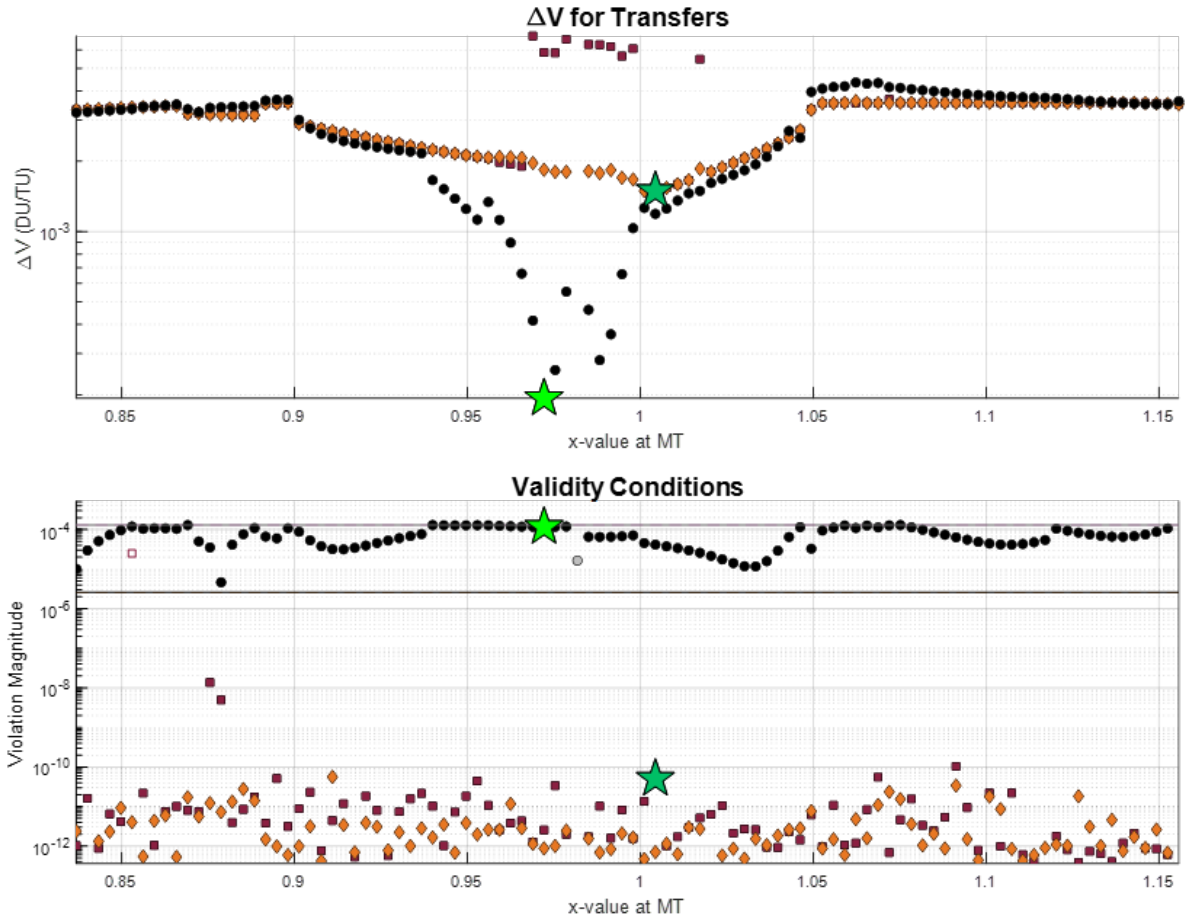

Figure 4.8: Total ΔV and Constraint Violation of the Correction Set 2 Transfers for Transfer 1. The total ΔVs are shown in the top plot and the maximum constraint violations are shown in the bottom plot. The maximum allowable constraint violation is indicated by the black line, and the maximum allowable position offset for the manifold transfers is shown by the gray line. Black dots indicate the best manifold transfers (same data as shown in Figure 4.4). Gray dots indicate the manifold transfer crashed into the Moon. Solid shapes indicate a valid corrected transfer. Maroon and orange indicate a corrected transfer of Type 1 and Type 2, respectively. Hollow shapes indicate the corrected transfer violated the max allowable constraint limit. Hollow shapes with "+"s or "x"s in the middle indicate the corrected transfer crashed into the Moon. The light green star indicates the best manifold transfer overall. The dark green star indicates the best corrected transfer from Set 2.

As can be seen in Figure 4.8, all manifold transfers converged to a valid Set 2 corrected transfer, except for one Set 2 Type 1 transfer. Except for a region with x_{MT} between 0.97 and 1 DU (and one more outside that range), Set 2 Type 1 and Set 2 Type 2, when based on

the same manifold transfer, appeared to find the same corrected transfers (the ΔVs for the Type 1 and Type 2 corrected transfers are very similar). In the region where the corrected transfers of Type 1 and Type 2 did not have similar ΔVs, the Type 2 corrected transfers had lower ΔVs. The best corrected transfer from Set 2 had a lower ΔV required than the best corrected transfer from Set 1, but still required more ΔV compared to the best manifold transfer overall. The value of x_{MT} corresponding to the best corrected transfer from Set 2 is noticeably different than the values of x_{MT} corresponding to the best corrected transfer from Set 1 and the best manifold transfer overall. The spatial representations of the Set 2 corrected transfers, along with the best corrected transfer from Set 2, are provided in Figure 4.9. As can be seen on the left side of Figure 4.9, the spatial shapes of the Set 2 corrected transfers were more similar to the manifold transfers on which they were based than was the case for the Set 1 corrected transfers.

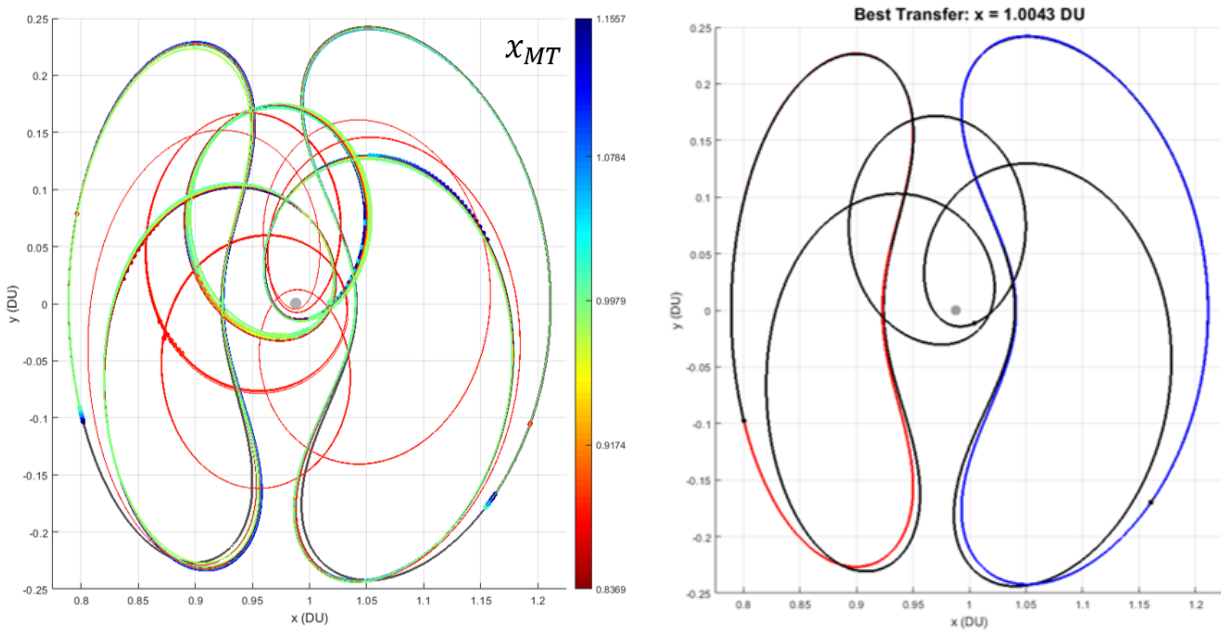

Figure 4.9: Transfers from Correction Set 2 for Transfer 1. Left: Corrected transfers from Set 2 at each specified value of x_{MT}. The color scale indicates the x_{MT} value of the manifold transfer used in the optimization scheme to generate each corrected transfer with maroon being at L_1 and navy being at L_2 (see Figure 4.4). Right: Best corrected transfer from Set 2 for Transfer 1. The black line represents the best transfer identified amongst all the possible corrected transfers from Set 2 for Transfer 1, which are shown on the left.

The total ΔV and the magnitude of the maximum constraint violation for the Correction Set 3 transfers and the best manifold transfers for Transfer 1 are provided in Figure 4.10.

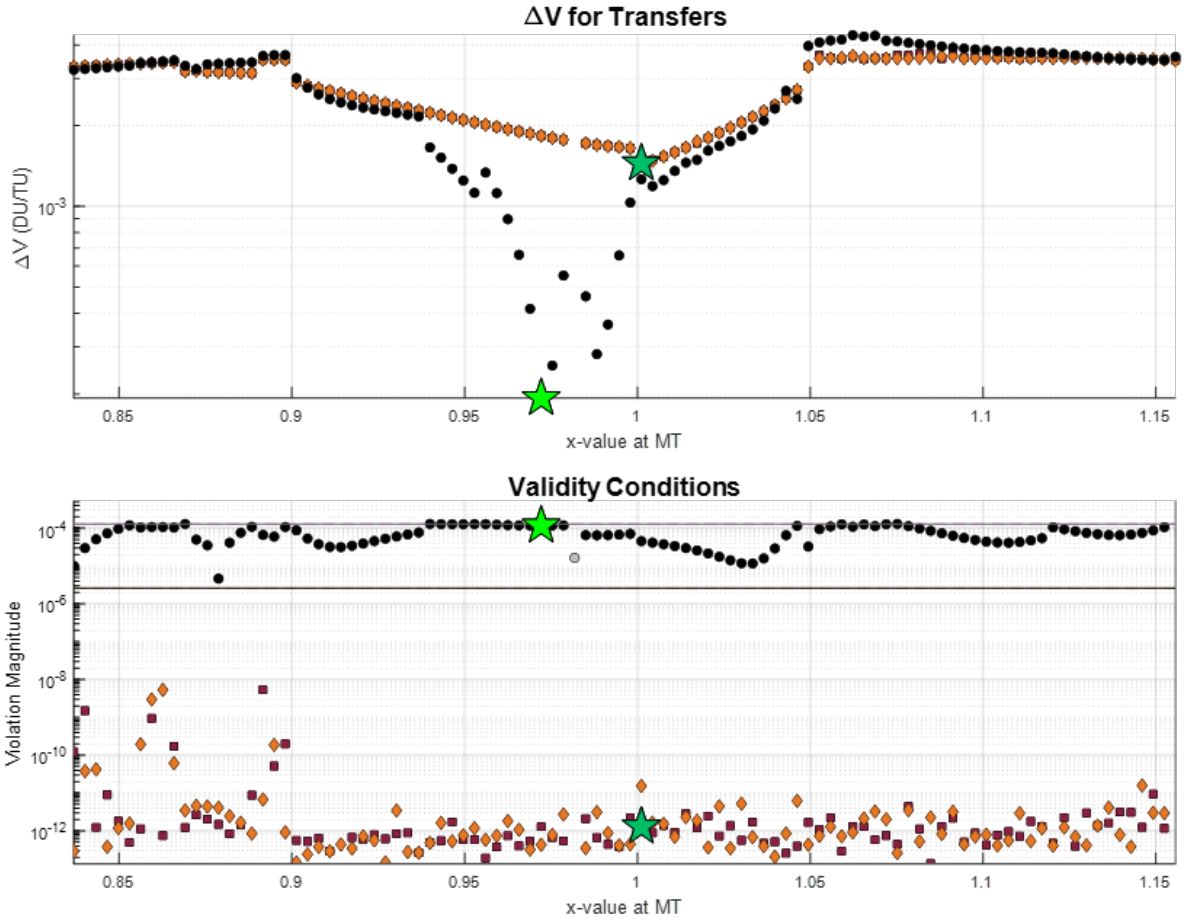

Figure 4.10: Total ΔV and Constraint Violation of the Correction Set 3 Transfers for Transfer 1. The total ΔVs are shown in the top plot and the maximum constraint violations are shown in the bottom plot. The maximum allowable constraint violation is indicated by the black line, and the maximum allowable position offset for the manifold transfers is shown by the gray line. Black dots indicate the best manifold transfers (same data as shown in Figure 4.4). Gray dots indicate the manifold transfer crashed into the Moon. Solid shapes indicate a valid corrected transfer. Maroon and orange indicate a corrected transfer of Type 1 and Type 2, respectively. Hollow shapes indicate the corrected transfer violated the max allowable constraint limit. Hollow shapes with "+"s or "x"s in the middle indicate the corrected transfer crashed into the Moon. The light green star indicates the best manifold transfer overall. The dark green star indicates the best corrected transfer from Set 3.

As can be seen in Figure 4.10, all manifold transfers converged to a valid Set 3 corrected transfer for both Set 3 Type 1 and Set 3 Type 2. For all values of x_{MT}, Set 3 Type 1 and Set 3 Type 2, when based on the same manifold transfer, appeared to find the same corrected

transfers. The best corrected transfers from Set 2 and Set 3 appear to be similar. The best corrected transfer from Set 3 had a very similar required ΔV compared to the best corrected transfer from Set 2. The value of x_{MT} corresponding to the best corrected transfer from Set 3 was also very similar to the value of x_{MT} corresponding to the best corrected transfer from Set 2. Also, the relationship between the ΔV required and x_{MT} exhibited by the Set 3 (and most of the Set 2) corrected transfers, was very similar to the relationship exhibited by the best manifold transfers. The spatial representations of the Set 3 corrected transfers, along with the best corrected transfer from Set 3, are provided in Figure 4.11. As was the case for the Set 2 corrected transfers, the spatial shapes of the Set 3 corrected transfers were similar to the manifold transfers on which they were based, as can be seen on the left side of Figure 4.11.

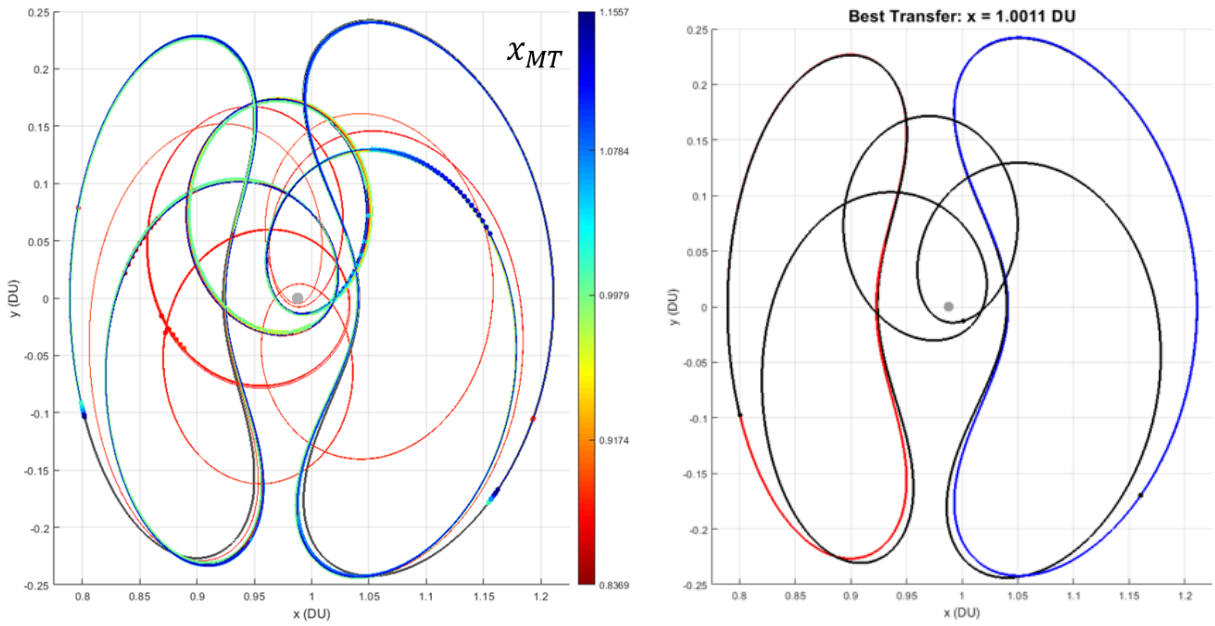

Figure 4.11: Transfers from Correction Set 3 for Transfer 1. Left: Corrected transfers from Set 3 at each specified value of x_{MT}. The color scale indicates the x_{MT} value of the manifold transfer used in the optimization scheme to generate each corrected transfer with maroon being at L_1 and navy being at L_2 (see Figure 4.4). Right: Best corrected transfer from Set 3 for Transfer 1. The black line represents the best transfer identified amongst all the possible corrected transfers from Set 3 for Transfer 1, which are shown on the left.

4.1.4 Discussion

The success rate of the methodology used to identify valid manifold transfers, as well as data on the convergence of the correction models when applied to the best manifold transfers for Transfer 1, are shown in Table 4.1.

Convergence Transfer 1 2D Case 1	Valid Transfers		Met Constraint Violation Limit		No Moon Crash	
	Number	*%*	*Number*	*%*	*Number*	*%*
Original Transfers						
Manifold Transfers	**99**	**99**	100	100	99	99
Corrected Transfers						
Set 1 Type 1	**78**	**78.8**	82	82.8	86	86.9
Set 1 Type 2	**68**	**68.7**	68	68.7	99	100
Set 2 Type 1	**98**	**99.0**	98	99.0	99	100
Set 2 Type 2	**99**	**100**	99	100	99	100
Set 3 Type 1	**99**	**100**	99	100	99	100
Set 3 Type 2	**99**	**100**	99	100	99	100

Table 4.1: Convergence Results for Transfer 1. One manifold transfer for each of the 100 x_{MT} values was desired, so the manifold transfer convergence percentages are out of 100. An optimization scheme using each correction model was applied to each valid manifold transfer that was identified, so the correction model convergence percentages are out of the number of valid manifold transfers (99 for Transfer 1). Green or red values indicate the best or worst validity rate for the criteria in that column, respectively.

As the two orbits in this transfer case were 2D and had very similar Jacobi constant values, the high rate of success in identifying valid manifold transfers is not surprising. The fact that a correction model of Type 2 had the worst convergence rate (Set 1 Type 2) was surprising; typically initial guesses from models of Type 1 have lower initial costs, but much larger constraint violations than initial guesses from models of Type 2. However, both Type 1 and Type 2 correction models with more than three node points (Set 2 and Set 3), had high convergence rates.

Looking at Figure 4.5, while 99 valid manifold transfers were identified by using the methodology, it appears that many of those transfers follow similar paths. By grouping those 99 transfers

together based on their path, a smaller number of truly distinct transfer paths can be identified. In the spatial representations of the best manifold transfers for this transfer case, the manifold transfers for x_{MT} values that were in between approximately 0.87 and 0.89 DU appear to follow a single distinct path. For this discussion, when the color of a transfer is mentioned, it is referring to the x_{MT} value of that transfer. Note the relationship between the colors of the transfers and the values of x_{MT} for the transfers is depicted in Figure 4.4 and Figure 4.5. For example, the phrase "maroon and red transfers" will be used to refer to the transfers with x_{MT} values that are approximately between 0.837 and 0.89 DU. With closer inspection of Figure 4.5, it appears that two distinct transfer paths were identified. The first distinct transfer path is the path followed by the red transfers that are grouped together. The second distinct transfer path is the path followed by all the other transfers that are grouped together.

In contrast to the manifold transfers, for the transfers in Correction Set 1, there was a wider variety of different paths identified. As can be seen in Figure 4.7, while the red transfers appear to have similar paths to one another, and the blue transfers also appear to have similar paths to one another, there is clearly a wider variety of less similar paths, even though all of the paths shown in Figure 4.7 were based on the transfers that followed the two transfer paths from Figure 4.5. Considering the transfers in Correction Set 2 shown in Figure 4.9, the corrected transfers in this set appear to follow the two distinct transfer paths that were originally identified in the manifold transfers in Figure 4.5. This similarity is also present in the corrected transfers in Correction Set 3 which are shown in Figure 4.11. One significant finding is that for this transfer case, only two distinct transfer paths were identified even though 100 different manifold transfers were considered. For both correction models with more than three nodes, still only two distinct transfer paths were identified.

Characteristics of the best manifold transfer overall and the best corrected transfers found for each correction model for Transfer 1 are provided in Table 4.2.

Best Transfer Overall Transfer 1 2D Case 1	x_{MT} *DU*	ΔV *DU/TU*	TOF *TU*	Constraint Violation –	Correction Type –
Original Transfers					
Manifold Transfers	0.9722	**1.9307 $\times 10^{-4}$**	11.844	1.1683 $\times 10^{-4}$	N/A
Corrected Transfers					
Set 1	0.9625	**2.0774 $\times 10^{-3}$**	11.843	1.7635 $\times 10^{-10}$	2
Set 2	1.0044	**1.4932 $\times 10^{-3}$**	11.804	5.0636 $\times 10^{-11}$	1
Set 3	1.0011	**1.4480 $\times 10^{-3}$**	11.803	1.3017 $\times 10^{-12}$	2

Table 4.2: Characteristics of the Best Transfers for Transfer 1. Characteristics of the best transfer identified in the original set of manifold transfers, as well as for each corrected set of transfers. The constraint violation column has the maximum magnitude of the violation of any constraint used in the optimization process, and the units could be in DU or DU/TU depending on what specific type of constraint corresponded to the violation with the maximum magnitude. A green value indicates the best corrected transfer overall.

Looking at the data in Table 4.2, the best corrected transfers from Set 2 and Set 3 appear to be very similar. The fact that both these sets found similar transfers is a good indication that a corrected transfer with a sufficiently low ΔV was identified.

A low-cost transfer between two planar Lyapunov orbits, specifically from a L_1 Lyapunov orbit to a L_2 Lyapunov orbit, was identified. Techniques related to dynamical systems theory, such as those related to identifying periodic orbits, manifolds, and Poincaré maps, and techniques related to differential corrections and optimization were used to identify that transfer. As indicated by the results for this transfer case, the methodology used in this analysis is effective in identifying low-cost transfers between 2D orbits in the PCR3BP. The methodology is useful because it can be applied to cases where the initial and final orbits do not have the same Jacobi constant value. Even though this methodology could be considered inefficient compared to other more basic approaches when used to identify the best transfer between 2D Lyapunov orbits in the PCR3BP, this test case has validated the efficacy of this methodology. This methodology could be useful for identifying transfers between 3D orbits with different Jacobi constant values in the CR3BP, where more basic techniques that can be used in the PCR3BP are not as effective.

4.2 Transfer 2: 3D Case 1

With the results of Transfer 1 seeming to provide sufficient evidence for the efficacy of this methodology, a 3D transfer case was considered. This transfer case will be referred to as "Transfer 2" or "3D Case 1". The transfer will between a L_1 halo orbit and a L_2 halo orbit.

4.2.1 Selected Parameters & Orbits

A differential correction scheme was applied to halo orbits from Grebow [1] (the initial conditions for the orbits were in Table 3.4 and Table 3.5 in that document) to obtain valid initial conditions for the halo orbits that were used in this transfer case. The L_1 and L_2 halo orbits with Jacobi constant values closest to 3.03812 were selected as the initial and desired orbits, respectively. The two orbits that were selected for the analysis in this transfer case are highlighted in Figure 4.12.

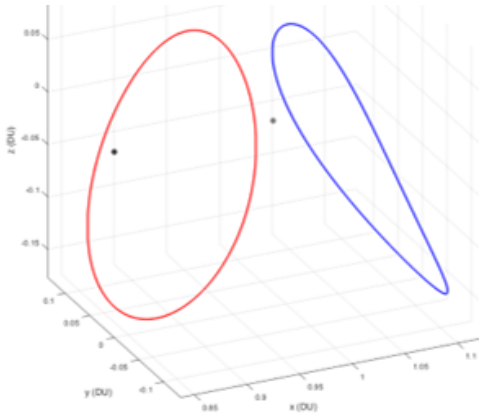

	Orbit 1	Orbit 2
Lagrange Point	L_1	L_2
Jacobi Constant	3.04269	3.04238
Initial Condition	$\begin{bmatrix} 0.836812615000000 \\ 0 \\ -0.147469552000000 \\ 0 \\ 0.256004070000000 \\ 0 \end{bmatrix}$	$\begin{bmatrix} 1.12973443200000 \\ 0 \\ -0.176981034000000 \\ 0 \\ -0.225485580000000 \\ 0 \end{bmatrix}$

Figure 4.12: Orbits Selected for Transfer 2. Left: The initial orbit (red) is an L_1 halo orbit and the final orbit (blue) is an L_2 halo orbit. The gray dot is the Moon and the black dot is L_1. Right: Table providing characteristics of the two selected orbits.

The same parameters used to determine the best manifold transfer for Transfer 1 were used for Transfer 2. 100 linearly spaced values from L_1 to L_2 were selected as the possible x-values of the manifold transition point. 1,000 equally spaced points along each orbit and a step size of 6.5×10^{-5} DU ($d = 25$ km) were used to generate the manifold trajectories. The states on

the manifolds were propagated from 0 TU to ± 10 TU for the unstable and stable manifold trajectories, respectively. MATLAB's *ode113* and event functions were used to store the state vectors when each Poincaré section was crossed by the trajectories. Positive and negative crossings of each Poincaré section with the same x-value were considered. A tolerance of 10^{-13} was used during integration. Pairs of state vectors at the manifold transition point with $\Delta P \leq 1.3 \times 10^{-4}$ DU (50 km) were considered states on valid possible transfers.

4.2.2 Results for Manifold Transfers

The ΔVs and ΔPs at the manifold transition point for the manifold transfers are in Figure 4.13.

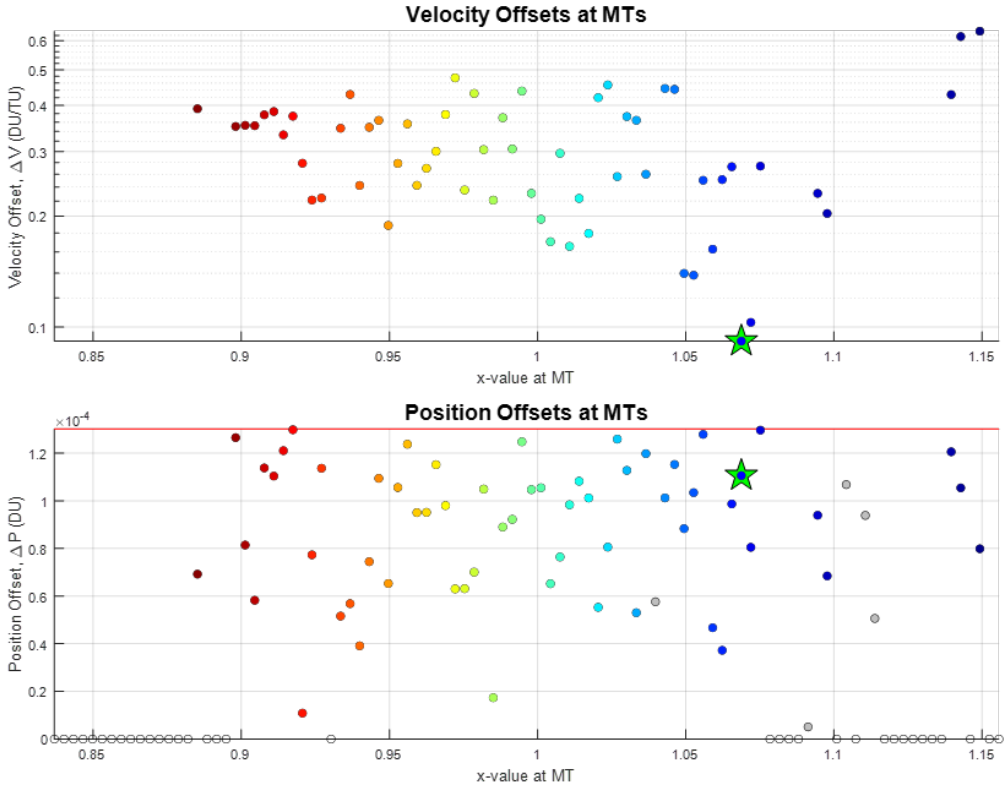

Figure 4.13: Position and Velocity Offsets at the Manifold Transfer Point of the Best Manifold Transfers for Transfer 2. The ΔVs are shown in the top plot and the ΔPs are shown in the bottom plot. The maximum allowable ΔP is indicated by the red line. Gray dots indicate the transfer crashed into the Moon. The light green star indicates the best manifold transfer overall. The color scale indicates the value of x_{MT} for each transfer, with maroon being at L_1 and navy being at L_2, and is the same as the color scale in Figure 4.14.

The relationship between the required ΔV and the value of x_{MT} for the best manifold transfers is not as clear as it was for Transfer 1. However, there appears to be three groups of manifold transfers with lower ΔVs than the other manifold transfers. Among these three groups, the group of transfers with an x_{MT} between 1.05 and 1.07 DU appears to have the lowest ΔV. A manifold transfer that met the position continuity requirement at the manifold transition point was identified for 65 of the 100 set values of x_{MT}. Five of those 65 transfers had a path that crashed into the Moon, and were ignored when determining the best manifold transfer overall. An image of the best manifold transfers is provided on the left side of Figure 4.14. An image of the best manifold transfer overall is on the right side of Figure 4.14. At the x_{MT} of the best manifold transfer overall, $x_{MT} = 1.06875$ DU, $\Delta P = 1.1056 \times 10^{-4}$ DU, and a ΔV of 9.1567×10^{-2} DU/TU was required.

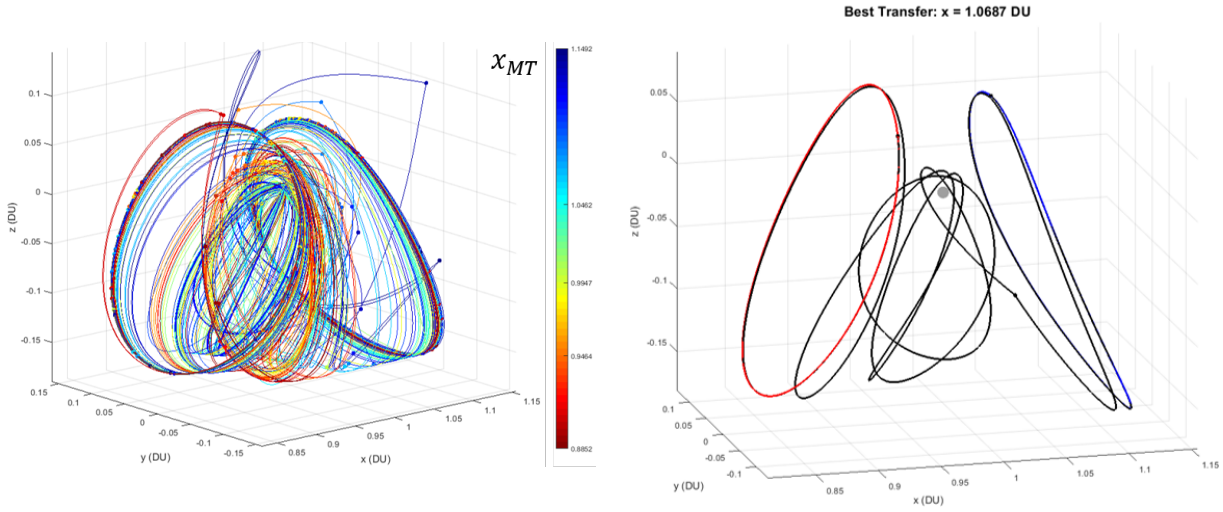

Figure 4.14: Best Identified Manifold Transfers for Transfer 2. Left: Best manifold transfers at each specified value of x_{MT}. The color scale indicates the value of x_{MT} for each manifold transfer with maroon being at L_1 and navy being at L_2 (see Figure 4.13). Right: Best manifold transfer overall for Transfer 2. The black line represents the best transfer identified amongst all the possible best manifold transfers for Transfer 2, which are shown on the left.

Images of the orthographic projections of the best manifold transfers for Transfer 2 are provided in Figure 4.15. Please note that the transfers shown in Figure 4.15 are the same as those shown on the left side of Figure 4.14.

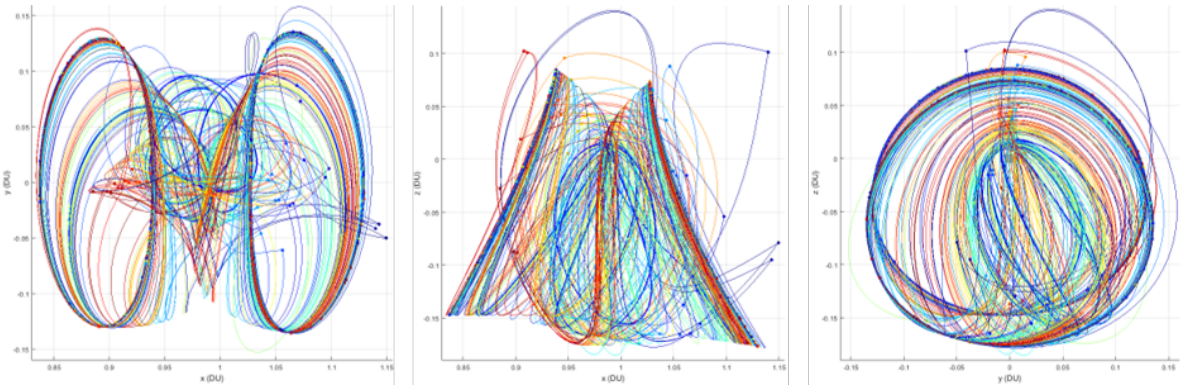

Figure 4.15: Best Identified Manifold Transfers for Transfer 2 (Orthographic Projections). Best manifold transfers at each specified value of x_{MT}. The color scale indicates the value of x_{MT} for each manifold transfer with maroon being at L_1 and navy being at L_2 (see Figure 4.13). Left: x-y view (viewpoint looking down at the primaries' plane of motion). Middle: x-z view (viewpoint looking at the Moon with the Earth to the left). Right: y-z view (viewpoint from the other side of the Moon, relative to the Earth, and looking at the Moon).

4.2.3 Results from Optimization

The total ΔV and the magnitude of the maximum constraint violation for both the Correction Set 1 transfers and the best manifold transfers for Transfer 2 are provided in Figure 4.16. The convergence of the manifold transfers did not appear to be heavily dependent on the value of x_{MT} for Set 1. While there appears to be three Type 1 corrected transfers that have significantly lower ΔVs than the other corrected transfers in this set, those transfers are invalid as they exceeded the maximum allowable constraint violation limit. For the most part, Set 1 Type 1 and Set 1 Type 2 appeared to find different corrected transfers based on the same manifold transfer, with the ΔVs for the Type 1 corrected transfers often being greater compared to the ΔVs for the Type 2 corrected transfers. The best corrected transfer from Set 1 had significantly better continuity characteristics, and had only a slightly higher required ΔV compared to the best manifold transfer overall. The value of x_{MT} corresponding to the best corrected transfer from Set 1 was significantly closer to the Moon (shifted towards the origin in the $-x$ direction) compared to the value of x_{MT} corresponding to the best manifold transfer overall.

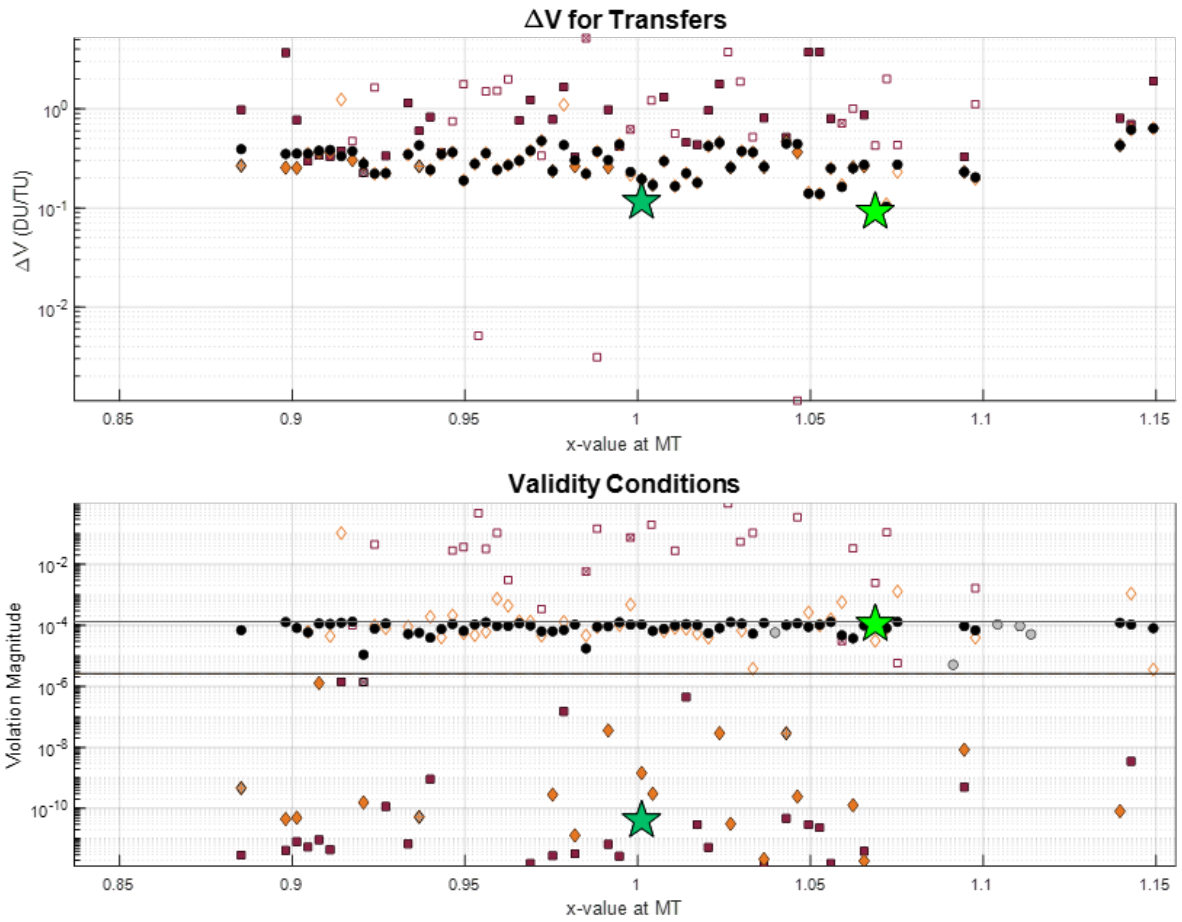

Figure 4.16: Total ΔV and Constraint Violation of the Correction Set 1 Transfers for Transfer 2. The total ΔVs are shown in the top plot and the maximum constraint violations are shown in the bottom plot. The maximum allowable constraint violation is indicated by the black line, and the maximum allowable position offset for the manifold transfers is shown by the gray line. Black dots indicate the best manifold transfers (same data as shown in Figure 4.13). Gray dots indicate the manifold transfer crashed into the Moon. Solid shapes indicate a valid corrected transfer. Maroon and orange indicate a corrected transfer of Type 1 and Type 2, respectively. Hollow shapes indicate the corrected transfer violated the maximum allowable constraint limit. Hollow shapes with "+"s or "x"s in the middle indicate the corrected transfer crashed into the Moon. The light green star indicates the best manifold transfer overall. The dark green star indicates the best corrected transfer from Set 1.

The spatial representations of each of the corrected transfers from Set 1, along with the best corrected transfer from Set 1, are provided in Figure 4.17. As can be seen on the left side of Figure 4.17, the spatial shapes of the some of the corrected transfers were noticeably different compared to the manifold transfers on which they were based.

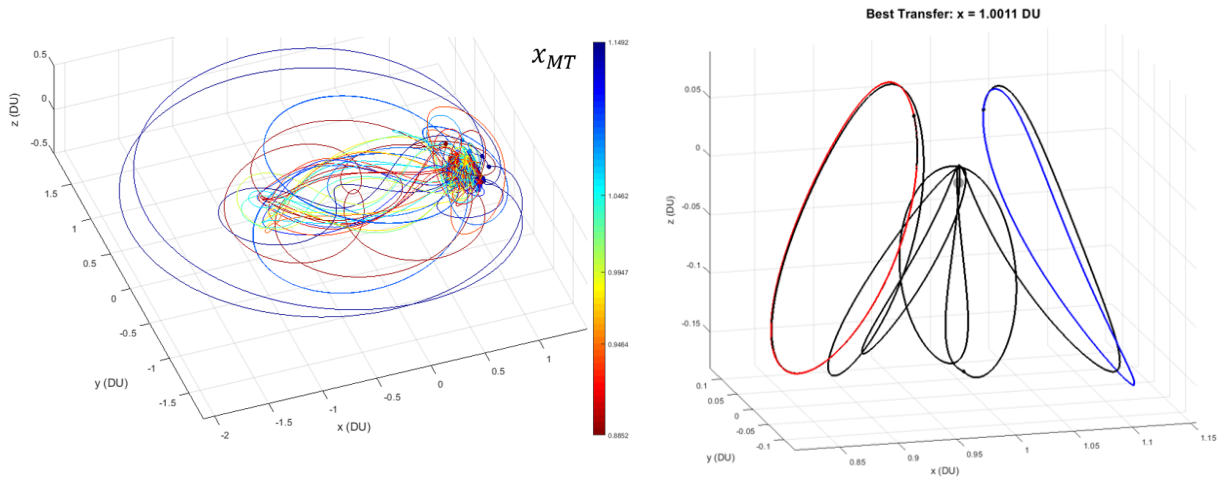

Figure 4.17: Transfers from Correction Set 1 for Transfer 2. Left: Corrected transfers from Set 1 at each specified value of x_{MT}. The color scale indicates the x_{MT} value of the manifold transfer used in the optimization scheme to generate each corrected transfer with maroon being at L_1 and navy being at L_2 (see Figure 4.13). Right: Best corrected transfer from Set 1 for Transfer 2. The black line represents the best transfer identified amongst all the possible corrected transfers from Set 1 for Transfer 2, which are shown on the left.

The orthographic projections of the Set 1 corrected transfers for this transfer case are provided in Figure 4.18.

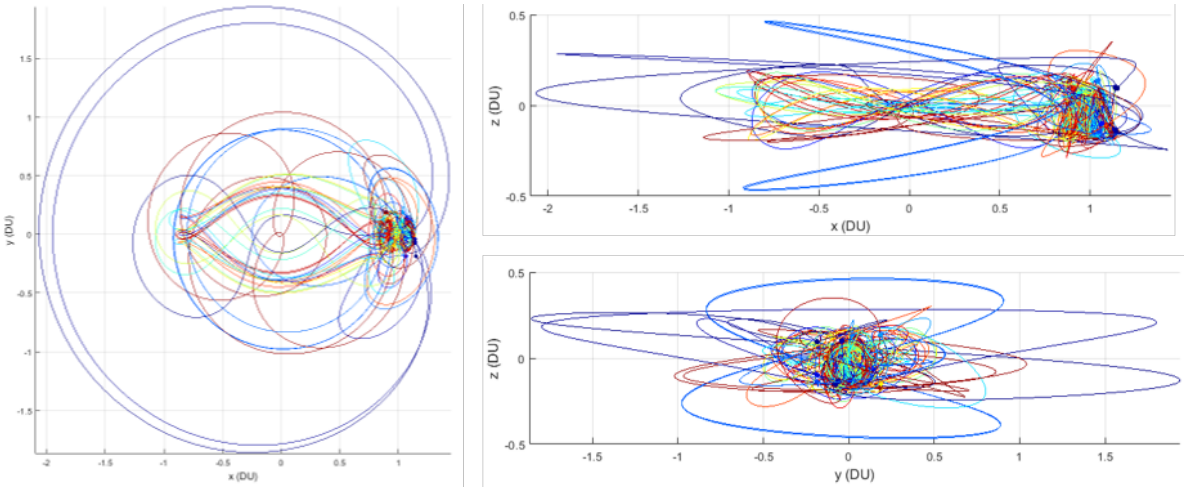

Figure 4.18: Transfers from Correction Set 1 for Transfer 2 (Orthographic Projections). Corrected transfers from Set 1 at each specified value of x_{MT}. The color scale indicates the x_{MT} value of the manifold transfer used in the optimization scheme to generate each corrected transfer with maroon being at L_1 and navy being at L_2 (see Figure 4.13). Left: x-y view (viewpoint looking down at the primaries' plane of motion). Top Right: x-z view (viewpoint looking at the Moon with the Earth to the left). Bottom Right: y-z view (viewpoint from the other side of the Moon, relative to the Earth, and looking at the Moon).

The total ΔV and the magnitude of the maximum constraint violation for the Correction Set 2 transfers and the best manifold transfers for Transfer 2 are provided in Figure 4.19.

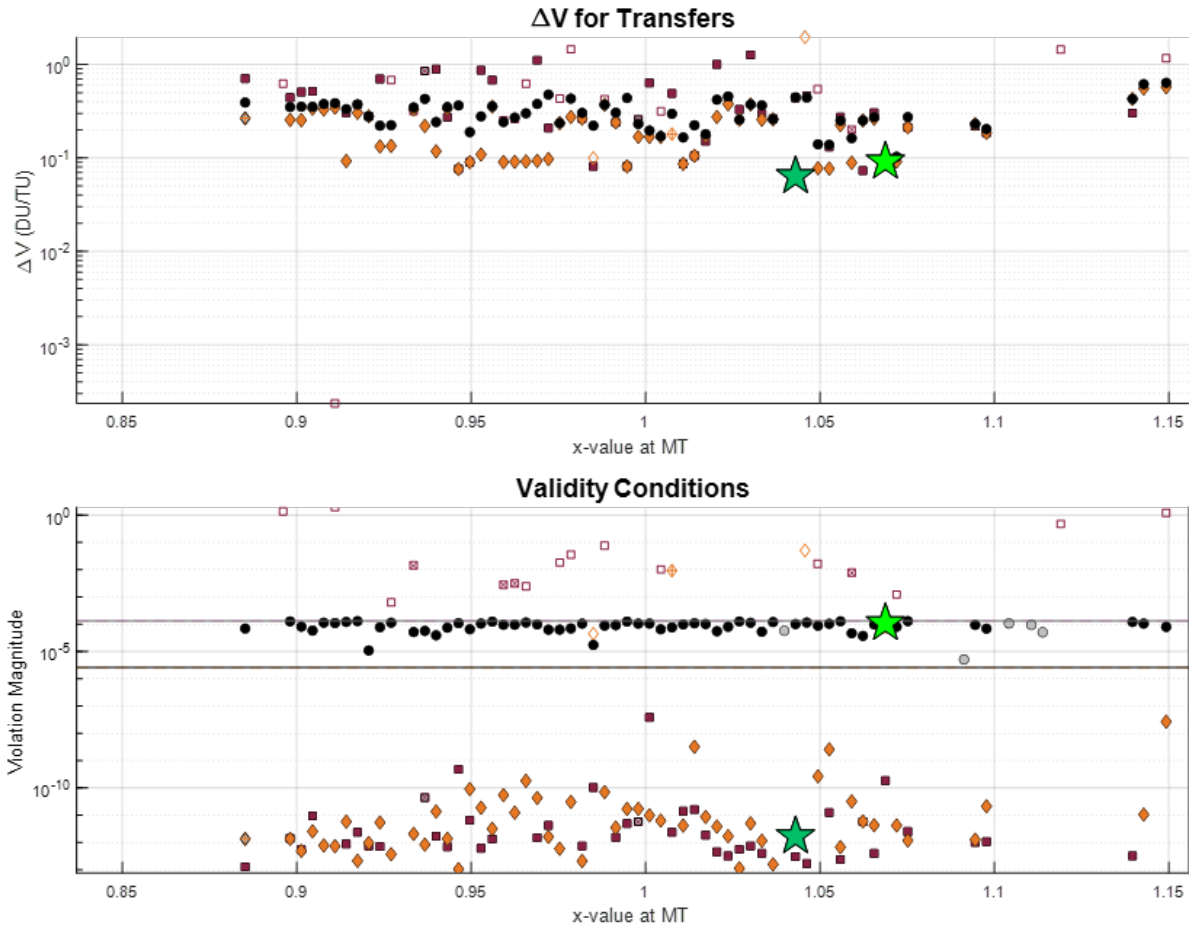

Figure 4.19: Total ΔV and Constraint Violation of the Correction Set 2 Transfers for Transfer 2. The total ΔVs are shown in the top plot and the maximum constraint violations are shown in the bottom plot. The maximum allowable constraint violation is indicated by the black line. The maximum allowable ΔP for the manifold transfers is shown by the gray line. Black dots indicate the best manifold transfers (same data as shown in Figure 4.13). Gray dots indicate the manifold transfer crashed into the Moon. Solid shapes indicate a valid corrected transfer. Maroon and orange indicate a corrected transfer of Type 1 and Type 2, respectively. Hollow shapes indicate the corrected transfer violated the maximum allowable constraint limit. Hollow shapes with "+"s or "x"s in the middle indicate the corrected transfer crashed into the Moon. The light green star indicates the best manifold transfer overall. The dark green star indicates the best corrected transfer from Set 2.

As can be seen in the figure above, for Set 2 correction models, the convergence of the manifold transfers did not appear to be heavily dependent on the value of x_{MT}. That being said, the convergence rate of Set 2 was significantly better than the convergence rate of Set 1.

While there appears to be one Type 1 corrected transfer that has a significantly lower ΔV than the other corrected transfers in this set, that transfer is invalid. As was the case for Set 1, for the most part, Set 2 Type 1 and Set 2 Type 2 appeared to find different corrected transfers for the same manifold transfer, with the ΔVs for the Type 1 corrected transfers often being greater compared to the ΔVs for the Type 2 corrected transfers. The best corrected transfer from Set 2 required less ΔV compared to both the best corrected transfer from Set 1 and the best manifold transfer overall. The value of x_{MT} corresponding to the best corrected transfer from Set 2 did shift compared to the value of x_{MT} corresponding to the best manifold transfer overall, but it was significantly closer to the best manifold transfer overall compared to the value of x_{MT} corresponding to the best Set 1 corrected transfer.

The spatial representations of each of the corrected transfers from Set 2, along with the best corrected transfer from Set 2, are provided in Figure 4.20.

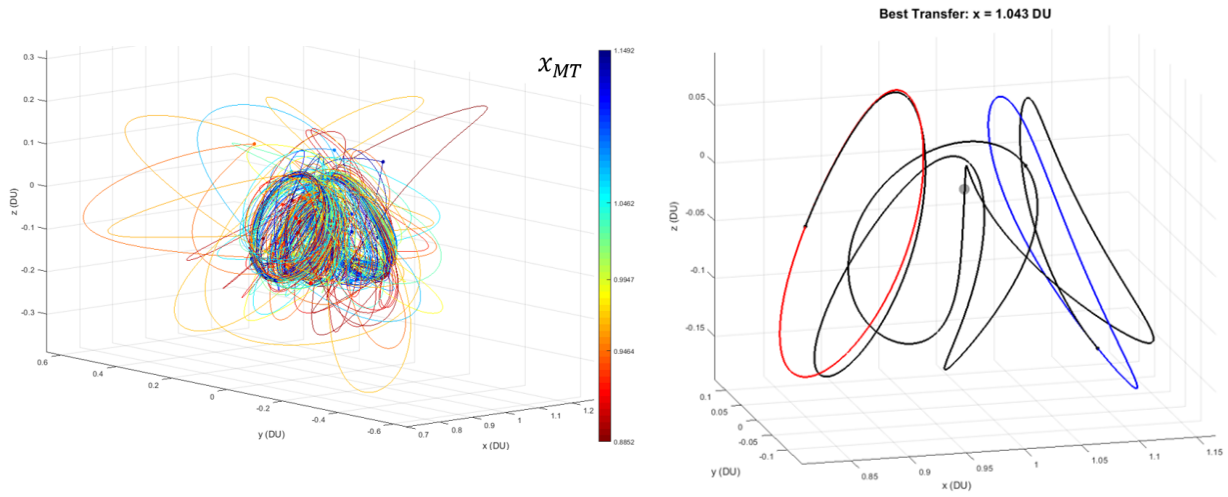

Figure 4.20: Transfers from Correction Set 2 for Transfer 2. Left: Corrected transfers from Set 2 at each specified value of x_{MT}. The color scale indicates the x_{MT} value of the manifold transfer used in the optimization scheme to generate each corrected transfer with maroon being at L_1 and navy being at L_2 (see Figure 4.13). Right: Best corrected transfer from Set 2 for Transfer 2. The black line represents the best transfer identified amongst all the possible corrected transfers from Set 2 for Transfer 2, which are shown on the left.

As can be seen on the left side of Figure 4.20, the spatial shapes of the some of the Set 2 corrected transfers were noticeably different than the manifold transfers on which they were

based, but less so compared to the Set 1 corrected transfers. The orthographic projections of the Set 2 corrected transfers are provided in Figure 4.21.

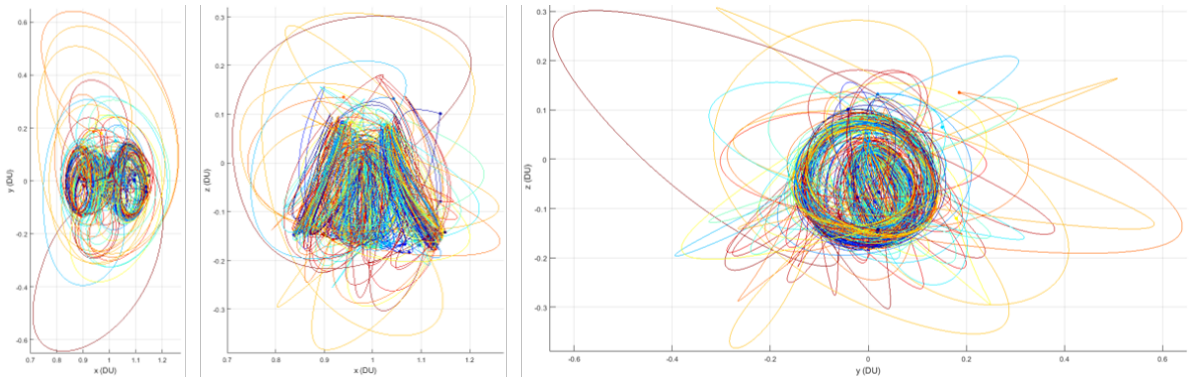

Figure 4.21: Transfers from Correction Set 2 for Transfer 2 (Orthographic Projections). Corrected transfers from Set 2 at each specified value of x_{MT}. The color scale indicates the x_{MT} value of the manifold transfer used in the optimization scheme to generate each corrected transfer with maroon being at L_1 and navy being at L_2 (see Figure 4.13). Left: x-y view (viewpoint looking down at the primaries' plane of motion). Middle: x-z view (viewpoint looking at the Moon with the Earth to the left). Right: y-z view (viewpoint from the other side of the Moon, relative to the Earth, and looking at the Moon).

The total ΔV and the magnitude of the maximum constraint violation for the Correction Set 3 transfers and the best manifold transfers for Transfer 2 are provided in Figure 4.22. As was the case for Set 1 and Set 2, for Set 3 correction models, the convergence of the manifold transfers did not appear to be heavily dependent on the value of x_{MT}. The convergence rate of Set 3 was the best of the three sets. Unlike Set 1 and Set 2, there were no invalid corrected transfers in Set 3 that had a ΔV lower than the best valid transfer in Set 3. Also, looking at left-hand side of the plots in Figure 4.22, there is clearly one Type 1 transfer that violated the same x_{MTN} constraint as there is no corresponding black dot at that value of x_{MT} (the best manifold transfer at that value of x_{MT} was invalid). For approximately half of the transfers where both types converged, Type 1 and Type 2 appeared to find different corrected transfers for the same manifold transfer. However, unlike the previous sets, the ΔVs for the Type 1 corrected transfers were sometimes lower compared to the ΔVs for the Type 2 corrected transfers. The best corrected transfers from Set 2 and Set 3 appear to be similar as they had the same corresponding value of x_{MT} and similar ΔVs.

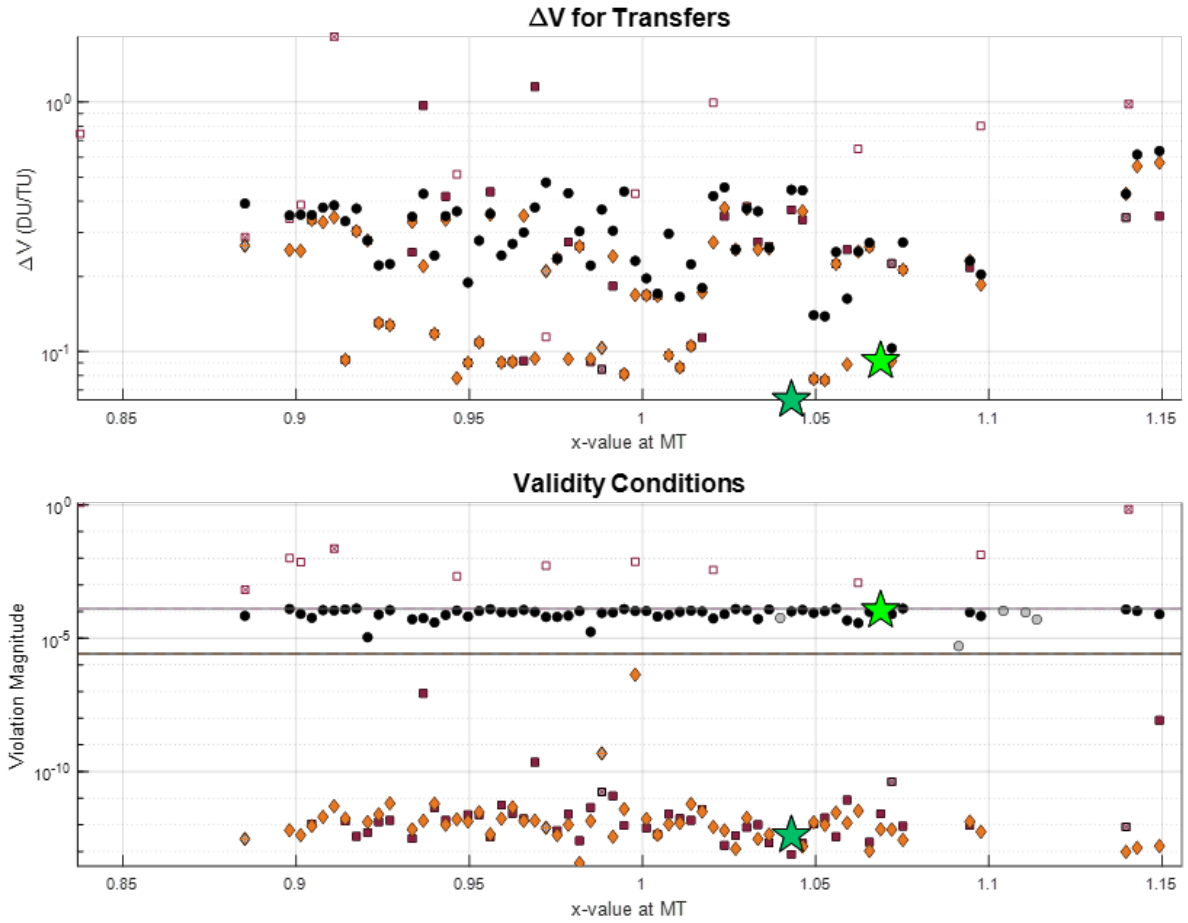

Figure 4.22: Total ΔV and Constraint Violation of the Correction Set 3 Transfers for Transfer 2. The total ΔVs are shown in the top plot and the maximum constraint violations are shown in the bottom plot. The maximum allowable constraint violation is indicated by the black line. The maximum allowable ΔP for the manifold transfers is shown by the gray line. Black dots indicate the best manifold transfers (same data as shown in Figure 4.13). Gray dots indicate the manifold transfer crashed into the Moon. Solid shapes indicate a valid corrected transfer. Maroon and orange indicate a corrected transfer of Type 1 and Type 2, respectively. Hollow shapes indicate the corrected transfer violated the maximum allowable constraint limit. Hollow shapes with "+"s or "x"s in the middle indicate the corrected transfer crashed into the Moon. The light green star indicates the best manifold transfer overall. The dark green star indicates the best corrected transfer from Set 3.

The spatial representations of each of the corrected transfers from Set 3, along with the best corrected transfer from Set 3, are provided in Figure 4.23. As can be seen on the left side of Figure 4.23, the spatial shapes of some of the corrected transfers were noticeably different than the manifold transfers on which they were based, but less so compared to both the Set 1 and Set 2 corrected transfers.

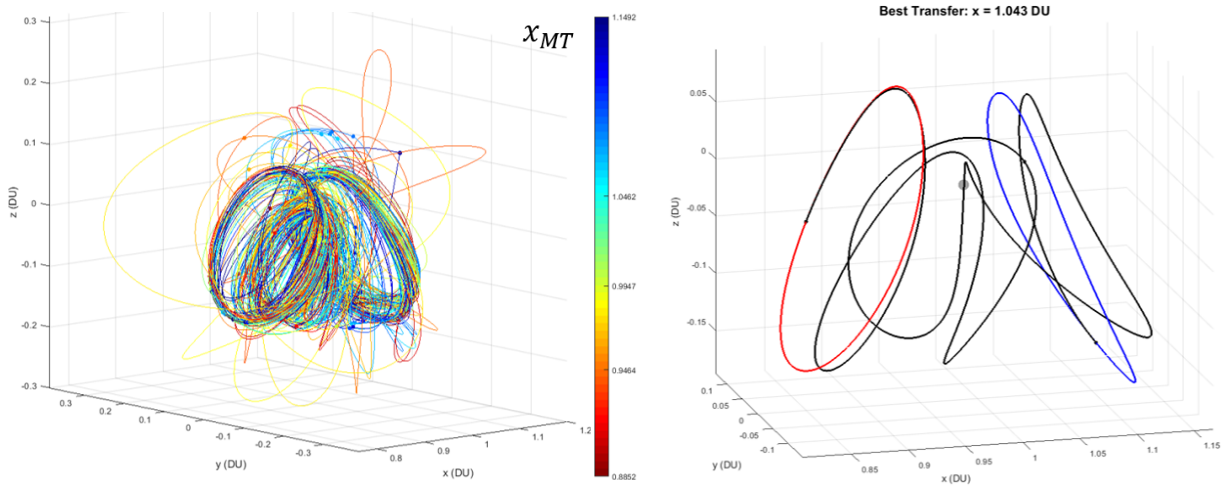

Figure 4.23: Transfers from Correction Set 3 for Transfer 2. Left: Corrected transfers from Set 3 at each specified value of x_{MT}. The color scale indicates the x_{MT} value of the manifold transfer used in the optimization scheme to generate each corrected transfer with maroon being at L_1 and navy being at L_2 (see Figure 4.13). Right: Best corrected transfer from Set 3 for Transfer 2. The black line represents the best transfer identified amongst all the possible corrected transfers from Set 3 for Transfer 2, which are shown on the left.

The orthographic projections of the Set 3 corrected transfers are provided in Figure 4.24.

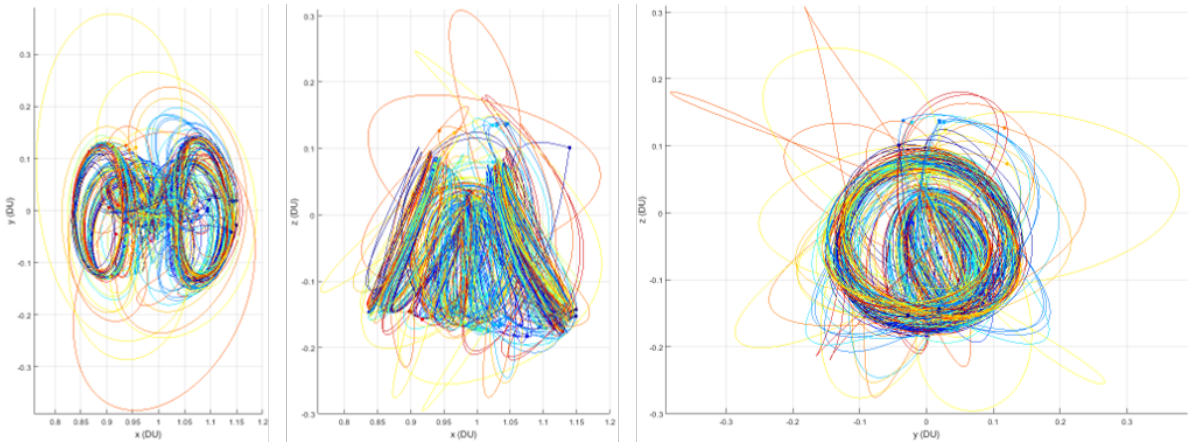

Figure 4.24: Transfers from Correction Set 3 for Transfer 2 (Orthographic Projections). Corrected transfers from Set 3 at each specified value of x_{MT}. The color scale indicates the x_{MT} value of the manifold transfer used in the optimization scheme to generate each corrected transfer with maroon being at L_1 and navy being at L_2 (see Figure 4.13). Left: x-y view (viewpoint looking down at the primaries' plane of motion). Middle: x-z view (viewpoint looking at the Moon with the Earth to the left). Right: y-z view (viewpoint from the other side of the Moon, relative to the Earth, and looking at the Moon).

4.2.4 Discussion

The success rate of the methodology used to identify valid manifold transfers, as well as data on the convergence of the correction models when applied to the best manifold transfers for Transfer 2, are provided in Table 4.3.

Convergence Transfer 2 3D Case 1	Valid Transfers		Met Constraint Violation Limit		No Moon Crash	
	Number	*%*	*Number*	*%*	*Number*	*%*
Original Transfers						
Manifold Transfers	**60**	**60**	65	65	95	95
Corrected Transfers						
Set 1 Type 1	**35**	**58.3**	36	60.0	56	93.3
Set 1 Type 2	**18**	**30.0**	21	35.0	57	95.0
Set 2 Type 1	**42**	**70.0**	44	73.3	54	90.0
Set 2 Type 2	**55**	**91.7**	56	93.3	58	96.7
Set 3 Type 1	**45**	**75.0**	48	80.0	54	90.0
Set 3 Type 2	**57**	**95.0**	60	100	57	95.0

Table 4.3: Convergence Results for Transfer 2. One manifold transfer for each of the 100 x_{MT} values was desired, so the manifold transfer convergence percentages are out of 100. An optimization scheme using each correction model was applied to each valid manifold transfer that was identified, so the correction model convergence percentages are out of the number of valid manifold transfers (60 for Transfer 2). Green or red values indicate the best or worst validity rate for the criteria in that column, respectively.

The much lower rate of success in identifying valid manifold transfers for Transfer 2 compared to Transfer 1 was not surprising. Even though the two orbits used in this transfer case had very similar Jacobi constant values, these orbits were 3D. A correction model of Type 2 had the worst convergence rate (Set 1 Type 2) and the best convergence rate (Set 3 Type 2). This result was also not surprising, as this behavior was also identified in the results for Transfer 1. As was the case in Transfer 1, correction models of Type 2 using more than three node points (Set 2 and Set 3) had high convergence rates. However, unlike for Transfer 1, correction models of Type 1 using more than three node points had convergence rates approximately 20% lower than the convergence rates for correction models of Type 2. Also unlike Transfer 1, a smaller set of transfer paths could not be identified amongst the best manifold transfers

or amongst any of the corrected sets for Transfer 2.

Characteristics of the best manifold transfer overall and the best corrected transfers found for each correction set for Transfer 2 are provided in Table 4.4.

Best Transfer Overall Transfer 2 3D Case 1	x_{MT} *DU*	ΔV *DU/TU*	TOF *TU*	Constraint Violation –	Correction Type –
Original Transfers					
Manifold Transfers	1.0688	**9.1567 $\times 10^{-2}$**	14.618	1.1056 $\times 10^{-4}$	N/A
Corrected Transfers					
Set 1	1.0011	**1.1547 $\times 10^{-1}$**	11.618	4.0497 $\times 10^{-11}$	1
Set 2	1.0430	**6.3930 $\times 10^{-2}$**	9.8316	1.7016 $\times 10^{-12}$	2
Set 3	1.0430	**6.3947 $\times 10^{-2}$**	9.8281	4.0540 $\times 10^{-13}$	2

Table 4.4: Characteristics of the Best Transfers for Transfer 2. Characteristics of the best transfer identified in the original set of manifold transfers, as well as for each corrected set of transfers. The constraint violation column has the maximum magnitude of the violation of any constraint used in the optimization process, and the units could be in DU or DU/TU depending on what specific type of constraint corresponded to the violation with the maximum magnitude. A green value indicates the best corrected transfer overall.

As mentioned earlier in Section 4.2.3, the best corrected transfers from Set 2 and Set 3 appear to be similar. This statement is supported by the data in Table 4.4. The fact that those two sets found similar transfers is a good indication that a corrected transfer with a sufficiently low ΔV was identified using this methodology.

4.3 Transfer 3: 3D Case 2

With the results of Transfer 2 providing further evidence that this methodology is effective, one more transfer case was considered. This transfer case will be referred to as "Transfer 3" or "3D Case 2". The transfer will between the same L_1 halo orbit from Transfer 2, but unlike Transfer 2, the planned orbit of the Lunar Gateway will be used as the other orbit.

4.3.1 Selected Parameters & Orbits

A differential correction scheme was used on initial conditions for halo orbits around L_1 from Grebow [1] (results were in Table 3.4 in that document) to obtain valid initial conditions for the halo orbit that was used in this transfer case. A differential correction scheme was also used on the planned orbit of the Lunar Gateway (as described in Section 2.1.2). The L_1 halo orbit with a Jacobi constant value closest to the Jacobi constant value of the modified Gateway orbit ($C = 3.03812$) was selected as the initial orbit. The modified Gateway orbit was selected as the desired orbit. The two orbits that were selected for the analysis in this transfer case are highlighted in Figure 4.25.

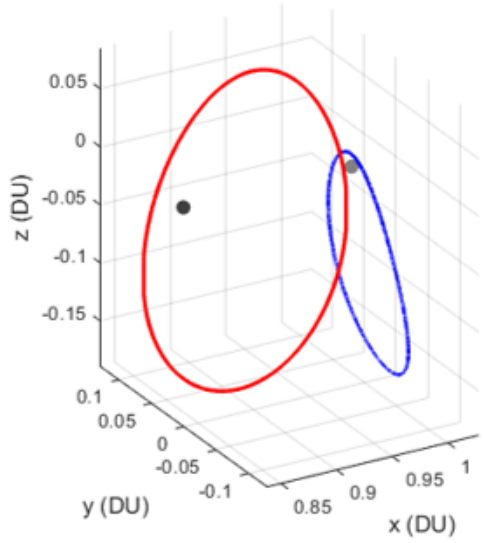

	Orbit 1	Orbit 2
Lagrange Point	L_1	L_2
Jacobi Constant	3.04269	3.04238
Initial Condition	$\begin{bmatrix} 0.836812615000000 \\ 0 \\ -0.147469552000000 \\ 0 \\ 0.256004070000000 \\ 0 \end{bmatrix}$	$\begin{bmatrix} 0.987530952112453 \\ -2.47248916941290 \times 10^{-18} \\ 0.0113348020483358 \\ -0.0169239502592414 \\ 1.43388071493305 \\ 0.00952573907372518 \end{bmatrix}$

Figure 4.25: Orbits Selected for Transfer 3. Left: The initial orbit (red) is an L_1 halo orbit and the final orbit (blue) is an L_2 NRHO which is one possible orbit for the planned Lunar Gateway (modified from Williams et al. [2]). The gray dot is the Moon and the black dot is L_1. Right: Table providing characteristics of the two selected orbits.

Except for the allowable ΔP at the manifold transition point, the same manifold transfer parameters that were used for this transfer were also used for Transfer 1 and Transfer 2. A total of 100 values, linearly spaced between L_1 and L_2, were selected as the possible x-values of the transition point between the manifolds. 1,000 equally spaced points along each orbit were used to generate the manifold trajectories. A step size of 6.5×10^{-5} DU ($d = 25$ km)

was used to determine the states on the manifolds. The states on the manifolds were then propagated forward/backward in time from 0 TU to ±10 TU for the unstable and stable manifold trajectories, respectively. Both positive and negative crossings of each Poincaré section with the same x-value were considered. MATLAB's *ode113* function was used with a tolerance of 10^{-13} to integrate the equations of motion. At each value of x_{MT}, pairs of states with $\Delta P \leq 2.6 \times 10^{-4}$ DU (100 km) were considered states on valid possible transfers.

4.3.2 Results for Manifold Transfers

The ΔVs and ΔPs at the manifold transition point for the best transfers are in Figure 4.26.

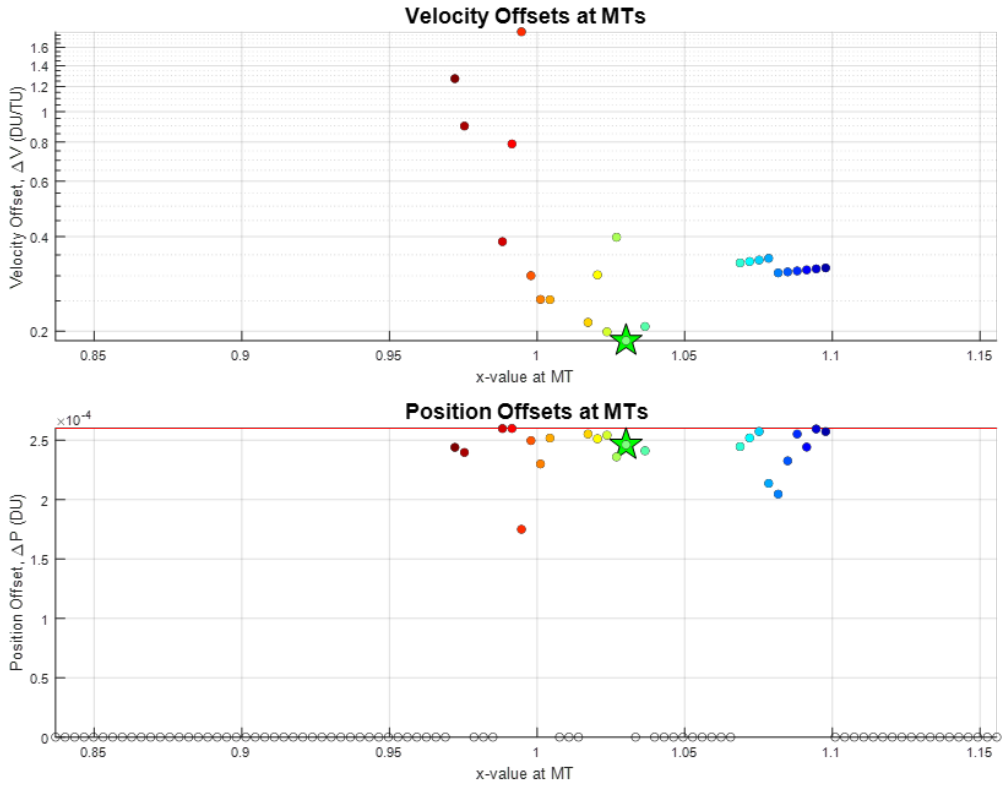

Figure 4.26: Position and Velocity Offsets at the Manifold Transfer Point of the Best Manifold Transfers for Transfer 3. The velocity offsets are shown in the top plot and the position offsets are shown in the bottom plot. The maximum allowable position offset is indicated by the red line. Gray dots indicate the transfer crashed into the Moon. The light green star indicates the best manifold transfer overall. The color scale indicates the value of x_{MT} for each transfer, with maroon being at L_1 and navy being at L_2, and is the same as the color scale in Figure 4.27.

While the relationship between the ΔV and the x_{MT} of the best manifold transfers is not clearly discernible, there appears to be one group of manifold transfers with x_{MT} values between 1 and 1.05 DU that have lower ΔVs than the other manifold transfers. Even with a larger allowable ΔP at the manifold transition point, a manifold transfer that met the position continuity requirement was identified for only 24 of the 100 set values of x_{MT}. None of those 24 manifold transfers had a path that crashed into the Moon. An image of the best manifold transfers is provided on the left side of Figure 4.27. An image of the best manifold transfer overall is on the right side of Figure 4.27. At the x_{MT} of the best manifold transfer overall, $x_{MT} = 1.03011$ DU, $\Delta P = 2.4635 \times 10^{-4}$ DU, and a ΔV of 1.86656×10^{-1} DU/TU was required.

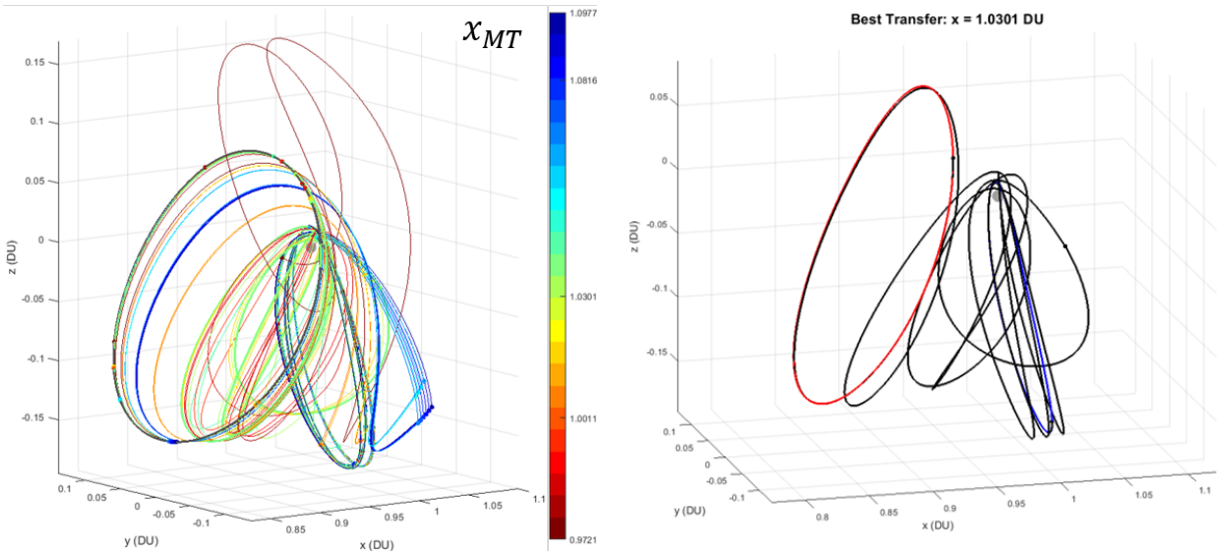

Figure 4.27: Best Identified Manifold Transfers for Transfer 3. Left: Best manifold transfers at each specified value of x_{MT}. The color scale indicates the value of x_{MT} for each manifold transfer with maroon being at L_1 and navy being at L_2 (see Figure 4.26). Right: Best manifold transfer overall for Transfer 3. The black line represents the best transfer identified amongst all the possible best manifold transfers for Transfer 3, which are shown on the left.

Images of the orthographic projections of the best manifold transfers for Transfer 3 are provided in Figure 4.28. Note that the transfers shown in Figure 4.28 are the same as those shown on the left side of Figure 4.27.

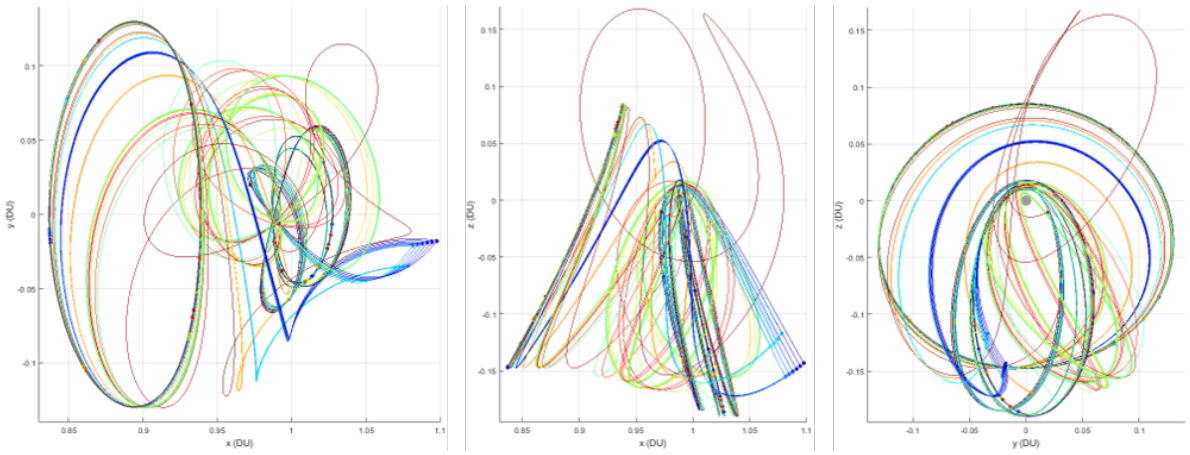

Figure 4.28: Best Identified Manifold Transfers for Transfer 3 (Orthographic Projections). Best manifold transfers at each specified value of x_{MT}. The color scale indicates the value of x_{MT} for each manifold transfer with maroon being at L_1 and navy being at L_2 (see Figure 4.26). Left: x-y view (viewpoint looking down at the primaries' plane of motion). Middle: x-z view (viewpoint looking at the Moon with the Earth to the left). Right: y-z view (viewpoint from the other side of the Moon, relative to the Earth, and looking at the Moon).

4.3.3 Results from Optimization

The total ΔV and the magnitude of the maximum constraint violation for each of the Correction Set 1 transfers and the best manifold transfers for Transfer 3, are provided in Figure 4.29. For Set 1 the convergence rate of the manifold transfers was better for transfers with a $x_{MT} \geq 1.05$ DU compared to those with a $x_{MT} < 1.05$ DU. There are three Type 1 corrected transfers that have significantly lower ΔVs than the other corrected transfers in this set, but they are invalid. For the most part, Set 1 Type 1 and Set 1 Type 2 appeared to find different corrected transfers for the same manifold transfer. For the transfers with a $x_{MT} \geq 1.05$ DU there was a clearer pattern; all those transfers converged for both types, and corrected transfers of Type 2 had lower ΔVs than the corresponding Type 1 corrected transfers and manifold transfers. The best corrected transfer from Set 1 had significantly better continuity characteristics, and had only a slightly higher ΔV compared to the best manifold transfer overall. The value of x_{MT} corresponding to the best corrected transfer from Set 1 was similar to the x_{MT} value of the best manifold transfer overall.

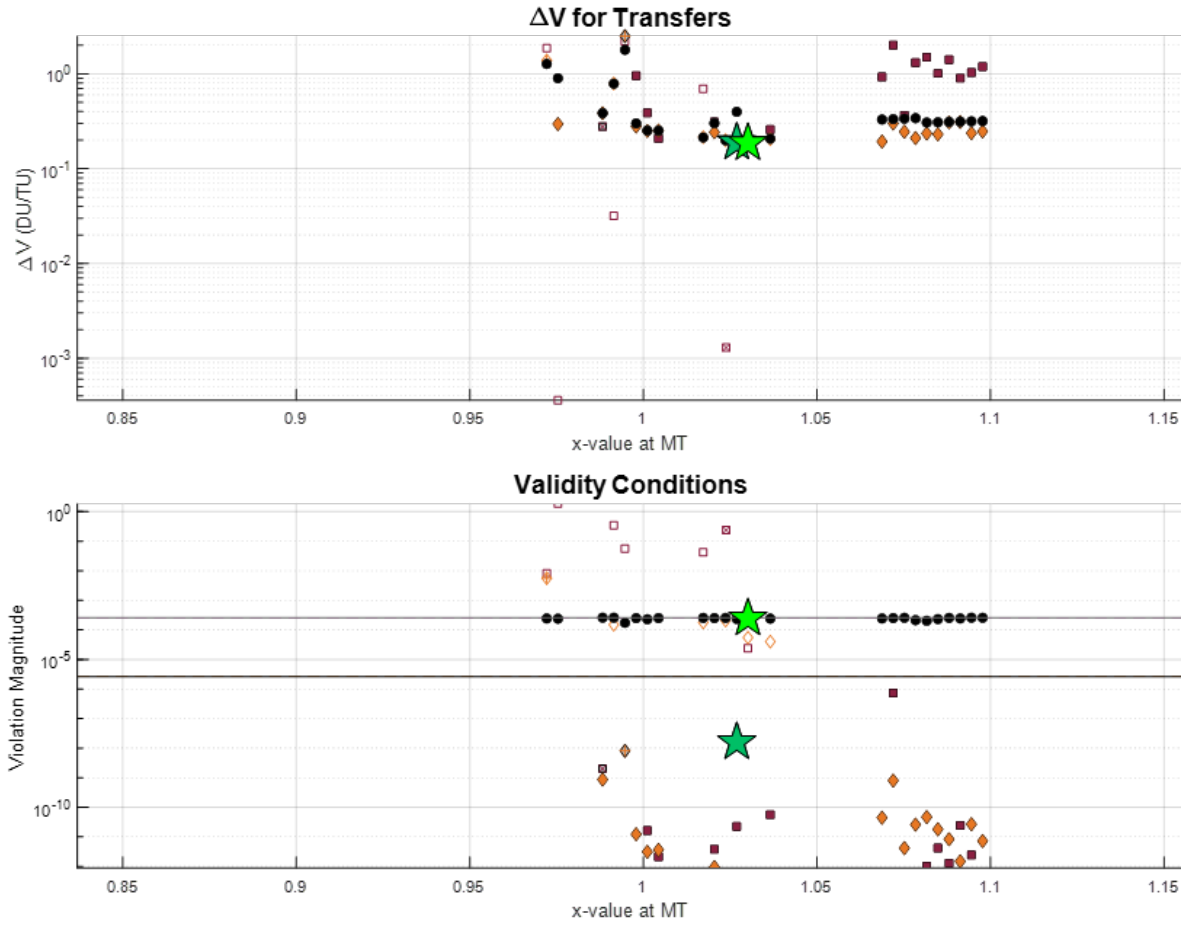

Figure 4.29: Total ΔV and Worst Constraint Violation of the Best Corrected Set 1 Transfers for Transfer 3. The total ΔVs are shown in the top plot and the maximum constraint violations are shown in the bottom plot. The maximum allowable constraint violation is indicated by the black line, and the maximum allowable position offset for the manifold transfers is shown by the gray line. Black dots indicate the best manifold transfers (same data as shown in Figure 4.26). Gray dots indicate the manifold transfer crashed into the Moon. Solid shapes indicate a valid corrected transfer. Maroon and orange indicate a corrected transfer of Type 1 and Type 2, respectively. Hollow shapes indicate the corrected transfer violated the maximum allowable constraint limit. Hollow shapes with "+"s or "x"s in the middle indicate the corrected transfer crashed into the Moon. The light green star indicates the best manifold transfer overall. The dark green star indicates the best corrected transfer from Set 1.

The spatial representations of each of the corrected transfers from Set 1, along with the best corrected transfer from Set 1 are provided in Figure 4.30. The spatial shapes of the some of the corrected transfers were noticeably different compared to the manifold transfers on which they were based. Some of the corrected transfers even went around the Earth.

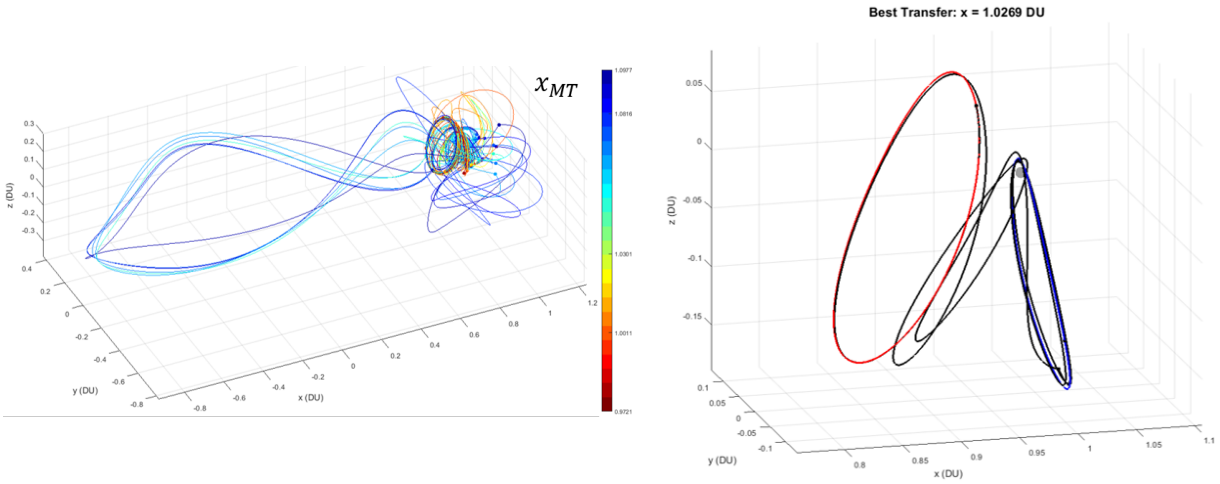

Figure 4.30: Transfers from Correction Set 1 for Transfer 3. Left: Corrected transfers from Set 1 at each specified value of x_{MT}. The color scale indicates the x_{MT} value of the manifold transfer used in the optimization scheme to generate each corrected transfer with maroon being at L_1 and navy being at L_2 (see Figure 4.26). Right: Best corrected transfer overall from Set 1 for Transfer 3 (black line).

The orthographic projections of the Set 1 corrected transfers are provided in Figure 4.31.

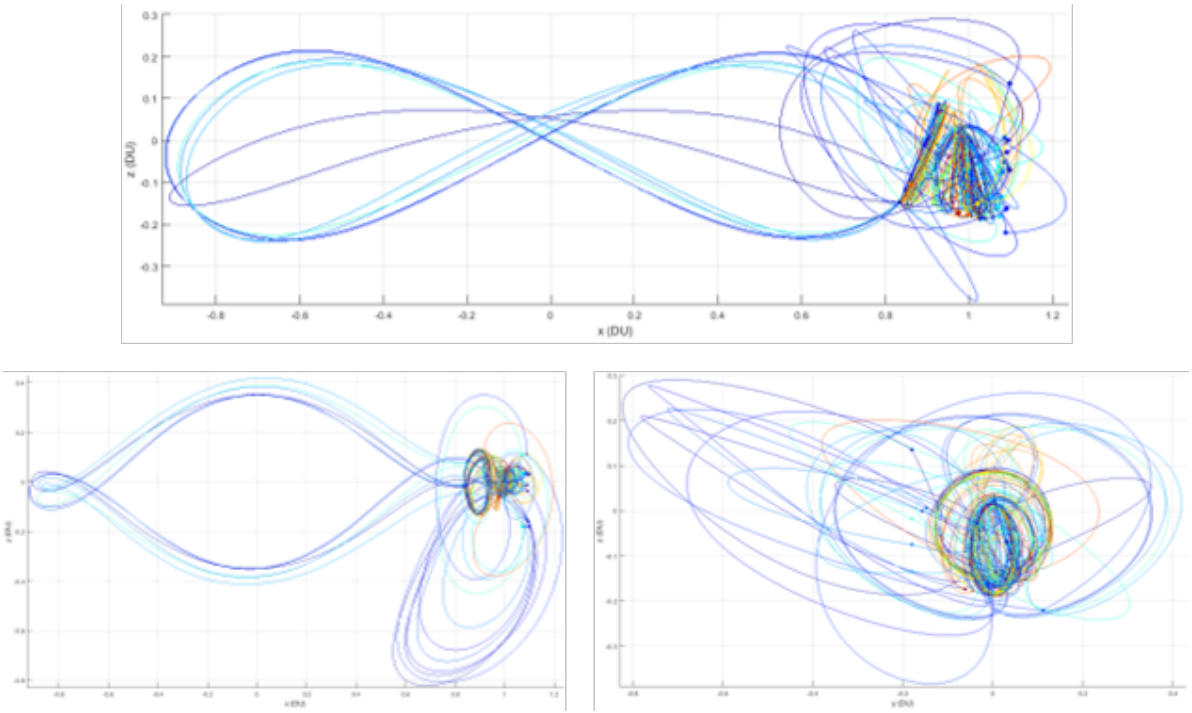

Figure 4.31: Transfers from Correction Set 1 for Transfer 3 (Orthographic Projections). Corrected transfers from Set 1 at each specified value of x_{MT}. The color scale indicates the value of x_{MT} for the manifold transfers used with maroon at L_1 and navy at L_2 (see Figure 4.26). Top: x-z view. Bottom Left: x-y view. Bottom Right: y-z view.

The total ΔV and the magnitude of the maximum constraint violation for the Correction Set 2 transfers and the best manifold transfers for Transfer 3 are provided in Figure 4.32.

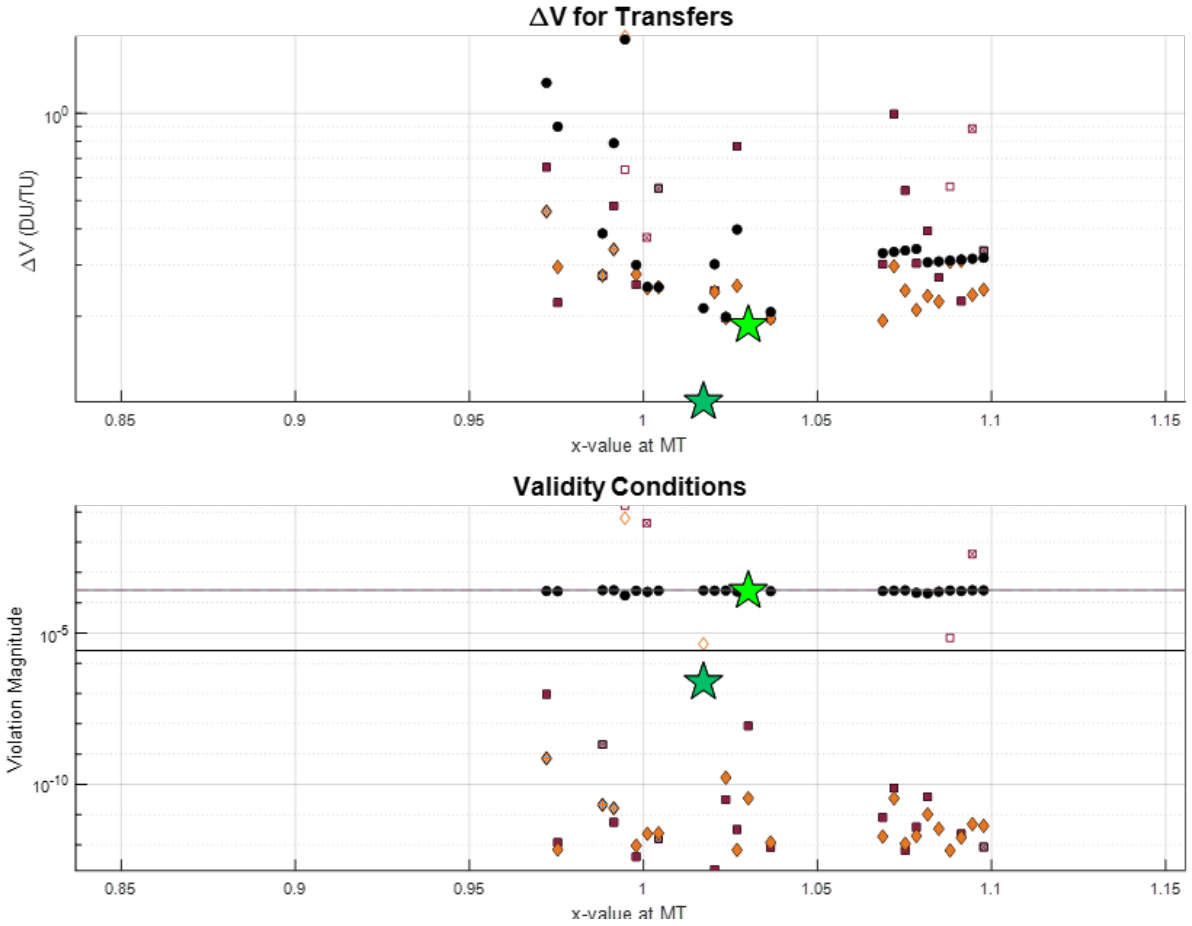

Figure 4.32: Total ΔV and Constraint Violation of the Correction Set 2 Transfers for Transfer 3. The total ΔVs are shown in the top plot and the maximum constraint violations are shown in the bottom plot. The maximum allowable constraint violation is indicated by the black line. The maximum allowable ΔP for the manifold transfers is shown by the gray line. Black dots indicate the best manifold transfers (same data as shown in Figure 4.26). Gray dots indicate the manifold transfer crashed into the Moon. Solid shapes indicate a valid corrected transfer. Maroon and orange indicate a corrected transfer of Type 1 and Type 2, respectively. Hollow shapes indicate the corrected transfer violated the maximum allowable constraint limit. Hollow shapes with "+"s or "x"s in the middle indicate the corrected transfer crashed into the Moon. The light green star indicates the best manifold transfer overall. The dark green star indicates the best corrected transfer from Set 2.

Similarly to Set 1, the convergence rate of the manifold transfers for Set 2 was better for transfers with a $x_{MT} \geq 1.05$ DU compared to those with a $x_{MT} < 1.05$ DU. There were no invalid corrected transfers that had a lower ΔV than the best corrected transfer overall

for this set. As was the case for Set 1, for the most part, Set 2 Type 1 and Set 2 Type 2 appeared to find different corrected transfers for the same manifold transfer, with the ΔVs for the Type 1 corrected transfers often being greater compared to the ΔVs for the Type 2 corrected transfers. Some of the transfers with a $x_{MT} \geq 1.05$ DU that had converged in Set 1 failed to converge in Set 2. Also different from Set 1, some of the Type 1 transfers with a $x_{MT} \geq 1.05$ DU had lower ΔVs than their corresponding manifold transfers. The best corrected transfer from Set 2 required less ΔV compared to both the best corrected transfer from Set 1 and the best manifold transfer overall. The value of x_{MT} corresponding to the best corrected transfer from Set 2 was similar, but closer to the Moon, compared to the value of x_{MT} corresponding to the best corrected transfer from Set 1.

The spatial representations of each of the corrected transfers from Set 2, along with the best corrected transfer from Set 2, are provided in Figure 4.33.

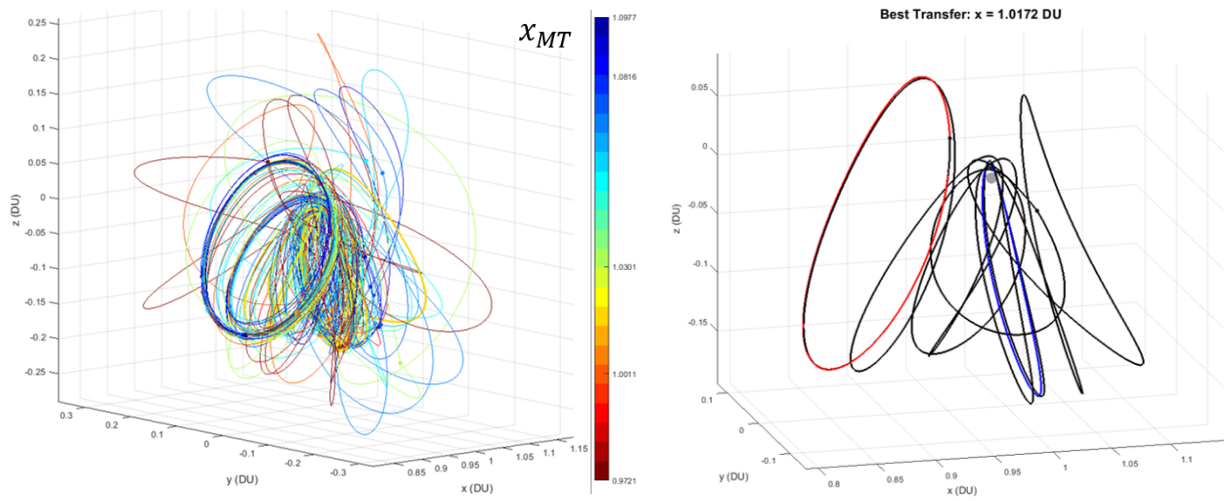

Figure 4.33: Transfers from Correction Set 2 for Transfer 3. Left: Corrected transfers from Set 2 at each specified value of x_{MT}. The color scale indicates the x_{MT} value of the manifold transfer used in the optimization scheme to generate each corrected transfer with maroon being at L_1 and navy being at L_2 (see Figure 4.26). Right: Best corrected transfer from Set 2 for Transfer 3. The black line represents the best transfer identified amongst all the possible corrected transfers from Set 2 for Transfer 3, which are shown on the left.

The spatial shapes of the some of the Set 2 corrected transfers were different compared to the manifold transfers on which they were based, as can be seen on the left side of Figure 4.33.

However, the Set 2 corrected transfers were more similar to the manifold transfers than the Set 1 corrected transfers. The orthographic projections of the Set 2 corrected transfers are provided in Figure 4.34.

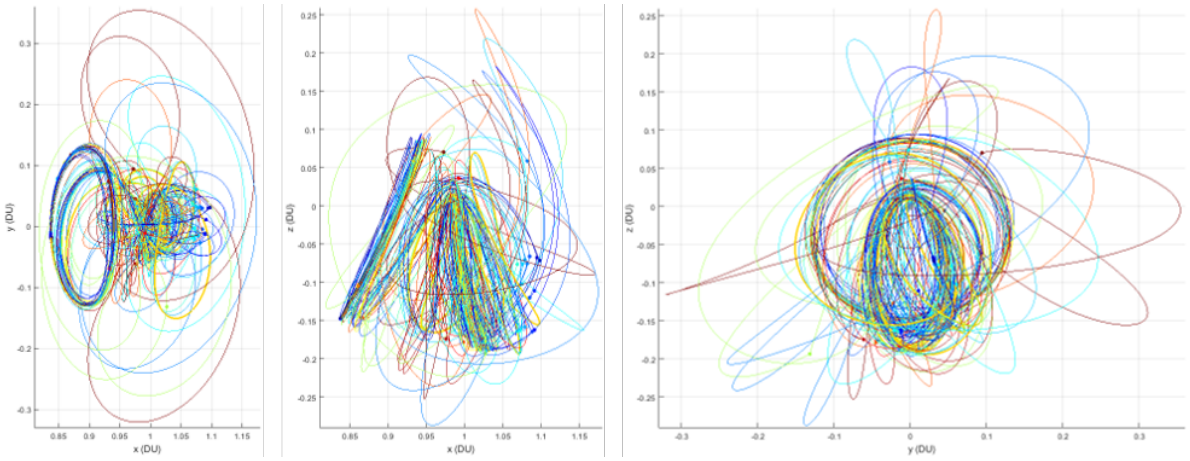

Figure 4.34: Transfers from Correction Set 2 for Transfer 3 (Orthographic Projections). Corrected transfers from Set 2 at each specified value of x_{MT}. The color scale indicates the value of x_{MT} for the manifold transfer used with maroon being at L_1 and navy being at L_2 (see Figure 4.26). Left: x-y view. Middle: x-z view. Right: y-z view.

The total ΔV and the magnitude of the maximum constraint violation for the Correction Set 3 transfers and the best manifold transfers for Transfer 3 are provided in Figure 4.35. Unlike the results for Set 1 and Set 2, for Set 3, the convergence rate of the manifold transfers was better for transfers with a $x_{MT} < 1.05$ DU compared to those with a $x_{MT} \geq 1.05$ DU. Unlike Transfer 1 and Transfer 2, for this transfer case, the convergence rates of Set 3 were worse than the convergence rates of Set 2. While for the most part Set 3 Type 1 and Set 3 Type 2 appeared to find different corrected transfers for the same manifold transfer, there were some instances where the ΔVs for the Type 1 and Type 2 transfers were similar to each other. For the transfers with a $x_{MT} \geq 1.05$ DU, some of the transfers that converged in the Sets 1 and 2 failed to converge in Set 3. Also different from Set 1 and Set 2, one of the valid Type 2 transfers with a $x_{MT} \geq 1.05$ DU had a larger ΔV than the corresponding manifold transfer. The best corrected transfer from Set 3 had a significantly lower ΔV compared to the best corrected transfer from Set 2, but they had the same corresponding value of x_{MT}.

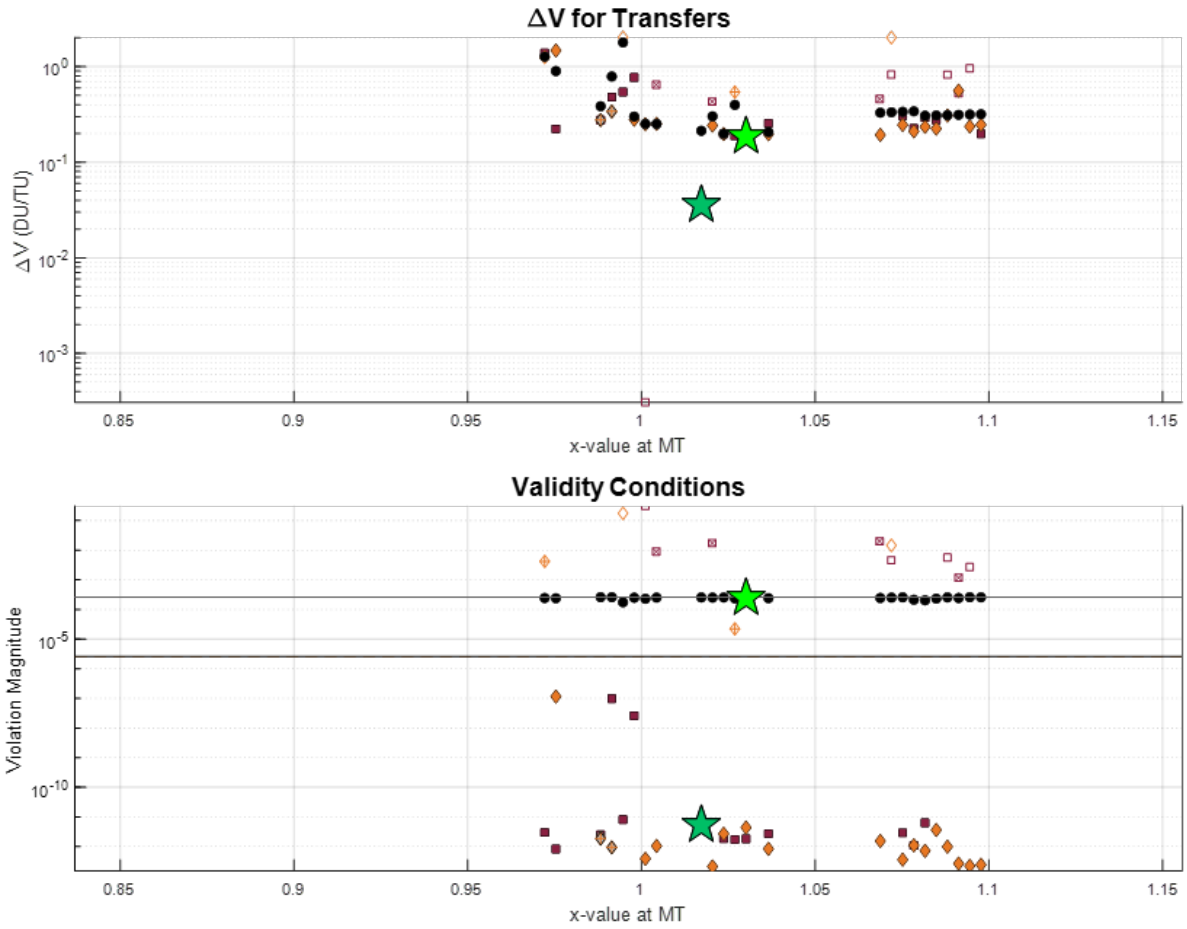

Figure 4.35: Total ΔV and Constraint Violation of the Correction Set 3 Transfers for Transfer 3. The total ΔVs are shown in the top plot and the maximum constraint violations are shown in the bottom plot. The maximum allowable constraint violation is indicated by the black line. The maximum allowable ΔP for the manifold transfers is shown by the gray line. Black dots indicate the best manifold transfers (same data as shown in Figure 4.26). Gray dots indicate the manifold transfer crashed into the Moon. Solid shapes indicate a valid corrected transfer. Maroon and orange indicate a corrected transfer of Type 1 and Type 2, respectively. Hollow shapes indicate the corrected transfer violated the maximum allowable constraint limit. Hollow shapes with "+"s or "x"s in the middle indicate the corrected transfer crashed into the Moon. The light green star indicates the best manifold transfer overall. The dark green star indicates the best corrected transfer from Set 3.

The spatial representations of each of the corrected transfers from Set 3, along with the best corrected transfer from Set 3, are provided in Figure 4.36. As can be seen on the left side of Figure 4.36, the spatial shapes of some of the Set 3 corrected transfers were different compared to the manifold transfers on which they were based, but significantly less so than as was the case for the Set 1 corrected transfers.

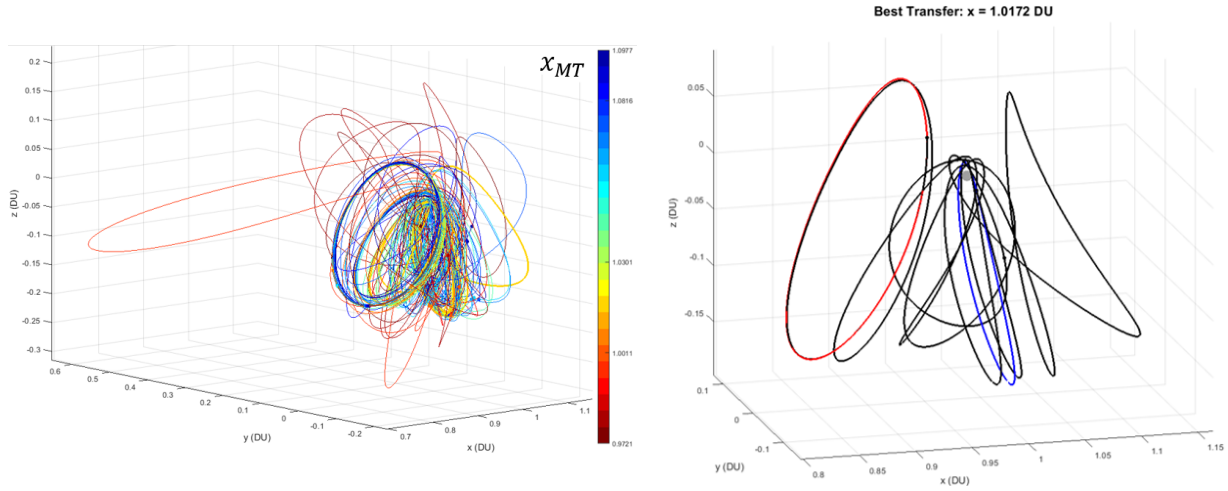

Figure 4.36: Transfers from Correction Set 3 for Transfer 3. Left: Corrected transfers from Set 3 at each specified value of x_{MT}. The color scale indicates the x_{MT} value of the manifold transfer used in the optimization scheme to generate each corrected transfer with maroon being at L_1 and navy being at L_2 (see Figure 4.26). Right: Best corrected transfer from Set 3 for Transfer 3. The black line represents the best transfer identified amongst all the possible corrected transfers from Set 3 for Transfer 3, which are shown on the left.

The orthographic projections of the Set 3 corrected transfers are provided in Figure 4.37.

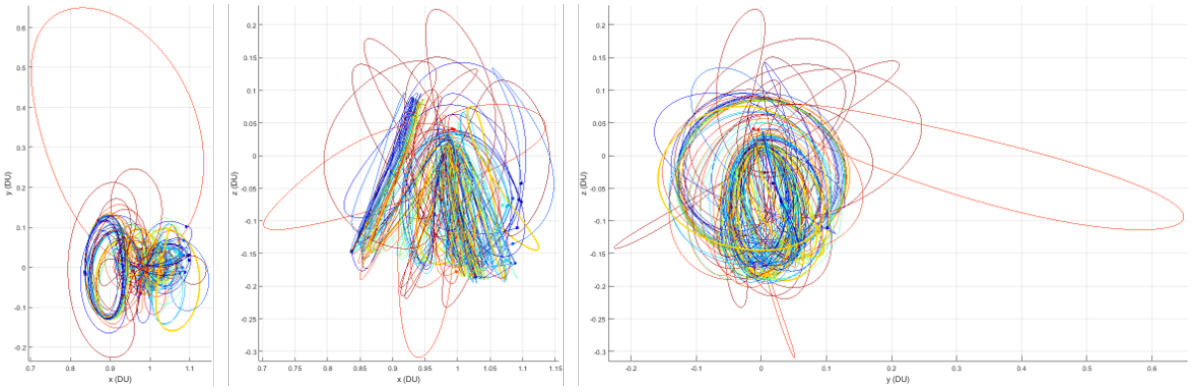

Figure 4.37: Transfers from Correction Set 3 for Transfer 3 (Orthographic Projections). Corrected transfers from Set 3 at each specified value of x_{MT}. The color scale indicates the x_{MT} value of the manifold transfer used in the optimization scheme to generate each corrected transfer with maroon being at L_1 and navy being at L_2 (see Figure 4.26). The transfers in these plots are the corrected transfers from Set 3, which are based on the manifold transfers shown in Figure 4.27 and Figure 4.28. Left: x-y view. Middle: x-z view. Right: y-z view.

4.3.4 Discussion

The success rate of the methodology used to identify valid manifold transfers, as well as data on the convergence of the correction models when applied to the best manifold transfers for Transfer 3, are provided in Table 4.5.

Convergence Transfer 3 3D Case 2	Valid Transfers		Met Constraint Violation Limit		No Moon Crash	
	Number	*%*	*Number*	*%*	*Number*	*%*
Original Transfers						
Manifold Transfers	**24**	**24**	24	24	100	100
Corrected Transfers						
Set 1 Type 1	**16**	**66.7**	17	70.8	22	91.7
Set 1 Type 2	**17**	**70.8**	18	75.0	22	91.7
Set 2 Type 1	**17**	**70.8**	20	83.3	19	79.2
Set 2 Type 2	**19**	**79.2**	22	91.7	21	87.5
Set 3 Type 1	**15**	**62.5**	16	66.7	19	79.2
Set 3 Type 2	**18**	**75.0**	20	83.3	20	83.3

Table 4.5: Convergence Results for Transfer 3. One manifold transfer for each of the 100 x_{MT} values was desired, so the manifold transfer convergence percentages are out of 100. An optimization scheme using each correction model was applied to each valid manifold transfer that was identified, so the correction model convergence percentages are out of the number of valid manifold transfers (24 for Transfer 3). Green or red values indicate the best or worst validity rate for the criteria in that column, respectively.

Possible reasons why there was a much lower success rate in identifying valid manifold transfers for this transfer case, compared to Transfer 1 and Transfer 2, will be discussed later in this section. A correction model that was neither Set 1 nor Type 2 had the worst convergence rate (Set 3 Type 1). For both Transfer 1 and Transfer 2 the correction model with the worst convergence rate was Set 1 Type 2. A correction model of Type 2 that was not Set 3 had the best convergence rate (Set 2 Type 2). Both Type 1 and Type 2 transfers in Set 3 had worse convergence rates than in Set 2. As the number of nodes increased, the difference between the convergence rates of Type 2 and Type 1 increased.

Some similar paths could be identified amongst the best manifold transfers for Transfer 3

which are shown in Figure 4.27 and Figure 4.28. Two distinct transfer paths were identified amongst the ten best manifold transfers with x_{MT} values greater than 1.05 DU. The first four of those transfers appear to follow similar paths to one another (the four transfers with the smallest values of x_{MT} that were greater than 1.05 DU, or the cyan transfers). The remaining six of those transfers appear to follow similar paths to one another (the blue to navy transfers). The two groupings of these 10 transfers can be identified in Figure 4.26. Transfers with similar transfer paths appear to have ΔVs that exhibit a continuous trend in the ΔV vs x_{MT} plot (e.g. increase linearly as x_{MT} increases). The transition between the two distinct paths is marked by a discontinuous jump in the ΔV vs x_{MT} plot. While some similar paths could be identified amongst the best manifold transfers for Transfer 3, a smaller set of similar transfer paths could not be identified amongst any of the corrected sets for this transfer case.

Characteristics of the best manifold transfer overall and the best corrected transfer found for each correction set for Transfer 3 are provided in Table 4.6.

Best Transfer Overall Transfer 3 3D Case 2	x_{MT} *DU*	ΔV *DU/TU*	TOF *TU*	Constraint Violation –	Correction Type –
Original Transfers					
Manifold Transfers	1.0301	**1.8666 $\times 10^{-1}$**	14.993	2.4635 $\times 10^{-4}$	N/A
Corrected Transfers					
Set 1	1.0269	**1.8938 $\times 10^{-1}$**	10.547	1.5953 $\times 10^{-8}$	2
Set 2	1.0172	**1.0154 $\times 10^{-1}$**	16.674	2.3908 $\times 10^{-7}$	1
Set 3	1.0172	**3.5789 $\times 10^{-2}$**	16.791	5.3881 $\times 10^{-12}$	2

Table 4.6: Characteristics of the Best Transfers for Transfer 3. Characteristics of the best transfer identified in the original set of manifold transfers, as well as for each corrected set of transfers. The constraint violation column has the maximum magnitude of the violation of any constraint used in the optimization process, and the units could be in DU or DU/TU depending on what specific type of constraint corresponded to the violation with the maximum magnitude. A green value indicates the best corrected transfer overall.

The best corrected transfers from Set 2 and Set 3 appear to have some similar characteristics, as they had the same x_{MT} and a similar TOF, even though the best corrected transfer from

Set 3 had a significantly lower ΔV than the best corrected transfer from Set 2. As the best corrected transfers in Set 2 and Set 3 had different ΔVs, there is no indication that a corrected transfer with a sufficiently low ΔV was identified using this methodology for this specific transfer case.

Limited Success of the Methodology When Applied to Transfer 3

The significantly lower success rate in identifying valid manifold transfers for Transfer 3, compared to Transfer 1 and Transfer 2, was not surprising. Even though the two orbits used in this transfer case had similar Jacobi constant values, not only were these orbits 3D but, in the region defined by the input parameters, the trajectories on the NRHO's stable manifold rarely intersected with the trajectories on the unstable manifold of the initial orbit. The relatively small number of manifold intersections for the two orbits used in this case, compared to the two Lyapunov orbits used in Transfer 1 and the two halo orbits used in Transfer 2, can be seen in Figure 4.38.

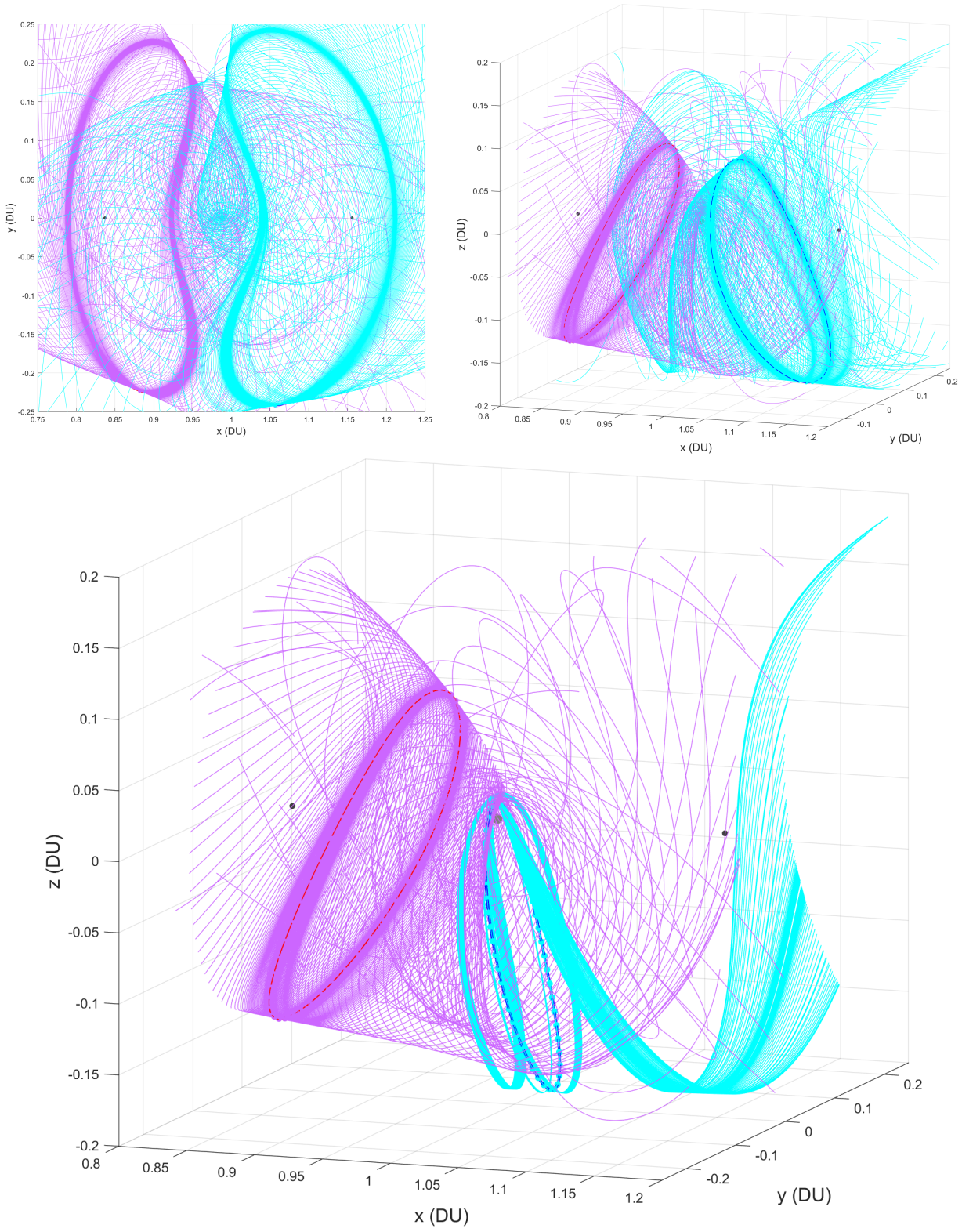

Figure 4.38: Manifolds of the Orbits Used in the Transfer Cases. These plots are focused on the space around the Moon. Purple and cyan lines are Orbit 1 unstable and Orbit 2 stable manifold trajectories, respectively. Top Left: Orbit manifolds for Transfer 1. Top Right: Orbit manifolds for Transfer 2. Bottom: Orbit manifolds for Transfer 3.

Chapter 5

Conclusion

5.1 Summary

A methodology to identify low-cost transfers between orbits in the CR3BP was developed. This methodology leverages tools related to dynamical systems theory, such as manifolds and Poincaré sections, as well as techniques related to differential corrections and optimization. This methodology was applied to three transfer cases. The first was a test case in the PCR3BP for a transfer from a L_1 Lyapunov orbit to a L_2 Lyapunov orbit. The results obtained for the best manifold transfer indicated this methodology was effective. The results obtained from the optimization scheme on the manifold transfers indicated that a sufficient transfer between the two orbits was identified. The second case was for a transfer in the CR3BP from a L_1 halo orbit to a L_2 halo orbit. While less valid manifold transfers were identified with the input parameters used, the results still indicated that the methodology was effective in identifying valid manifold transfers. Like for the first case, the results obtained from the optimization scheme on the manifold transfers for the second case indicated that a sufficient transfer between the two orbits was identified. The final case was for a transfer in the CR3BP from a L_1 halo orbit to one possible orbit for the Lunar Gateway (a NRHO about L_2). The results indicated that the initial orbit's unstable manifold did not have a large number of intersections with the final orbit's stable manifold in the space defined by the selected input values. The results from the optimization scheme were inconclusive as to whether a sufficient transfer between the two orbits was identified for this case.

While the relationship between ΔV and x_{MT} was relatively the same for the best manifold transfers and the corrected transfers in Transfer 1, this was not the case for Transfer 2 and Transfer 3. When using more than three nodes to discretize the best manifold transfers, discretizing the transfers using Type 2 often resulted in corrected transfers that performed better than those that resulted from using Type 1. Also, when using more than three nodes, Type 2 converged to a valid corrected transfer more often than Type 1 did. In Transfer 1, the best manifold transfer overall and the best corrected transfer overall followed very similar paths with similar TOFs, although they had noticeably different ΔVs and continuity characteristics. In Transfer 2 and Transfer 3, the best manifold transfer overall and the best corrected transfer overall followed noticeably different paths, even though the paths shared some similar characteristics. For all transfer cases, the best corrected transfer overall had significantly better continuity characteristics compared to the best manifold transfer overall. However, the best corrected transfer overall had a lower ΔV compared to the best corrected transfer overall only in Transfer 2 and Transfer 3, not in Transfer 1. These results indicate that for transfer cases similar to the three included in this analysis, applying this specific optimization scheme to manifold transfers obtained by using the methodology outlined in Section 3.1 will likely yield a substantially better transfer.

5.2 Future Work

Additional work is needed to verify that this methodology can be effectively applied to transfers between additional types of orbits in the CR3BP. This methodology is heavily dependent on the input parameters used to identify the manifold transfers, particularly the type of restricted coordinate, the range of the restricted coordinate values, and the number of restricted coordinate values. If the manifolds for the two orbits do not have a large number of intersections in the space defined by the input values, then there is a low chance that the methodology will be able to identify a large number of valid manifold transfers. If

not enough manifold transfers are identified, then the likelihood that the characteristics of the best possible transfer are captured by the set of identified manifold transfers is low. As identifying a trend or result is easier when there are more data points, if not enough manifold transfers are identified, then the results of the optimization scheme might be inconclusive. For those reasons, the third transfer case should be tested again with a different set of values for the three input parameters mentioned previously in this paragraph. Some guidance as to what the values of these parameters should be can be obtained by observing where there are the most intersections of the orbits' manifolds (see Figure 4.38).

Other general items of future work that are unrelated to the issues discussed in the previous paragraph will now be addressed. The first item is to create more transfer cases with a wider variety of orbits. Transfer cases between orbits with a larger difference in their Jacobi constant values, as well as between orbits about L_3, L_4, and L_5, should be studied. The second item is to perform the optimization scheme with more nodes discretizing the manifold transfers. The most nodes used in this analysis was seven; maybe 11 or more nodes could be used. The third item is to study the effect of programmatically changing the magnitude of the step size onto the manifold. The effects of this change should be considered, particularly those related to effectiveness in identifying better manifold transfers, efficiency in terms of computation time and capability needed, and complexity of integrating the necessary changes into the current methodology. It is also important to mention that the dynamics model used in this study ignored the gravitational effects of the Sun on the system, as well as other perturbations. To include these effects, the equations of motion and the differential equations for the STM would need to be updated.

5.3 Conclusions

Overall, the methodology developed and used in this analysis shows some promise as it can identify transfers between orbits in the CR3BP that do not have the same Jacobi constant value. As long the unstable manifold trajectories of the initial orbit intersect the stable manifold trajectories of the final orbit, and the input parameters define a space that adequately capture these intersections, this methodology appears to be effective. More analysis is needed to verify this methodology is effective for a wide variety of orbits in the CR3BP. Programs used for transfer design that have higher fidelity dynamics models and more advanced optimization schemes currently exist. However, as indicated by the results of the three transfer cases examined in this study, the methodology outlined in this document can be used to obtain an initial guess for the characteristics of a sufficient transfer between two orbits in the CR3BP.

Bibliography

[1] Grebow, D. J., "Generating Periodic Orbits in the Circular Restricted Three-Body Problem with Applications to Lunar South Pole Coverage," Master's thesis, Purdue University, May 2006. URL https://engineering.purdue.edu/people/kathleen.howell.1/Publications/Masters/2006_Grebow.pdf, accessed: 8 Feb 2020.

[2] Williams, J., Lee, D. E., Whitley, R. J., Bokelmann, K. A., Davis, D. C., and Berry, C. F., "Targeting Cislunar Near Rectilinear Halo Orbits for Human Space Exploration," *27th AAS/AIAA Space Flight Mechanics Meeting*, 2017. URL https://ntrs.nasa.gov/archive/nasa/casi.ntrs.nasa.gov/20170001352.pdf, accessed: 8 Feb 2020.

[3] Pritchett, R. E., "Numerical Methods for Low-Thrust Trajectory Optimization," Master's thesis, Purdue University, August 2016. URL https://engineering.purdue.edu/people/kathleen.howell.1/Publications/Masters/2016_Pritchett.pdf, accessed: 8 Feb 2020.

[4] Gerstenmaier, W., and Crusan, J., "Cislunar and Gateway Overview," [online], Sep 2018. URL https://www.nasa.gov/sites/default/files/atoms/files/cislunar-update-gerstenmaier-crusan-v5a.pdf, accessed: 1 May 2020.

[5] Frank, J., "LSU PHYS 7221 Lecture - The Three-Body Problem," , Oct 2006.

[6] Schroeder, K., "Virginia Tech AOE 4314 Lecture: The Three-Body Problem," , Nov 2017.

[7] Szebehely, V., *Theory of Orbits: The Restricted Problem of Three Bodies*, Academic Press, 1967.

[8] Koon, W., Lo, M., Marsden, J., and Ross, S., "Dynamical Systems, the Three-Body Problem and Space Mission Design," , 2006.

[9] Schaub, H., and Junkins, J. L., *Analytical Mechanics of Aerospace Systems*, 3rd ed., AIAA Education Series, AIAA, 2002.

[10] Farquhar, R. W., "The Control and Use of Libration-Point Satellites," Ph.D. thesis, Stanford University, Jul 1968.

[11] Breakwell, J. V., and V., B. J., "The halo family of 3-dimensional periodic orbits in the Earth-Moon restricted 3-body problem," *Celestial Mechanics*, Vol. 20, 1979, pp. 389–404.

[12] Howell, K. C., "Three-dimensional, periodic, 'halo' orbits," *Celestial Mechanics*, Vol. 32, 1984, pp. 53–71.

[13] Zimovan, E. M., "Characteristics And Design Strategies For Near Rectilinear Halo Orbits Within The Earth-Moon System," Master's thesis, Purdue University, Aug 2017. URL https://engineering.purdue.edu/people/kathleen.howell.1/Publications/Masters/2017_Zimovan.pdf, accessed: 8 Feb 2020.

[14] Richardson, D. L., "Analytic construction of periodic orbits about the collinear points," *Celestial Mechanics*, Vol. 22, 1980.

[15] Howell, K. C., and Breakwell, J. V., "Almost rectilinear halo orbits," *Celestial Mechanics*, Vol. 32, 1984, pp. 29–52.

[16] D'Amario, L. A., "Minimum impulse three-body trajectories," Ph.D. thesis, Massachusetts Institute of Technology, Jun 1973. URL https://dspace.mit.edu/handle/1721.1/12370, accessed: 1 May 2020.

[17] Rausch, R. R., "Earth to Halo Orbit Transfer Trajectories," Master's thesis, Purdue University, Aug 2005. URL https://engineering.purdue.edu/people/kathleen.howell.1/Publications/Masters/2017_Zimovan.pdf, accessed: 8 Feb 2020.

[18] Gómez, G., Koon, W. S., Lo, M. W., Marsden, J. E., Masdemont, J., and Ross, S. D., "Invariant Manifolds, The Three-Body Problem And Space Mission Design," *Advances in the Astronautical Sciences*, Vol. 109, No. 1, 2001, pp. 3–22.

[19] Haapala, A. F., Vaquero, M., Pavlak, T. A., Howell, K. C., and Folta, D. C., "Trajectory Selection Strategy For Tours In The Earth-Moon System," 2013. URL https://engineering.purdue.edu/people/kathleen.howell.1/Publications/Conferences/2013_AAS_HaaVaqPavHowFol.pdf, accessed: 1 May 2020.

[20] Schlei, W. R., "An Application of Visual Analytics to Spacecraft Trajectory Design," Master's thesis, Purdue University, Dec 2011. URL https://engineering.purdue.edu/people/kathleen.howell.1/Publications/Masters/2011_Schlei.pdf, accessed: 8 Feb 2020.

[21] Schlei, W. R., "Interactive Spacecraft Trajectory Design Strategies Featuring Poincaré Map Topology," Ph.D. thesis, Purdue University, May 2017. URL https://engineering.purdue.edu/people/kathleen.howell.1/Publications/Dissertations/2016_Bosanac.pdf, accessed: 1 May 2020.

[22] Howell, K. C., "Developing a Transportation Network in CisLunar Space," *AstroNet-II International Final Conference*, 2015.

[23] Farquhar, R. W., Muhonen, D. P., Newman, C. R., and Heubergerg, H. S., "Trajectories and Orbital Maneuvers for the First Libration-Point Satellite," *Journal of Guidance, Control, and Dynamics*, Vol. 3, No. 6, 1980, pp. 549–554.

[24] Siddiqi, A. A., "Deep Space Chronicle: A Chronology of Deep Space and Planetary Probes 1958-2000," Tech. Rep. SP 2002-4524, NASA, Jun 2002. URL https://ntrs.nasa.gov/archive/nasa/casi.ntrs.nasa.gov/20020052429.pdf, accessed: 1 May 2020.

[25] Barden, B. T., Howell, K. C., and Lo, M. W., "Application of dynamical systems theory to trajectory design for a libration point mission," 1996.

[26] Pritchett, R., Howell, K. C., and Folta, D. C., "Low-Thrust Trajectory Design for a Cislunar CubeSat Leveraging Structures from the Bicircular Restricted Four-Body Problem," *70th International Astronautical Congress*, 2019. URL https://ntrs.nasa.gov/archive/nasa/casi.ntrs.nasa.gov/20190032217.pdf, accessed: 13 Apr 2020.

[27] Ramanan, R. V., and Lal, M., "Analysis of optimal strategies for soft landing on the Moon from lunar parking orbits," *Journal of Earth System Science*, Vol. 114, No. 6, 2005.

[28] Shi, Y. Y., and Young, D. H., "Minimum fuel coplanar aeroassisted orbital transfer using collocation and nonlinear programming," *Flight Mechanics/Estimation Theory Symposium*, 1991. URL https://ntrs.nasa.gov/archive/nasa/casi.ntrs.nasa.gov/19920004877.pdf, accessed: 8 Feb 2020.

[29] Salazar, F., Macau, E. E. N., De Melo, C. F., and Winter, O. C., "Three-body problem, its Lagrangian points and how to exploit them using an alternative transfer to L4 and L5," *Celestial Mechanics and Dynamical Astronomy*, Vol. 114, No. 1, 2012. URL https://link.springer.com/article/10.1007%2Fs10569-012-9426-y, accessed: 31 Mar 2020.

[30] NASA Science Mission Directorate, "NASA Strategic Plan 2018," [online], 2018. URL https://www.nasa.gov/sites/default/files/atoms/files/nasa_2018_strategic_plan.pdf, accessed: 1 May 2020.

[31] NASA, "Gateway Memorandum for the Record," [online], May 2018. URL https://www.nasa.gov/sites/default/files/atoms/files/gateway_domestic_and_international_benefits-memo.pdf, accessed: 1 May 2020.

[32] Erickson, K., "Earth's Moon," [online], Dec 2019. URL https://solarsystem.nasa.gov/moons/earths-moon/in-depth/, accessed: 1 May 2020.

[33] Williams, D. R., "Moon Fact Sheet," [online], Jan 2020. URL https://nssdc.gsfc.nasa.gov/planetary/factsheet/moonfact.html, accessed: 1 May 2020.

[34] Analytical Graphics Inc., *Astrogator Central Bodies Gravity*, Systems Tool Kit (STK), Sep 2016.

[35] Shampine, Lawrence F. and Reichelt, Mark W., "The Matlab ODE Suite," *SIAM Journal on Scientific Computing*, Vol. 18, No. 1, 1997.

[36] Mathworks, *Mathematics: ode113*, The Mathworks Inc., Mar 2020. URL https://www.mathworks.com/help/matlab/ref/ode113.html, accessed: 1 May 2020.

[37] Bosanac, N., "Leveraging Natural Dynamical Structures to Explore Multi-Body Systems," Ph.D. thesis, Purdue University, Aug 2016. URL https://engineering.purdue.edu/people/kathleen.howell.1/Publications/Dissertations/2016_Bosanac.pdf, accessed: 1 May 2020.

[38] Schroeder, K., "Virginia Tech AOE 6984 Lecture: The Three-Body Problem," , Jan 2020.

[39] Markellos, V., "Asymmetric periodic orbits in three dimensions," *Monthly Notices of the Royal Astronomical Society*, Vol. 184, No. 2, 1978.

[40] Markellos, V., and Halioulias, A. A., "Numerical Determination of Asymmetric Periodic Solutions," *Astrophysics and Space Science*, Vol. 46, No. 1, 1977.

[41] Barrabés, E., and Mikkola, S., "Families of periodic horseshoe orbits in the restricted three-body problem," *Astronomy & Astrophysics*, Vol. 432, No. 3, 2005.

[42] Gordon, D. P., "Transfers to Earth-Moon L2 Halo Orbits Using Lunar Proximity and Invariant Manifolds," Master's thesis, Purdue University, August 2008. URL

https://engineering.purdue.edu/people/kathleen.howell.1/Publications/Masters/2008_Gordon.pdf, accessed: 8 Feb 2020.

[43] Wiggins, S., *Introduction to Applied Nonlinear Dynamics Systems and Chaos*, 2nd ed., Texts in Applied Mathematics, Springer, 2003.

[44] Ross, S., "Virginia Tech ESM 6314 Lecture: April 30, 2020," , Apr 2020.

[45] Haapala, A. F., "Trajectory Design in the Spatial Circular Restricted Three-Body Problem Exploiting Higher-Dimensional Poincaré Maps," Ph.D. thesis, Purdue University, Dec 2014. URL https://engineering.purdue.edu/people/kathleen.howell.1/Publications/Dissertations/2014_Haapala.pdf, accessed: 8 Feb 2020.

[46] Parker, J. S., and Anderson, R. L., *Low-Energy Lunar Trajectory Design*, Deep Space Communications and Navigation Series, NASA Jet Propulsion Laboratory, 2013.

[47] Krauskopf, B., Osinga, H. M., Doedel, E. J., Henderson, M. E., Guckenheimer, J., Vladimirsky, A., Dellnitz, M., and Junge, O., "A Survey of Methods for Computing (un)Stable Manifolds of Vector Fields," *International Journal of Bifurcation and Chaos*, Vol. 15, No. 3, 2005.

[48] Perko, L., *Differential Equations and Dynamical Systems*, 3rd ed., Texts in Applied Mathematics, Springer, 2006.

[49] Patterson, C. E., "Representations of Invariant Manifolds for Applications in System-to-System Transfer Design," Master's thesis, Purdue University, May 2005. URL https://engineering.purdue.edu/people/kathleen.howell.1/Publications/Masters/2005_Patterson.pdf, accessed: 8 Feb 2020.

[50] Bosanac, N., "Data-Mining Approach to Poincaré Maps in Multi-Body Trajectory Design," *Journal of Guidance, Control, and Dynamics*, Vol. 43, No. 6, 2020. URL https://arc.aiaa.org/doi/10.2514/1.G004857, accessed: 12 Feb 2020.

[51] Ross, S., "Virginia Tech ESM 6314 Lecture: March 26, 2020," , Mar 2020.

[52] Vaquero, T. M., "Poincaré Sections And Resonant Orbits In The Restricted Three-Body Problem," Master's thesis, Purdue University, May 2010. URL https://engineering.purdue.edu/people/kathleen.howell.1/Publications/Masters/2010_Vaquero.pdf, accessed: 1 May 2020.

[53] Leek, V., "An Optimal Control Toolbox for MATLAB Based on CasADi," Master's thesis, Linkoping University, Aug 2016. URL https://www.fs.isy.liu.se/Publications/MSc/16_EX_4986_VL.pdf, accessed: 8 Feb 2020.

[54] Conway, B. A., *Differential Equations and Dynamical Systems*, Cambridge University Press, 2010.

[55] Lawden, D. F., *Optimal Trajectories for Space Navigation*, Butterwroths Mathematical Texts, Butterworths, 1963.

[56] Pavlak, T. A., "Mission Design Applications In The Earth-Moon System Transfer Trajectories And Stationkeeping," Master's thesis, Purdue University, May 2010. URL https://engineering.purdue.edu/people/kathleen.howell.1/Publications/Masters/2010_Pavlak.pdf, accessed: 8 Feb 2020.